Multi-scale Computational Studies of Waterborne Coatings

by

Fang Yuan

A dissertation submitted in partial fulfillment
of the requirements for the degree of
Doctor of Philosophy
(Chemical Engineering)
in The University of Michigan
2015

Doctoral Committee:

Professor Ronald Larson, Chair
Professor John Kieffer
Assistant Professor Timothy Scott
Professor Robert Ziff

This dissertation is dedicated to my parents Yinglan Wang and Zhenghai Yuan in appreciation of their enduring support and encouragement.

ACKNOWLEDGEMENTS

Prof. Larson is the most important person for the completion of my desertion. I am greatly indebted to Prof. Larson for being such a inspiring and motivating motor. Ever since I joined his group in 2011, Prof. Larson never fails to surprise me with his depth and breadth of knowledge, every time I encounter an obstacle in my research, he always guides me through the darkness with some brilliant suggestions. His work ethics have greatly influenced me also, despite being a busy professor, he always returns my manuscript within a few days with thorough reviews. Besides being a great motor academically, he cares deeply about the students' personal well-beings. For a foreign student with no family ties in the States, holidays could be the most difficult days of the year. Prof. Larson always invites the students to celebrate Thanks-givings and some other holidays with his family, which fills my memories with great conversations and laughters.

I would like to sincerely thank Professor Robert Ziff, Professor John Kieffer, and Professor Timothy Scott for serving on my committee and for the numerous constructive suggestions I received from them throughout my PhD studies. I thank Prof. Kieffer for providing insightful suggestions and asking challenging questions during our regular monthly meetings with the DOW Chemical Company. I also thank Prof. Ziff for teaching me "Statistical and Irreversible Thermodynamics", his teaching sparked my interests in thermodynamics and laid a solid foundation for my research.

It is a great pleasure to acknowledge the funding source of my research, the Dow Chemical Company (DOW) and the people that I worked with for the past 3 years

from DOW, Dr. Valeriy Ginzburg, Dr. Antony Van Dyk, Dr. Susan Fitzwater, Dr. Alex Kalos and others. During our regular monthly meetings, they have provided a great number of suggestions and discussions which inspired the most important findings of my doctoral studies. I also thank them for inviting me to visit the Dow facilities in Midland, MI and Collegeville, PA, where I had the opportunities of sharing my work with people working in the chemical industry and gained first-hand experience of researches conducted by chemical companies.

I thank my parents for being so supportive of my pursuit of education. I thank them for having distilled the value of education and perseverance from the very early stage of my life. They have always encouraged me to follow my dream and achieve the highest goals of life. They made significant sacrifices in their personal lives so that I could receive the best education available in our city and nation. I hope that I will continue making them proud. I also thank my significant other Jason for always being there for me whenever I feel weak and for always encouraging me to achieve my goals.

I also acknowledge the help of my collaborators. I wish to thank Prof. Scott Milner and Prof. Kristen Fichthorn and Zifeng Li on our great experience of working on a project together. I would like to express my appreciation for all of our group members.

I also wish to thank the friends I made in the University of Michigan who have always been supportive of me and made my life in Ann Arbor enjoyable.

TABLE OF CONTENTS

LIST OF FIGURES

Figure

LIST OF TABLES

Table

ABSTRACT

Multi-scale Computational Studies of Waterborne Coatings

by

Fang Yuan

Chair: Ronald G. Larson

In this thesis, we apply multi-scale molecular dynamics (MD) simulations to enhance understanding of the molecular-level structure and interactions in waterborne coatings that is needed to go beyond the current trial-and-error methods of formulating them. We use atomistic simulations reveal the properties of the latex binder/water interface including the persistence of hydrogen bonds formation and interfacial water dynamics. We also develop a new method using a weighted histogram analysis method (WHAM) to calculate the free energy differences between of micelles of various sizes, and use this to determine the size distribution of the flower-like micelles formed by model hydrophobically modified ethoxylated urethane (HEUR) polymer rheology modifiers, containing an alkane hydrophobe at each end of the chain. We also use WHAM and first passage time analysis to determine the times required for hydrophobes to escape from micelles and from the latex surfaces. We find, for example, that these escape times from a latex surface are more than an order of magntidue larger than for the same hydrophobe from a micelle. This implies that a direct bridge of a latex particle to another latex particle via a HEUR molecule will persist longer than a bridge of a particle to a HEUR micelle, and that these direct particle-to-particle bridges likely

dominate the important rheological time sclaes of the latex suspension. These results help reveal the molecular structures of waterborne coatings that are responsible for the rheological properties of the coatings, such as their modulus, relaxation times, and shear thinning.

CHAPTER I

Introduction

1.1 Motivations

Waterborne coatings, often referred to as latex paints, have dominated the domestic and architectural market due to a series of regulations governing the emission of volatile organic compounds (VOCs). The market of waterborne coatings is foreseen to continue to grow at a healthy speed in the next decade. Despite the large market potentials of waterborne coatings, their formulas till this day are mostly trial-and-error based because of a lack of understanding of the structures of the multiple components and their interactions. The goal of this work is to achieve rapid multi-variant new product design and optimization by furthering the understanding of two-phase systems using multi-scale computational studies.

Paints are complex formulations of latex binders, pigments, dispersants, surfactants, rheology modifiers and other additives. The volume fraction of latex binders range from 5% to 35% in typical commercially available paint. The diameters of latex particles range from 100 nm to 300 nm, leading to a high interfacial area with water. Latex paint exhibits a desired viscosity profile over shear rates from $10^{-5}s^{-1}$ for settling to $> 10^{4}s^{-1}$ for paint applications[1]. Latex paints exhibit a shear-thinning behavior. To precisely control the viscosity over the large range of shear rate, rheology modifiers (RMs) such as hydrophobic ally modified eylene oxide urethane (HEUR)

are often added to the formulation[2].HEUR polymers consist of a poly(ethylene oxide) (PEO) backbone which are terminated by various hydrophobes[3]. The rheology of pure telechelic HEUR aqueous solutions is well understood. Above a threshold concentration, HEUR polymers aggregate to form flower-like micelles, in which each hydrophilic PEO groups form a "petal", the hydrophobic groups aggregate together to form the core[4]. At higher concentration the inter-aggregate spacing is reduced enough for the PEO chain to bridge two aggregates, forming a network of aggregates. At low shear rate, the aqueous solution of HEUR exhibits a Newtonian behavior followed by a shear-thickening regime, then a shear-regime at moderate and high shear rates, respectively[5].The shear thickening phenomenon was attributed to incomplete relaxation of a dissociating chain[6]. The shear thinning at even higher shear rates is often attributed to the pull-out of bridging chains from micelles.

Similarly to HEUR solutions, fully formulated paints undergoes structure changes in response to shear rate. For example, when an associative thickener is added to a latex suspension, the synergy between the particles and the thickener enhances the effect that each one has separately on viscosity [7]. A synergy between polymer and latex particle rheology is partially caused by the polymer adsorbing to the latex particle, thus incorporating it into the network, which increases the network bridging density and so its viscosity. However, the underlaying structure responsible for the rheology of fully formulated paints is less understood due to the complexity of the formulations.

The complex atomic-scale interactions between these components determine the macroscopic phase behavior, temperature sensitivity, and flow properties of the components, in ways that are not easily predicted using existing methods. However, increased computational speed, and the development of powerful multi-scale methods have now made it possible to bridge the gap between the atomic macroscopic scales.

Atomistic molecular dynamics simulations reveal structures and dynamics on a

molecular level and is widely used for tasks of exploring interactions between species in many applications[8]. However, the time and length scale accessible by atomistic simulations are greatly limited. By grouping multiple atoms into one "bead" and sacrificing degrees of freedom, coarse-grained simulations enable us to study systems that are larger in size and require a longer simulation time than what is accessible by atomistic simulations [9, 10, 11, 12].Recent progress in coarse-grained simulations including the parameterizations of a large number of coarse-grained beads have made it possible for us to study very complex realistic systems such as the waterborne coatings with great efficiency and accuracy[13, 14].

1.2 Methods

1.2.1 The CHARMM force field

MD is an algorithm for molecular simulations in which the particles are moved in discrete time steps in a continuum space. In this thesis, all atomistic simulations are conducted with the CHARMM force field unless otherwise noted.

1.2.1.1 Lennard-Jones potential

The Lennard-Jones potential is used to describe the non-boned interactions between particles.

$$V_{LJ}(r_{ij}) = 4\epsilon_{ij}\left(\left(\frac{\sigma_{ij}}{r_{ij}}\right)^{12} - \left(\frac{\sigma_{ij}}{r_{ij}}\right)^{6}\right) \tag{1.1}$$

in which i and j designates different atoms. LJ forces are only evaluated for atoms three or more bonds apart. The combination rules for these the LJ potentials are presented below for the equilibrium distance, σ and for the depth of the potential well, ϵ

$$\sigma_{ij} = \frac{1}{2}(\sigma_i + \sigma_j) \tag{1.2}$$

$$\epsilon_{ij} = \sqrt{\epsilon_i \epsilon_j} \tag{1.3}$$

1.2.1.2 Coulomb interactions

The Coulomb interaction between two charge particles is given by:

$$V_c(r_{ij}) = f\frac{q_i q_j}{\epsilon_r r_{ij}} \tag{1.4}$$

where f=138.935485, ϵ_r is the relative dielectric constant, in CHARMM force field, it is set to be 1.

The long-range Coulomb interactions are evaluated using Particle-mesh Ewald (PME). The potential at the grid points is calculated by inverse transformation, and by using the interpolation factors we get the forces on each atom.

1.2.1.3 Bonds

The bond stretching between two covalently bonded atom i and j is represented by a harmonic potential:

$$V_b(r_{ij}) = \frac{1}{2}k^b(r_{ij} - b_{ij})^2 \tag{1.5}$$

where b_{ij} is the equilibrium distance between atom i and j.

1.2.1.4 Angles

The Urey-Bradley bond-angle vibration between a triplet of atoms i-j-k is represented by a harmonic potential on the angle θ_{ijk} and a harmonic correction term on the distance between the atoms i and k. The Urey-Bradley potentials are used for CHARMM27 and CHARMM C35r force fields, and CGenFF force field used in this study does not contain the correction term on the distance between atom i and k.

$$Va(\theta) = \frac{1}{2}k_1(\theta - \theta^0)^2 + \frac{1}{2}k_2(r_{ik} - r_{ik}^0) \tag{1.6}$$

1.2.1.5 Proper dihedrals: periodic type

The proper dihedral angles of a sequence of atoms i, j, k and l are evaluated by equation

$$Vd(\phi) = k_\phi(1 + cos(n\phi - \phi_0)) \tag{1.7}$$

where ϕ is the angle between the ink and the jkl planes, with zero corresponding the *cis* configuration. This type of dihedral angle terms allows multiple potential functions to be applied automatically to a single dihedral angle.

1.2.1.6 Improper dihedrals: harmonic type

The improper dihedral angles are evaluated by

$$V_{id}(\xi) = \frac{1}{2}k_\xi(\xi - \xi_0)^2 \tag{1.8}$$

1.2.2 The MARTINI force fields

In the MARTINI force field, on average four heavy atoms are represented by a single coarse grain bead[9, 10, 15].

The non-bonded interactions are also evaluated by Equation 1.1 and Equation 1.4 where ϵ_r =15 for explicit screening, the Coulomb interactions are cut off at 1.2 nm. The bonded interactions are evaluated by Equation 1.5, and the angles are described using a weak harmonic potential of the cosine

$$V_a = \frac{1}{2}k^\theta \left(\cos(\theta) - \cos(\theta_0)\right)^2 \tag{1.9}$$

And the proper dihedrals are computed for the PEO groups using Equation 1.7.

1.2.3 The SDK force field

On average, the SDK force field mapped three heavy atoms to one coarse-grained bead. The LJ function is used for the non-bonded interactions[11, 12, 16].

$$V_{LJ}(r_{ij}) = B\epsilon_{ij}\left\{(\frac{\sigma_{ij}}{r_{ij}})^m - \frac{\sigma_{ij}}{r_{ij}})^n\right\} \tag{1.10}$$

For (m.n), two sets of values, (12,4) and (9,6) are selected. The choice depends on the type of interaction, with the non-bonded interactions involving "W" (water bead, each "W" bead represents three water molecules) are modeled with the LJ12-4 function, while all others employ the LJ9-6 functional form. The prefactor B is given by $\frac{3\sqrt{3}}{2}$ and 27/4 for LJ12-4 and LJ9-6, respectively. The long-range LJ force is truncated at 1.5 nm. The bonds are described by Equation 1.5, and the angle potentials are written as

$$V_a = k\left(\theta - \theta_0\right)^2 \tag{1.11}$$

The Coulomb interactions are evaluated by Equation 1.4, and the long-range Coulomb interactions are treated with PME.

1.3 Overview

In this work, we present the new models and tools we developed to study the waterborne coatings. In Chapter II we discuss the construction and the characterization of the atomistic model we build for the latex/water interface, as well as the interactions of this interface with surfactant and interfacial water molecules. In Chapter III, we develop a method of computing the first-passage time of hydrophobe escaping from micelles and from hydrophobic surfaces, we also compared the performance of two commonly used coarse-grained force fields with atomistic force fields. In Chapter IV, we apply multi-scale simulation techniques to study the properties of HEUR micelles.

Using coase-grained MARTINI force field, we develop a new method of computing the optimal HEUR flower-like micelle size through free energy calculations, and applying atomistic simulations, we characterize the molecular level interactions of HEUR molecules with water and surfactant molecules. Finally, in Chapter V, we conclude and present future avenues of research.

Bibliography

[1] A. K. Van Dyk, T. Chatterjee, V. V. Ginzburg, and A. I. Nakatani, "Shear-dependent interactions in hydrophobically modified ethylene oxide urethane (heur) based coatings: Mesoscale structure and viscosity," *Macromolecules*, vol. 48, no. 6, pp. 1866–1882, 2015.

[2] M. Huldén, "Hydrophobically modified urethane—ethoxylate (heur) associative thickeners 1. rheology of aqueous solutions and interactions with surfactants," *Colloids and Surfaces A: Physicochemical and Engineering Aspects*, vol. 82, no. 3, pp. 263–277, 1994.

[3] X.-X. Meng and W. B. Russel, "Structure and size of spherical micelles of telechelic polymers," *Macromolecules*, vol. 38, no. 2, pp. 593–600, 2005.

[4] M. A. Winnik and A. Yekta, "Associative polymers in aqueous solution," *Current opinion in colloid & interface science*, vol. 2, no. 4, pp. 424–436, 1997.

[5] T. Chatterjee, A. I. Nakatani, and A. K. Van Dyk, "Shear-dependent interactions in hydrophobically modified ethylene oxide urethane (heur) based rheology modifier–latex suspensions: Part 1. molecular microstructure," *Macromolecules*, vol. 47, no. 3, pp. 1155–1174, 2014.

[6] B. Van den Brule and P. Hoogerbrugge, "Brownian dynamics simulation of re-

versible polymeric networks," *Journal of non-newtonian fluid mechanics*, vol. 60, no. 2, pp. 303–334, 1995.

[7] T. Svanholm, F. Molenaar, and A. Toussaint, "Associative thickeners: their adsorption behaviour onto latexes and the rheology of their solutions," *Progress in organic coatings*, vol. 30, no. 3, pp. 159–165, 1997.

[8] D. Frenkel, "Understanding molecular simulation," 2002.

[9] S. J. Marrink, H. J. Risselada, S. Yefimov, D. P. Tieleman, and A. H. de Vries, "The martini force field: coarse grained model for biomolecular simulations," *J. Phys. Chem. B*, vol. 111, no. 27, pp. 7812–7824, 2007.

[10] L. Monticelli, S. K. Kandasamy, X. Periole, R. G. Larson, D. P. Tieleman, and S.-J. Marrink, "The martini coarse-grained force field: extension to proteins," *Journal of Chemical Theory and Computation*, vol. 4, no. 5, pp. 819–834, 2008.

[11] W. Shinoda, R. DeVane, and M. L. Klein, "Coarse-grained molecular modeling of non-ionic surfactant self-assembly," *Soft Matter*, vol. 4, no. 12, pp. 2454–2462, 2008.

[12] W. Shinoda, R. DeVane, and M. L. Klein, "Coarse-grained force field for ionic surfactants," *Soft Matter*, vol. 7, no. 13, pp. 6178–6186, 2011.

[13] H. Lee, A. H. de Vries, S.-J. Marrink, and R. W. Pastor, "A coarse-grained model for polyethylene oxide and polyethylene glycol: conformation and hydrodynamics," *The Journal of Physical Chemistry B*, vol. 113, no. 40, pp. 13186–13194, 2009.

[14] H. Lee and R. W. Pastor, "Coarse-grained model for pegylated lipids: Effect of pegylation on the size and shape of self-assembled structures," *The Journal of Physical Chemistry B*, vol. 115, no. 24, pp. 7830–7837, 2011.

[15] D. H. de Jong, G. Singh, W. D. Bennett, C. Arnarez, T. A. Wassenaar, L. V. Schafer, X. Periole, D. P. Tieleman, and S. J. Marrink, "Improved parameters for the martini coarse-grained protein force field," *Journal of Chemical Theory and Computation*, vol. 9, no. 1, pp. 687–697, 2012.

[16] X. He, W. Shinoda, R. DeVane, and M. L. Klein, "Exploring the utility of coarse-grained water models for computational studies of interfacial systems," *Mol. Phys.*, vol. 108, no. 15, pp. 2007–2020, 2010.

CHAPTER II

Molecular view of the latex/water interface in waterborne coatings

Some of the materials in this chapter are adapted with minor modifications from Ref [1].

2.1 Abstract

To obtain a molecular level view of the interface of a latex particle with water solvent, atomistic simulations using the CGenFF and OPLS (contributed by Zifeng Li *et al.*) were performed for a slab of methyl methacrylate (MMA)/n-butyl acrylate (BA) random copolymer in water. The carbonyl groups at the polymer/water interface were found to orient significantly towards the water phase. To evaluate the performance of CGenFF and OPLS, we calculated the structure factor for PMMA, which agrees with neutron scattering results. We also computed the temperature dependence of the surface tension of PBA/vacuum interface, which agree nicely with experimental results. The carbonyl groups of the latex surface were found to orient to form small angles with the the normal of the interface to form hydrogen bonds with water. The free energy change of transferring sodium dodecyl sulfate (SDS) molecule from the latex surface to the aqueous solution is found to be about 17 kT,

indicating a very strong bonding between SDS and latex surface, and the maximum surface coverage of SDS on latex polymer is found to be 1.87 $surf./nm^{-2}$.

2.2 Introduction

Since environmental regulations have required manufacturers to reduce volatile organic components (VOCs) in paint, waterborne latex paints have taken an increasing market share over traditional, organic-solvent-based paint [2]. Compared to solvent-based paints, current latex formulations have a longer shelf life, lower toxicity, lower flammability, and a decreased likelihood of reacting with the substrate. However, waterborne coatings have inferior leveling properties, toughness, resistance to dirt and fingerprints, and ability to withstand freeze-thaw cycles[3]. As a result, solvent-based paints are still primarily used in the industrial sector.

The stability of latex paint during storage is a result of a balance between interparticle van der Waals and electrostatic forces. Charged species near the particle surfaces, including negatively charged dissociated comonomers, surfactants and ions are crucial to achieving this balance.

The shear-thinning behavior of latex paint is essential for achieving the final appearance of the paint. During storage, a high viscosity is desired to prevent the separation of the paint, while during application, the paint must flow easily and form a smooth surface without dripping off the brush or running down a vertical surface. To achieve these properties, rheology modifiers such as telechelic hydrophobically modified ethylene oxide urethane (HEUR) polymer are widely used in the coating industry[4]. Telechelic HEUR polymers are nonionic, associative thickeners consisting of a hydrophilic poly(ethyl oxide)(PEO) backbone terminated with a hydrophobobe at each end[5]. Rheology modifiers form a network in the aqueous phase, but they can also bind to the surfaces of the latex particles, and thus influence interparticle forces and shelf life. In addition, surfactant competes for accessible surface

area with the rheology modifier, which may lead to complicated interactions between these additives.

Modern latex paints and coatings have remarkably complex formulations, which typically consist of polymer binders, surfactants, rheology-modifying polymers, and pigments. For such a complex system, it is the interfacial region between polymer binder particles (referred to as polymer or latex polymer below) and water that plays a key role in the stability and rheology of the paint. In this polymer/water interfacial region, the interactions between the surface and key solution species, such as surfactants, salts and rheology modifiers, affect the stability and rheology.

To analyze these interactions near the polymer/water interface, understanding the interfacial structure and properties as well as the interactions between the interface and the additives are essential. Here, we apply molecular dynamics (MD) simulations to the study of the surface of an acrylic latex particle, composed of methyl methacrylate (MMA)/n-butyl acrylate (BA) random copolymer. No simulation study of the interfacial structure of acrylic latex polymer in water has been reported heretofore. However, there are both experimental and simulation studies of the polymer/water interfacial structure for other polymers, including PMMA, which are particularly relevant to the work reported here. [6, 7, 8].

Recent studies of polymer/water interfacial structure have provided insight into the local restructuring of polymer in response to water. The density profile of the PMMA/water interface has been measured for supported films by specular neutron reflectivity[6] and obtained from MD simulations[7]. A PMMA film is thickened by water compared with the pristine film in air, indicating that water molecules penetrate into the polymer film. The orientation of PMMA groups at the polymer/water interface has been studied by sum frequency generation vibrational spectroscopy[8]. It was found that the carbonyl groups in the side chains orient towards the water phase to form hydrogen bonds with water. Lee *et al.* [7] observed in their atomistic

MD simulations that among all the polar atoms of PMMA, the carboxyl oxygens formed the greatest number of hydrogen bonds with water.

To gain a molecular level understanding of the surface properties of MMA/BA copolymer in water, an atomistic resolution model of the polymer/water interface was built using the CGennFF force force field[9]. These force field parameters were validated through the comparison of calculated static structure factors of bulk PMMA, PBA and the copolymer obtained from MD simulations and experimental neutron scattering results. Then the interfacial properties of latex copolymer with water were calculated for the copolymer/water interface and compared to existing experimental results. These results validate our simulation methods and force fields, and set the stage for studies of the interactions between the particle surface and surface charge groups, surfactants, counterions, rheology modifiers, and other components of latex paints.

Further, we characterize the interactions of the latex surface with a commonly used surfactant sodium dodecyl sulfate (SDS), and construct the adsorption isotherm of SDS onto latex/water interface using free energy profile obtained via umbrella samplings[10]. We also investigate the affect of SDS coverage on the behaviors of interfacial water molecules.

2.3 Methods

CHARMM General Force Field (CGenFF) [11] and CHARMM27 [12] parameters were applied to simulate the latex copolymer and SDS molecules respectively. CGenFF covers a wide range of organic molecules[11], and it is fully compatible with other versions of CHARMM, for example CHARMM27. CHARMM27 contains more accurate force field parameters for certain molecules than does CGenFF, while CGenFF covers more molecular structures than does CHARMM27, combining parameters from both CGenFF and CHARMM27 is a promising approach for planned

future simulations of complex waterborne coating materials, which contain sodium dodecyl sulfate, rheology modifiers made of polyethylene glycol and urea linkers, and other molecules. All the CGenFF parameters used in this study are listed in Appendix A

(a) MMA (b) BA

Figure 2.1: Structural units of MMA/BA copolymer.

To model commercial latex copolymers, we construct random atactic copolymer chains of MMA and BA monomers with a 1:1 molar ratio.

To simulate the bulk copolymer properties, we constructed 45 short chains of 20 monomers, which are roughly 50 times shorter than commercial MMA/BA copolymers. The choice of 20 monomers represents a compromise between computational cost and fidelity to the local structure of commercial polymers, which have a very low concentration of chain ends.

To mimic commercial latex chains, each chain in the simulation is constructed by randomly selecting the species and tacticity of each monomer. As a result, each chain is different, and can contain different numbers of MMA and BA monomers. To achieve a 1:1 overall molar ratio of MMA to BA, we randomly added MMA and BA monomers one at a time with equal probability. To control chain tacticity, we built mirror images of each monomer, for which the side groups pointed towards opposite directions. Each MMA or BA added had equal probability to be either the original monomer or its mirror image, resulting in atactic chains. Monomers in chain ends have similar structure to monomers in the middle, except for an extra hydrogen on the first or last backbone carbon atom. We also built PMMA and PBA homopolymers so that simulations of these could be compared to those for MMA/BA copolymers.

The homopolymers also consist of 45 atactic chains of 20 monomers with random tacticity, the same as for the MMA/BA copolymer.

To create a reasonable initial configuration, we built all-*trans* chains, rotated the chains to randomize their conformations, and subsequently packed them at a low density to avoid overlap. To build all-*trans* chains, we created each monomer with its first backbone carbon atom located at the origin. A translation vector between the first backbone carbon of adjacent monomers was computed. To polymerize a chain, we translated the N^{th} monomer by $(N-1)$ times this translation vector. In this way, an all-*trans* chain was obtained.

From the all-*trans* configurations, we prepared random walk conformations by rotating each dihedral to the *trans*, *gauche* +, or *gauche* - angles with equal probability. The oligomeric chains had no self-overlap after these rotations. Having constructed the individual chains, we translated them to fill a cubic simulation box at a sufficiently low density that chains did not overlap. The chains were packed with a minimum inter-chain distance of 7Å, which is twice the Lennard-Jones (LJ) diameter σ for an alkane carbon[13]. The resulting box size is 11nm on each side, with a corresponding low density.

To equilibrate the initial configuration, we performed an energy minimization, followed by a constant number, volume, and temperature (NVT) simulation with periodic boundary conditions. For energy minimization, the steepest descent and the l-BFGS (limited-memory Broyde-Fletcher-Goldfarb-Shannon) integrator[14] were utilized successively, with a force tolerance of 10 kJ/(mol $\cdot$ nm). The NVT simulation was run for 10 ns at high temperature (500K) to accelerate equilibration. The temperature was maintained by the velocity rescaling thermostat, [15] which is known to correctly render the canonical ensemble.

To reach the natural density of the bulk polymer, we used a constant number, pressure, and temperature (NPT) simulation with periodic boundary conditions to

further equilibrate the initial configurations. NPT simulations were conducted at 500K and 1 bar pressure for 30 ns. We used the Berendsen barostat [16] to reach the target pressure and then switched to the Parrinello-Rahman barostat [17] for further equilibration. We did not start with the Parrinello-Rahman barostat, since we found it either reaches the target pressure very slowly (with a large time constant), or can cause numerical instabilities (with a small time constant) if the pressure is far from equilibrium. After NPT equilibration, the cubic box dimensions of MMA/BA copolymer, PMMA, and PBA homopolymers were 5.38 nm, 4.89 nm, and 5.67 nm respectively.

All MD simulations used the leapfrog algorithm with a 2 fs time step. For efficiency, we enforced constant bond lengths with the LINCS bond constraint algorithm [18]. The cutoff radius of the non-bonded potentials was 10 Å . We updated the neighbor list every 10 time steps. The van der Waals potential was shifted, and smoothly switched to zero beginning at 10Å. The long-range electrostatic forces were computed using the particle-mesh Ewald [19] method. All simulations were performed using the GROMACS package[20]. Typically, our simulation contains about 13,000 polymer atoms and 8,400 water molecules. Our simulations run at a rate of about 10 ns/day using eight processors on a typical Linux cluster.

2.4 Results and discussion

2.4.1 Bulk properties

We used the static structure of polymers $S(q)$ to verify the OPLS (Optimized Potentials for Liquid Simulations) [13]and CGenFF force fields. The OPLS simulations were conducted under the same conditions by Lifeng Li from Pennsylvania State University.

2.4.1.1 Structure factor of polymers

Wide-angle neutron scattering (WANS) is commonly used to analyze the local structure of polymer melts. Here, we use the static structure factor S(q) obtained from WANS to validate our MD simulations by converting the radial distribution functions from MD to $S(q)$ via Fourier transform, which we then compare to the experimental $S(q)$.

The structure factor $S(q)$ is defined as

$$S(q) = \frac{1}{N} \sum_{j,k} b_j b_k \langle e^{iq|r_j - r_k|} \rangle \quad . \tag{2.1}$$

$S(q)$ can be related to the radial distribution function $g(r)$ using

$$S(q) = 1 + 4\pi\rho \int_0^\infty dr r^2 \frac{\sin qr}{qr} (g(r) - 1) \quad , \tag{2.2}$$

where $g(r)$ is defined using the partial radial distribution functions

$$g(r) = \frac{\sum_{\alpha,\beta} c_\alpha b_\alpha c_\beta b_\beta g_{\alpha\beta}(r)}{\langle b^2 \rangle} \quad , \tag{2.3}$$

with

$$\langle b^2 \rangle = \big(\sum_\alpha c_\alpha b_\alpha \big)^2 \quad . \tag{2.4}$$

Here $c_\alpha = N_\alpha / N$, where N is the total number of atoms, and b_α represents the neutron scattering length of species α. All samples are fully deuterated in all the analysis in the current work.

PMMA has been thoroughly investigated using WANS and MD simulations by Genix *et al.* [21], who break down the structure factor of PMMA into contributions from three molecular substructures: the main chain, the α -methyl group, and the

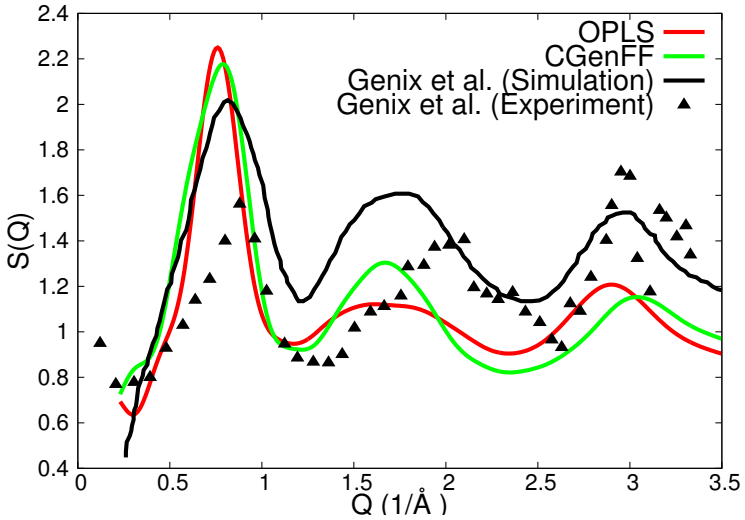

Figure 2.2: Structure factor of PMMA from simulation and experiment.

side group. In the current work, the OPLS and CGenFF force fields are validated by computing the static structure factor of PMMA and comparing the result with experimental WANS data and with the simulation results from Genix *et al.*[21] As can be seen in Fig. 2.2, results from both OPLS and CGenFF force fields show three peaks in the Q region from 0 to 3.5 Å^{-1} with positions in agreement with those by Genix and colleagues [21]. Genix *et al.* attributed the peak between 0.5 to 1Å^{-1} to inter-chain correlations, while the other two peaks result from complex interactions involving both the side groups and the main chain segments. The agreement in peak positions between our calculations and those of Genix *et al* indicate that the OPLS and CGenFF force fields capture the complex interactions between different groups of the PMMA molecules.

We also calculated the structure factor of PBA using the CGenFF and OPLS force fields. As shown in Fig. 2.3, the two force fields agree reasonably well in the positions of the three peaks located approximately at 0.33Å^{-1} (I), 1.2Å^{-1} (II), and 3.1Å^{-1} (III). The peak at Q =0.33Å^{-1} can be assigned to the average inter-molecular interactions, *i.e.*, the distance between chains. This peak is at a smaller Q than the lowest-Q, peak of the PMMA structure factor in Fig. 2.2, indicating a larger

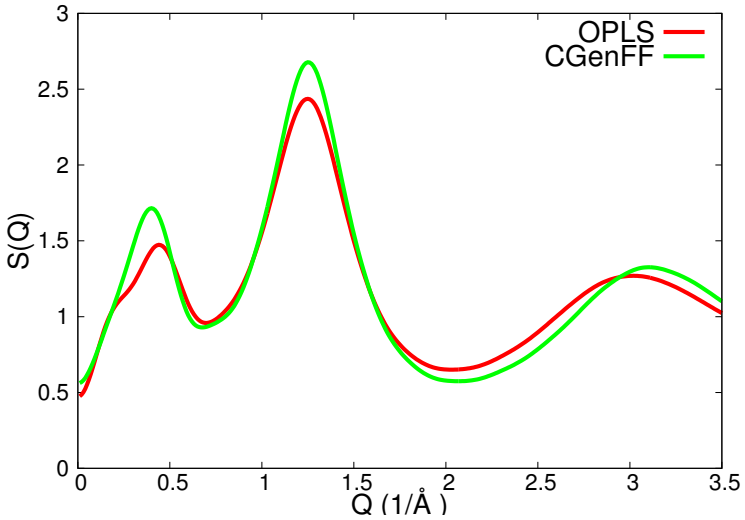

Figure 2.3: Structure factor of PBA.

separation between chains in PBA. This could be due to the bulkier side group in PBA ($COOCH_2CH_2CH_2CH_3$) compared to that in PMMA ($COOCH_3$).

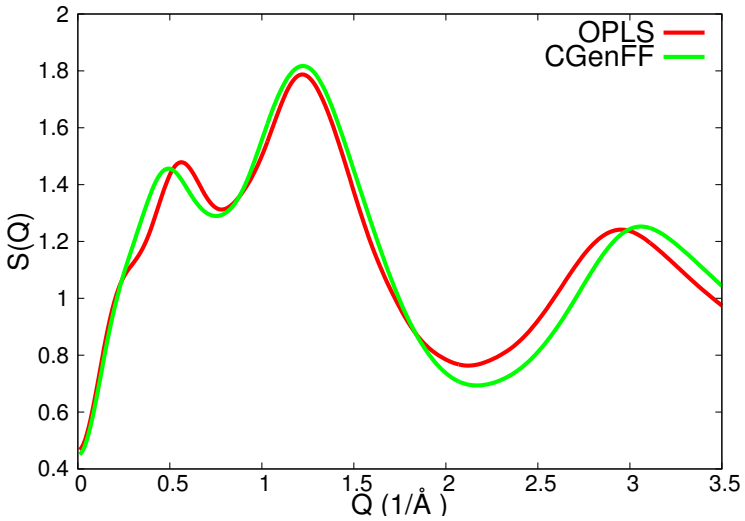

Figure 2.4: Structure factor of MMA/BA copolymer.

Finally, the structure factors of the 50/50 (by mole) copolymer of PMMA and PBA for CGenFF and OPLS force fields, shown in Fig. 2.4, are very similar, indicating that the force fields predict similar local ordering of the polymers.

As summarized in Fig. 2.5, CGenFF and OPLS force fields demonstrate similar structure factors for PMMA, PBA and the copolymer. The first distinct peak at

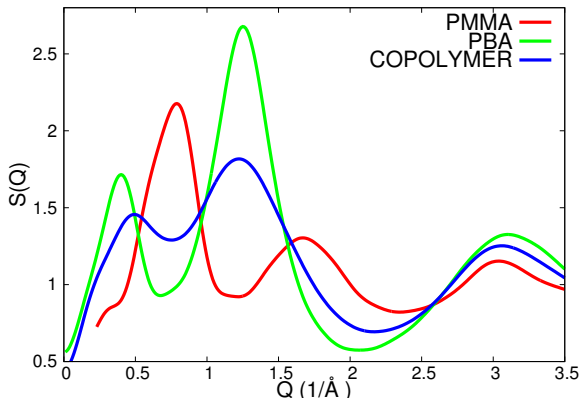

(a) CGenFF

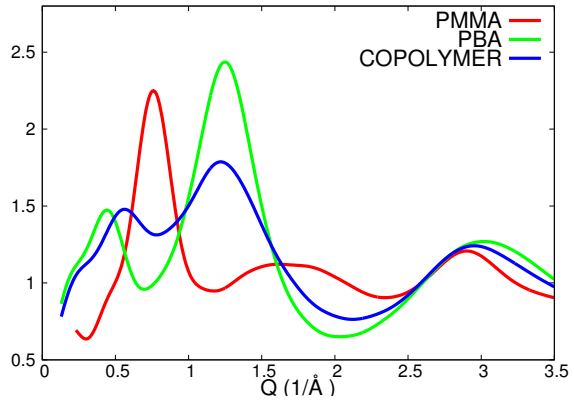

(b) OPLS

Figure 2.5: Structure factor $S(Q)$ of PMMA, PBA, and copolymer calculated using the CGenFF (a) and the OPLS (b) force fields.

low Q, which results from inter-molecular interactions, occurs at the lowest Q value for PBA, followed by the copolymer and then PMMA, indicating that PBA has the largest main chain average separation distance, while PMMA has the smallest.

2.4.1.2 Surface Tension of PBA

To further validate the CGenFF in producing the properties of the polymers, we computed the surface energy of the PBA/vacuum system at different temperatures. To simulate the PBA/Vacuum interface, we extend the simulation box of the bulk PBA system described earlier to 20 nm on the z direction. Our calculation of the surface tension of the PBA/vacuum interfaces began at 580K and progressed downward in temperature to 360K in steps of 40K. For each temperature, a NVT simulation of 100 ns was performed.

We applied the mechanical approach[22], where the surface tension is calculated from the pressure anisotropy:

$$\gamma = \frac{L_z}{2} \left\langle P_z - \frac{P_x + P_y}{2} \right\rangle \quad , \tag{2.5}$$

where L_z is the simulation box length in the z direction (normal to the interface), and the prefactor of 1/2 accounts for the presence of two interfaces in the system. Here P_z and $(P_x + P_y)/2$ are the normal and lateral components of the pressure tensor. This method enables us to calculate the interfacial tension from an NVT simulation.

The surface tension calculated using Eq. 2.5 does not take into account the contribution of long-range LJ interactions beyond the simulation cutoff radius. To restore the contribution of long range LJ interactions, we perform a "tail correction" [23]. Each atom with different LJ parameters is considered as a different LJ atom type.

The tail correction to the interfacial tension is then calculated as:

$$\gamma_{tail} = 12\pi(\rho_A - \rho_B)^2 \int_{r_c}^{\infty} dr \int_0^1 ds \frac{3s^3 - s}{r^3} \coth(\frac{rs}{d}) \quad , \tag{2.6}$$

in which the coefficients ρ_A and ρ_B are defined by

$$\begin{aligned} \rho_A &= \sum_u \epsilon_i^{\frac{1}{2}} \sigma_i^3 \rho_{i,A} \\ \rho_B &= \sum_i \epsilon_i^{\frac{1}{2}} \sigma_i^3 \rho_{i,B} \quad . \end{aligned} \tag{2.7}$$

The quantities ρ_A and ρ_B have dimensions of (energy)$^{1/2}$ (see below).

The sums in Eq. 2.7 run over each LJ atom type i; $\rho_{i,A}$ and $\rho_{i,B}$ are the number densities of atom type i in the bulk of phase A (the middle of the polymer slab) or phase B (the vacuum), respectively. The LJ energy and distance parameters for atom type i are denoted ϵ_i and σ_i respectively. The LJ cutoff radius is denoted as r_c (1 nm in this study), and d is the interfacial thickness.

The $\rho_{i,A}$, $\rho_{i,B}$ and d are obtained by fitting the number density profiles to the hyperbolic function tangent function:

$$\rho(z) = \frac{1}{2}(\rho_A + \rho_B) + \frac{1}{2}(\rho_A - \rho_B) \tanh\left(\frac{z - z_0}{d}\right) \quad , \tag{2.8}$$

where ρ_A and ρ_A are the bulk densities on either side of the planar interface, centered at z_0 with a normal thickness d.

The tail correction term achieves an upper bound of

$$\gamma_{tail,max} = 3\pi r_c^{-2}(\rho_A - \rho_B)^2 \quad , \tag{2.9}$$

in the limit of a sharp interface. From this limit, we see clearly that the tail correction decreases with increasing cutoff radius as r_c^{-2}.

We computed the interfacial energy as a function of temperature to extrapolate the value down to the room temperature, where the simulation is remarkably slow.

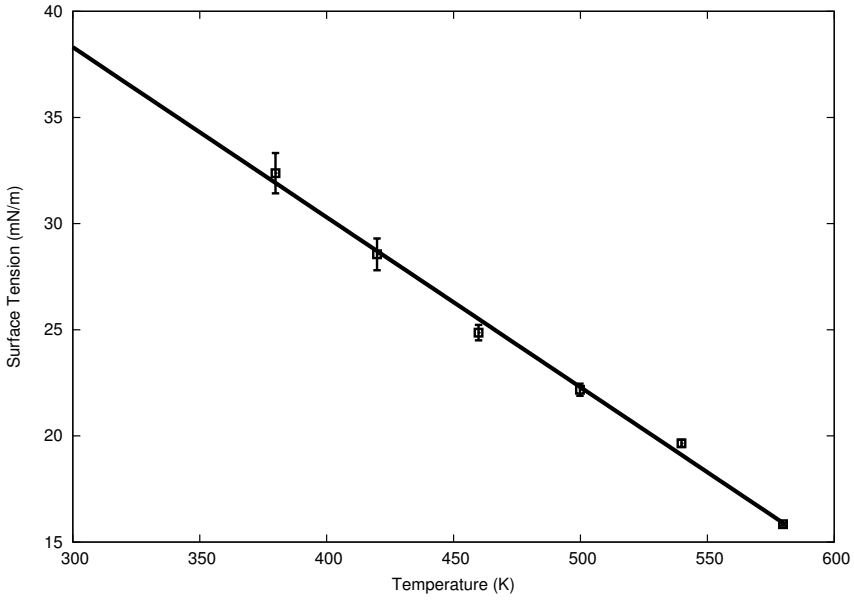

Figure 2.6: Surface tension of PBA at different temperatures with tail corrections, error bars represent standard deviations. The linear fitting function is -0.080x+62.3282

The surface tensions with tail corrections decrease linearly with increasing temperature, as shown in Fig. 2.6. The surface entropy $-\partial\gamma/\partial T$, given by the slope of the data, is 0.080 mN/(m· K), and it has been reported as 0.070 mN/(m· K) experimentally [24]. Ref. [24] reported the surface tension to be 33.7 mN/m at 20°C, very similar to our result from the fitting curve (38.9 mN/m).

The CGenFF force field successfully reproduced the static structure factors of PMMA, PBA and their copolymer, as well as the surface tension of PBA/vacuum system, and therefore is applied in the current study to simulate the copolymer/water interface.

2.4.2 Interfacial properties

2.4.2.1 Density profile

To probe latex/water interfaces, we created copolymer/water interfaces by creating polymer surface slabs and introducing water molecules. We examine density profiles of polymer and water, the re-structuring of the polymer surface when polymer forms hydrogen bonds with water. In these simulations, we model our polymer surface as a slab, since at the length scale of our simulation (a few nanometers), the curvature of the polymer surface could be ignored.

The initial configuration was obtained from an equilibrated bulk NPT simulation of 45 random 20-mers using periodic boundary conditions, resulting in a cubic box of about 5 nm on a side. Then the cubic box was repeated on the x and y direction to form a slab of 10 nm $\times$ 10 nm $\times$ 5 nm with the shorter dimension on the z direction.

This configuration was then placed in the center of a rectangular box, with dimensions 10 nm (x) by 10 nm (y) by 16 nm (z). This results in a 5.5 nm vacuum layer in the z direction on either side of the polymer slab. Then an annealing simulation from 500K to 298K with NVT ensemble was conducted to allow the resulting rough surface to relax.

The final polymer slab is 5 nm thick (in the z direction), with a square cross section of 10 by 10 nm. Recall that the system has periodic boundary conditions, so that the slab is in fact periodically continued in the x and y directions, with chains able to cross these periodic boundaries while remaining in the slab of melt. Our choice of a slab dimensions represents a compromise that results in a reasonably high surface area, while maintaining a slab thickness large enough that the density and local structure of the polymer in the interior of slab is representative of bulk material.

The polymer/water interfaces were then created by introducing water molecules above and below the polymer slab. We first inserted water molecules to fill the

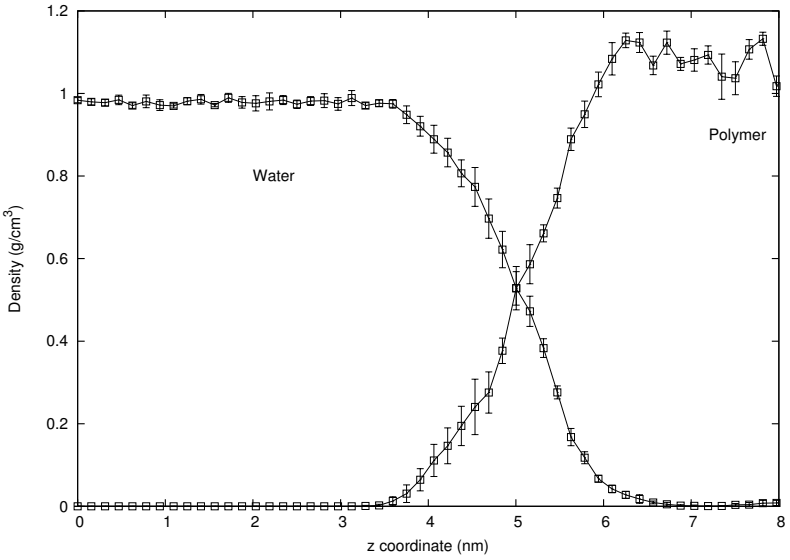

Figure 2.7: Density profiles for the MMA/BA copolymer and water.

portion of the simulation box not occupied by polymer. To avoid atom overlap, water molecules were then removed from the box where the distance between any atom of water and any atom of the polymer was less than the sum of the Van der Waals radii of both atoms. We used the extended simple point charge (TIP3P) water model [25]. Water molecules were constrained using the SETTLE algorithm[26].

After adding the water, we first performed an energy minimization simulation, then a 20 ns NPT simulation was performed before a production 20 ns NPT simulation at the same temperature.

A sharp interface forms between the immiscible copolymer slab and the adjacent water region. The simplest characterization of this interface is its density profile. To obtain the density profiles, we divided the simulation box into 100 bins along the z direction, normal to the interfaces, and calculated the mass density of polymer or water within each bin. The last 5 ns of data in the NPT simulation, was used to obtain the time-averaged density. The simulated bulk density of polymer fluctuates around 1.09 g/cm^3. The simulated bulk density of water is 0.981 g/cm^3, slightly smaller than the experimental value of 0.997 g/cm^3. The density profiles of polymer and water

overlap at the interface, indicating that water molecules penetrate into the polymer surface. To measure the interfacial widths, the polymer density profiles in water and vacuum were fitted by the hyperbolic tangent function Equation 2.8 mentioned above. Typically, the interfacial width t is reported as $t = 2.1972d$, *i.e.*, the width between 10 and 90 % of the density increase, which is the "10-90 thickness"[27] .Since the density profiles include two interfaces we merged the data of two interfaces by reflecting the right-hand density profile to coincide with the left-hand profile before fitting (see Fig. 2.7). The fitted copolymer/water interfacial width ($t = 1.58 \pm 0.22$) nm.

The measured interfacial width could be affected by surface roughness or capillary waves. We devided the simulation box into four equal quadrants in the $x - y$ plane. The density profiles in each quadrant were fitted using Eq. 2.8 to obtain the center of the interface and the interfacial widths and their average density at each z position and the standard deviations are plotted in Fig. 2.7. The standard deviations are not significant, and we consider the surface roughness not large enough to significantly affect the measured interfacial width.

2.4.2.2 Hydrogen Bonding and Surface Structure.

Hydrogen bonds form between polymer oxygens and water hydrogens at the polymer/water interface, which affects the structure of the polymer surface. In this section, we examine the fraction of polymer groups forming hydrogen bonds at the interface, and the orientation of polymer surface groups. Hydrogen bonds are identified in the simulation by a geometrical criterion: (1) the distance between water oxygen and polymer oxygen must be less than 3.5Å, and (2) the hydrogen bond angle (formed by the water oxygen, water hydrogen, and polymer oxygen) should be greater than 150°. About 20 % of the carbonyl oxygens at the interface form hydrogen bonds. The fraction of carbonyl oxygens forming hydrogen bonds is simply the ratio of the total

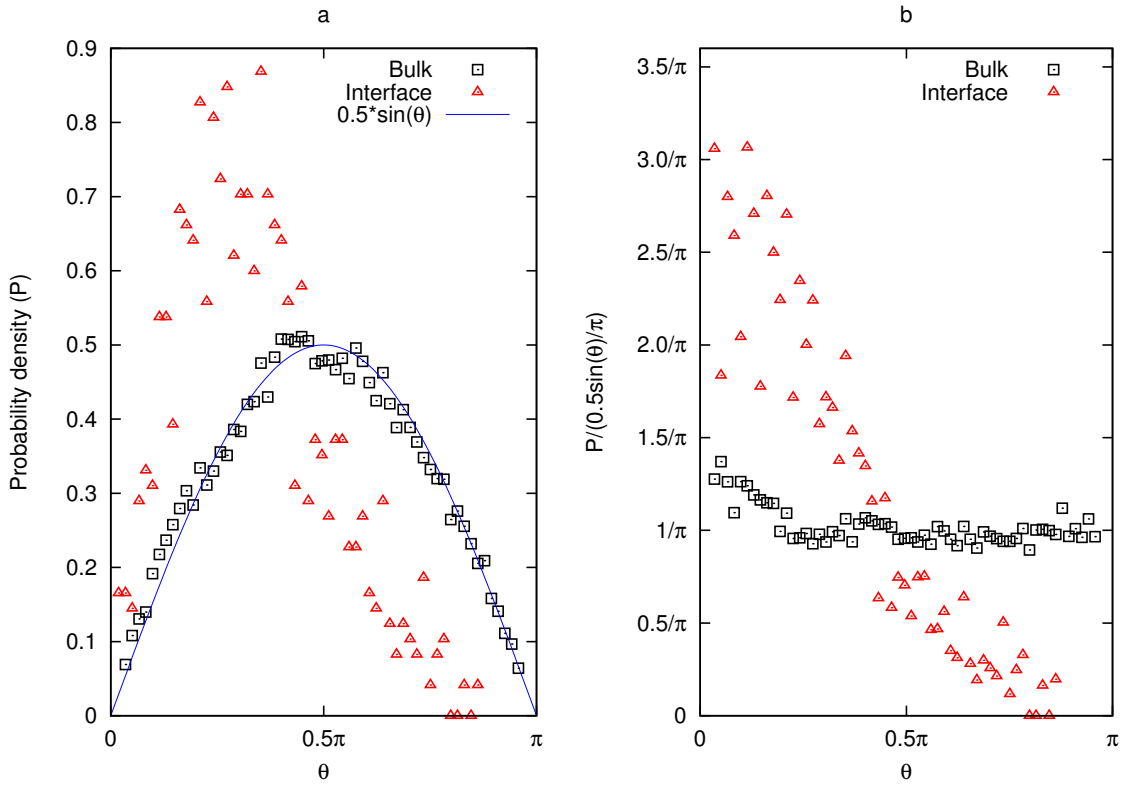

Figure 2.8: (a) Orientation distribution P(θ) of carbonyls on copolymers at the latex/water interface, and in the bulk of the slab, the line is the fitted sine function. (b) The normalized orientation distribution divided by the fitted sine function, an isotropic distribution corresponds to a constant value of $\frac{1}{\pi}$.

number of hydrogen-bonding carbonyls to the total carbonyls in the interfacial region. Nearly all the interfacial hydrogen bonds with the polymer were formed by carbonyl oxygens, with only 2 % formed by ester oxygens from MMA or BA monomers.

Since polymer surface groups reorganize to form hydrogen bonds, we may expect these surface groups to alter their orientation with respect to the same groups in the bulk. To quantify the orientation of carbonyl groups after equilibration, we calculated the angles between carbonyl dipole (from carbon to oxygen) and the interface normal (towards water/vacuum). The analysis was based on 100 frames spanning 10 ns.

The carbonyl groups at the water interface orient towards the interface signifi-

cantly compared with the carbonyls in the bulk, as shown in Fig. 2.8. The angles for interfacial carbonyls were all skewed towards small values, indicating orientation normal to the interface. By contrast, the carbonyls in the bulk are distributed isotropically, as indicated by their coincidence with a sinusoidal distribution (fitting line in Fig. 2.8). Preferential orientation of interfacial carbonyls has been observed qualitatively for PMMA/water interfaces using sum frequency generation vibrational spectroscopy[8]. The angles at the interface were found to be skewed toward small values, with an average of 49° (The average angle is evaluated by $\theta_{avg} = \int_0^\pi d\theta P'(\theta)\theta$, where $P'(\theta)$ is $P(\theta)$ normalized by $\frac{sin(\theta)}{2\pi}$), compared to the average value for the bulk region is found to be 88°, which is very close its theoretical value of 90° (random distribution). This deviation is due to noise caused by insufficient sampling.

2.4.2.3 Adsorption isotherm of SDS on the copolymer surface in water

We adopted the method discussed in Ref. [28] to obtain the adsorption isotherm of SDS adsorbing onto the copolymer/water interface.

Assuming that the surfactant adsorbed on the surface are in equilibrium with surfactant in bulk solution, and the bulk solution can be considered ideal. The chemical potential of the surfactant in bulk solutions could be written as

$$\mu_0 = \mu^\Theta + k_B T ln\big(\frac{c_0}{c^\Theta}\big) \tag{2.10}$$

where μ^Θ is the standard chemical potential at standard concentration c^Θ. The chemical potential of a surfactant molecule adsorbed at a height z which is the perpendicular distance between the surface and the center of mass (COM) of the surfactant

$$\mu(z) = \mu^\Theta + k_B T ln\big[\frac{c(z)}{c^\Theta}\big] + w(z) \tag{2.11}$$

where c(z) is the local concentration of surfactant, and w(z) is the free energy change

of of transferring a surfactant from an ideal bulk solution sufficiently remote from the surface to the position z from the surface with coverage Γ. At equilibrium, $\mu(z) = \mu_0$ and so

$$c(z) = c_0 exp\big[-\frac{w(z)}{k_B T}\big] \tag{2.12}$$

The goal adsorbed number of molecules per unit area of surface is given by

$$\Gamma = \frac{1}{A} \times \int_0^{z^*} Ac(z)dz \tag{2.13}$$

where z^* is a dividing height between adsorbed and desorbed states and A is the surface area (z^* is chosen to be 2.5 nm in this thesis), thus

$$\Gamma = c_0 \int_0^{z^*} exp\big[-\frac{w(z)}{k_B T}\big]dz = c_0 K(\Gamma) \tag{2.14}$$

The adsorption isotherm is defined by

$$c_0 = \frac{\Gamma}{K(\Gamma)} \tag{2.15}$$

We applied umbrella sampling and the weighted histogram analysis method (WHAM) to compute W(z) which is also referred to as the potential of mean force (PMF). To compute the PMF, we simulated 49 umbrella sampling windows with the window spacing of 0.6 Å(the COM of SDS is transferred from 1.84 nm away from the COM of copolymer slab to 4.78 nm away). At each simulation window, the COM distance of SDS and copolymer slab is constrained with a harmonic potential of 1200 $kJ/(mol \cdot nm^2)$ at each window.

By checking the histograms of each simulation window, we ascertained that a sufficient overlap between adjacent windows was achieved for the umbrella sampling simulations (see Fig. 2.9).

The weighted histogram analysis method (WHAM) was used for postsimulation

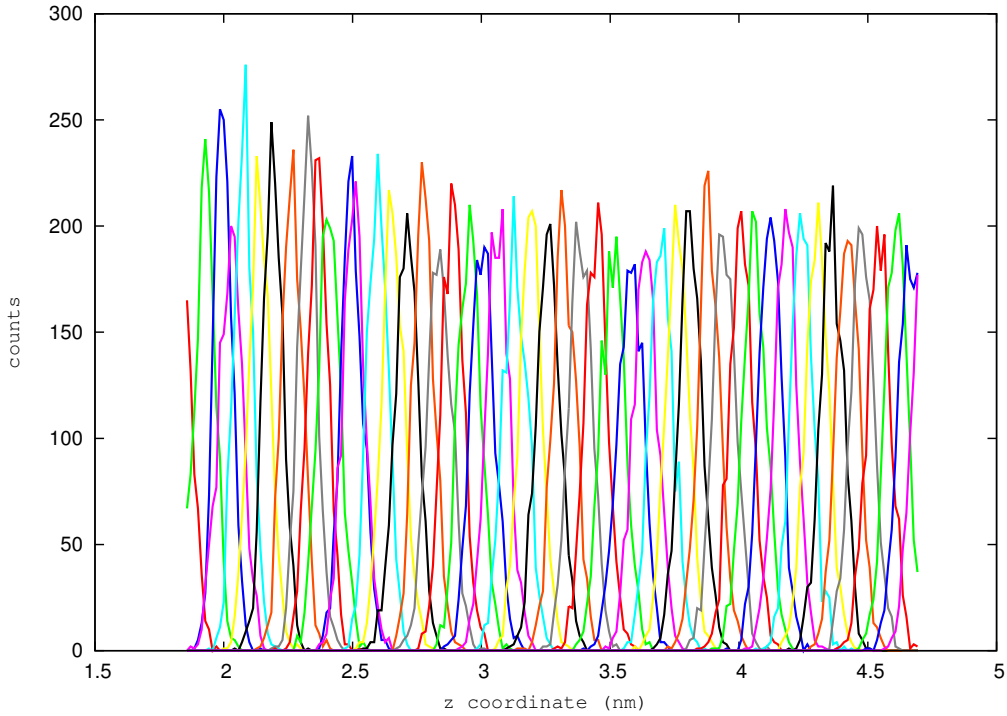

Figure 2.9: Number of counts for the umbrella sampling histogram of transferring a SDS molecule into the bulk solution along the z distance between the copolymer slab and the SDS molecule. The neighboring histograms are sufficiently overlapped.

unbiasing of umbrella sampling data in this work. The resulting PMF constructed from the umbrella sampling simulations is shown in Fig. 2.10. The free energy barrier for transferring a SDS molecule from its equilibrium position on the latex surface to water is about 17kT. Applying Equation 2.14, we obtain $K(\Gamma) = 3.34 \times 10^6\ nm$ ($2.01 \times 10^6\ surf./nm^{-2}(mol/L)^{-1}$).

To obtain the maximum coverage of SDS on the copolymer surface in water, we simulated copolymer/water slab systems with three different surfactants coverages. We placed 25 SDS surfactant molecules on each side of the copolymer/water interfaces to simulate a copolymer surface with an SDS coverage of 0.23 nm^{-2}, similarly, SDS coverage of 0.94 nm^{-2} and 1.89 nm^{-2} were simulated by placing 100 and 196 SDS molecules on each side of the copolymer/water interface respectively. In the course of 20 ns of NPT simulations at 1 bar, 298 K, no SDS were observed to escape from the system of 0.23 nm^{-2} SDS coverage and 0.94 nm^{-2} coverage, and average, 2 SDS molecules escaped from the copolymer surface with initial SDS coverage of 1.89 nm^{-2}, resulting a final SDS coverage of 1.87 nm^{-2}.

Assuming that the isotherm takes the form of a Langmuir isotherm, which has a low concentration region where the coverage increases linearly with the bulk concentration and a high concentration region where the coverage reaches its maximum and does not change with increasing bulk concentration, we obtained the adsorption isotherm of SDS on the latex surface, shown in Fig. 2.11.

2.4.2.4 SDS monolayers adsorbed on the latex surface and their effect on local water ordering and dynamics

To characterize the SDS monolayer adsorbed on the latex surface, trajectories of the NPT simulations of latex surface covered with different surface densities (0,23, 0.94 and 1.87 $surf./nm^{-2}$) of SDS molecules mentioned above were analyzed. The local arrangement of the SDS molecules could be characterized by the tilt angle (θ)

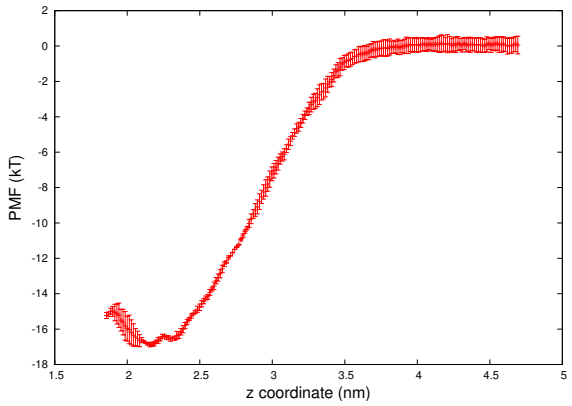

Figure 2.10: Potential of mean force of extracting an SDS molecule from the copolymer surface into the bulk solution. Error bars represent standard deviations

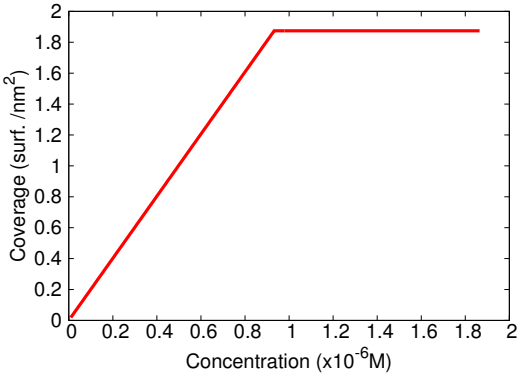

Figure 2.11: Adsorption isotherm of SDS on the latex surface in water.

(θ is defined as angle between the fist principal axis of an SDS molecule with the vector perpendicular to the latex surface) distributions. We plotted the distribution (P) of the tilt angle in Fig. 2.12 (a). The average tilt angle defined as $\theta_{avg} = \int_0^{\frac{\pi}{2}} \theta P(\theta) d\theta$ as a function of the surface coverage of SDS is plotted in Fig. 2.12 (b). Numerous previous studies suggested that the tilt angle of self-assembled monolayers (SAM) is directly related to coverage[29, 30], Castillo *et al.* reported a quadratic dependance of the tilt angle and on coverage for SAM of dedecyltrichlorosilane (DTS) and octavecyltrichlorosilane (OTS) on silica using MD simulations, our results show a similar trend.

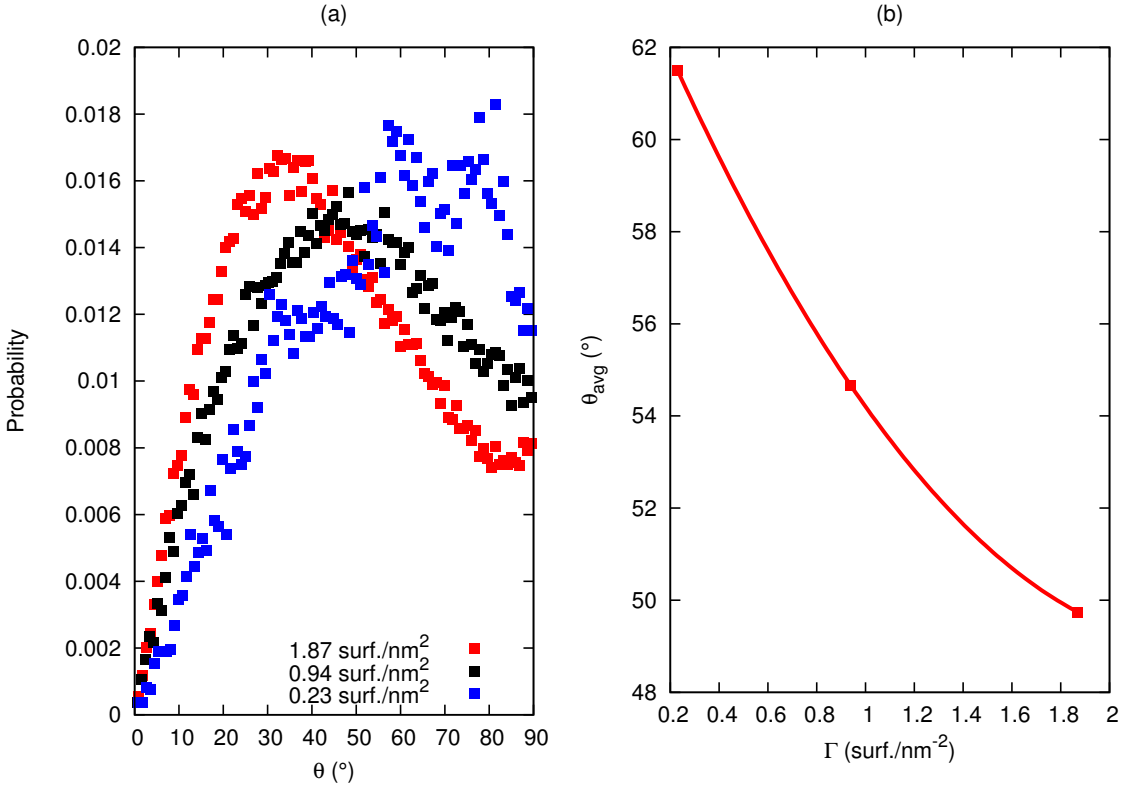

Figure 2.12: (a) Probability distribution of tilt angle of SDS molecules at different SDS surface densities. (b) The average tilt angle of SDS as a function of surface density (Γ), the dots are calculated from simulations, and the line is the fitted quadratic function (y=2.64865x^2-12.7295x+64.2832).

The effects of different SAM [31, 32] and adsorbed surfactants [33] on interfa-

cial water packing, ordering and dynamics have been documented in recent years. Tummala *et al.* [33] demonstrated that the properties of interfacial water near surfactants adsorbed to different substrates depend both on the surfactant coverage and the substrate properties. Since the the dynamics of interfacial water determine various processes including the diffusion of solutes near interfaces and therefore affect the performance of coatings[33], we here study the effect of coverage of SDS on interfacial water dynamics.

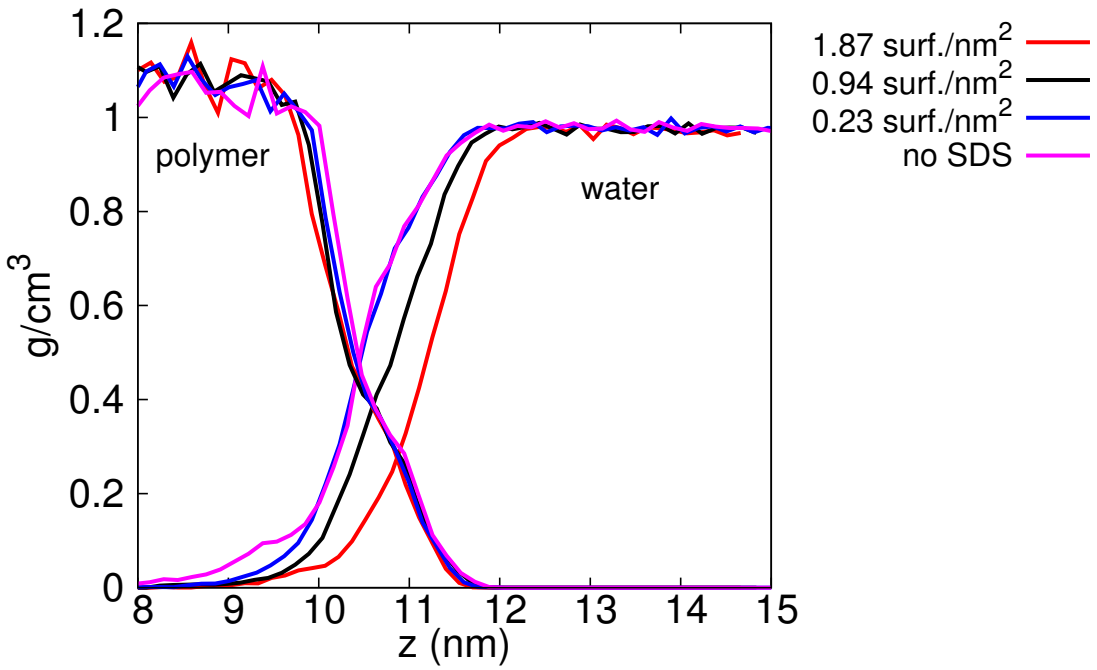

Figure 2.13: Density profiles of MMA/BA copolymer and water with different SDS surfactant coverages.

Fig. 2.13 shows the density profiles of latex/water interfaces with various SDS surfactant coverages. As the surfactant surface density increases, the water molecules are moved further away from the surface. The half-density plane of water [31] moves 0.74 nm away from the latex surface as the surface density of SDS increases from 0

to 1.87 nm^{-2}.

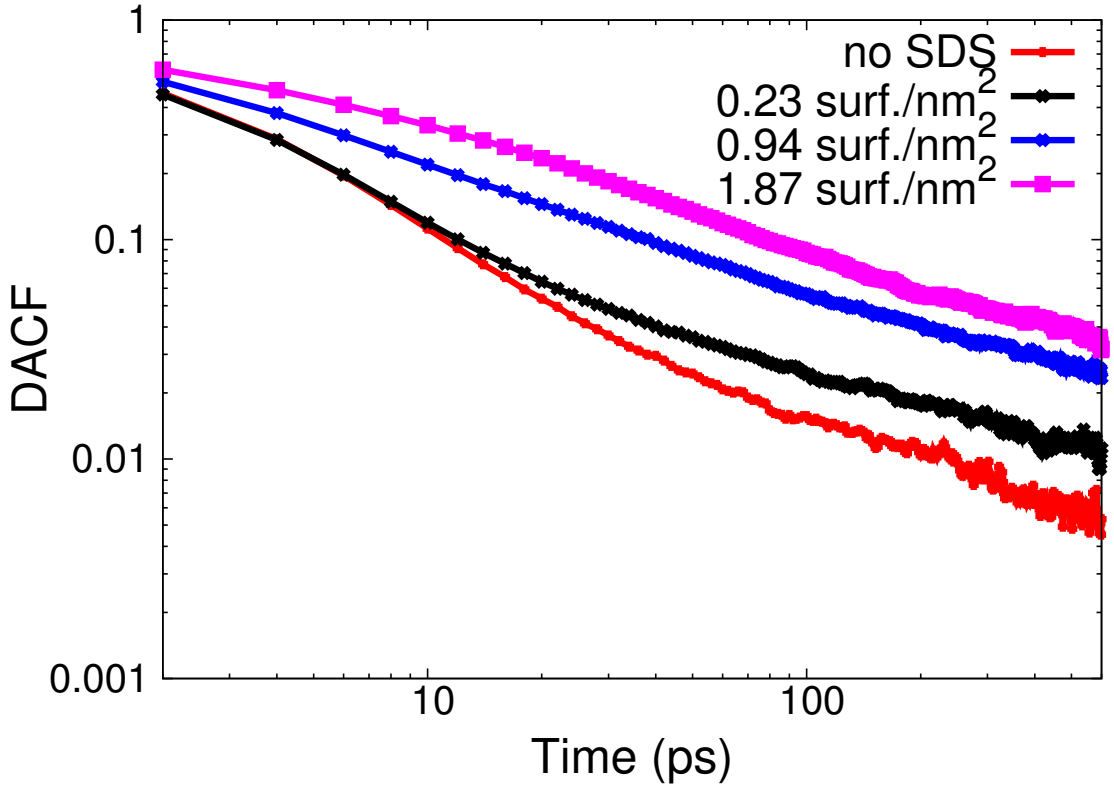

Figure 2.14: Dipole-dipole autocorrelation function (DACF) for interfacial water molecules.

We define the interfacial region as a slab of thickness of 2 nm centered at the half-density plane of water, and study the dipole-dipole autocorrelation function (DACF). The dipole moment vector a water molecule points from the midpoint between the hydrogen atoms toward the oxygen. DACF is defined as

$$\text{DACF} = \left\langle \frac{\mu_w(t) \cdot \mu_w(0)}{\mu_w(0) \cdot \mu_w(0)} \right\rangle \tag{2.16}$$

The orientational relaxation time τ_r is calculated by numerical integration from zero to 1 ns to avoid difficulties fitting the fast librational oscillation and decay, followed by analytical integration of the best fit exponential tail. The relaxation time

τ_r is therefore defined as [34]

$$\tau_r = \int_0^\infty \left\langle \frac{\mu_w(t) \cdot \mu_w(0)}{\mu_w(0) \cdot \mu_w(0)} \right\rangle dt \tag{2.17}$$

DACF is 1.0 at time zero and decays gradually as the water molecules rotate. Previous studies demonstrated that the rotational dynamics of water molecules in the hydration shell of charged groups are slower than those in the bulk[34], the decay time depends on both on the size and the charge of the hydrated groups[35] and also the hydrophobicity of the surface[36].

We show DACF for interfacial water molecules in Fig. 2.14. We observe the fasted decay for DACF in the absence of SDS, and DACF curves decay at similar rates for the first 10.0 ps for the system with no SDS and low coverage (0.23 nm^{-2}), suggesting that the water molecules on low coverage of SDS are in close proximity to the hydrophobic moieties, which is consistent with Fig. 2.13.

Table 2.1: Coverage dependence of rotational relaxation times

Γ ($surf./nm^2$)	0	0.23	0.94	1.87
τ_r (ps)	10.9	17.1	36.6	52.3

As the coverage of SDS increases from 0 $surf./nm^2$ to 1.87 $surf./nm^2$, the rotational relaxation time increases about 5 fold, indicating that the increased charge caused by the adsorbed SDS significantly slows down the rotational dynamics of water.

2.5 Conclusions

In this chapter, we studied the interfacial structure and associated energies of a 50/50 mole ratio MMA/BA latex copolymer in water using chemically detailed MD simulations. We first calculated bulk properties to test the validity of the

force field parameters, including structure factor of MMA/BA copolymer, as well as PMMA and PBA homopolymers and the temperature dependence of surface tension of PBA/vacuum interface.

The structure factor of PMMA is in reasonable agreement with literature data, and the structure factor of all three polymers calculated using two different force fields are reasonably consistent with each other.

We examined the structure of the copolymer/water interface. We found that water molecules penetrate into the polymer slab at the interface, and form hydrogen bonds with polymer carbonyl groups. About 20 % of polymer carbonyls at the interface form hydrogen bonds with water. Carbonyl groups at the polymer/water interface orient more towards the water phase, resulting in an average angle of about 49° with the interface normal, while carbonyls in the center of the polymer slab are isotropically oriented.

Having established this interfacial model, we characterized the interactions of the latex surface with SDS surfactant molecules. The adsorption isotherm of SDS on the latex surface was calculated. We discovered that the surface density of SDS adsorbed on the latex surface affect the tilt angles of the SDS molecules and the interfacial water properties, both are consistent with previous studies.

Bibliography

[1] Z. Li, F. Yuan, K. A. Fichthorn, S. T. Milner, and R. G. Larson, "Molecular view of polymer/water interfaces in latex paint," *Macromolecules*, vol. 47, no. 18, pp. 6441–6452, 2014.

[2] J. L. Keddie, "Film formation of latex," *Mater. Sci. Eng. R-Rep.*, vol. 21, no. 3, pp. 101 – 170, 1997.

[3] L. J. Procopio, G. Larson, and W. Rosano, "Low-voc waterborne coatings for use

in industrial maintenance painting," *JCT Coatings Tech*, vol. 4, no. 3, pp. 50–59, 2007.

[4] M. Huldén, "Hydrophobically modified urethane—ethoxylate (heur) associative thickeners 1. rheology of aqueous solutions and interactions with surfactants," *Colloids Surf., A*, vol. 82, no. 3, pp. 263–277, 1994.

[5] X.-X. Meng and W. B. Russel, "Structure and size of spherical micelles of telechelic polymers," *Macromolecules*, vol. 38, no. 2, pp. 593–600, 2005.

[6] K. Tanaka, Y. Fujii, H. Atarashi, K.-i. Akabori, M. Hino, and T. Nagamura, "Nonsolvents cause swelling at the interface with poly(methyl methacrylate) films," *Langmuir*, vol. 24, no. 1, pp. 296–301, 2008.

[7] W.-J. Lee, J.-G. Chang, and S.-P. Ju, "Hydrogen-bond structure at the interfaces between water/poly(methyl methacrylate), water/poly(methacrylic acid), and water/poly(2-aminoethylmethacrylamide)," *Langmuir*, vol. 26, no. 15, pp. 12640–12647, 2010.

[8] Y. Tateishi, N. Kai, H. Noguchi, K. Uosaki, T. Nagamura, and K. Tanaka, "Local conformation of poly(methyl methacrylate) at nitrogen and water interfaces," *Polym. Chem.*, vol. 1, no. 3, p. 303, 2010.

[9] E. R. Hatcher, O. Guvench, and A. D. MacKerell Jr, "Charmm additive all-atom force field for acyclic polyalcohols, acyclic carbohydrates, and inositol," *J. Chem. Theory Comput.*, vol. 5, no. 5, pp. 1315–1327, 2009.

[10] G. M. Torrie and J. P. Valleau, "Nonphysical sampling distributions in monte carlo free-energy estimation: Umbrella sampling," *J. Comput. Phys.*, vol. 23, no. 2, pp. 187–199, 1977.

[11] K. Vanommeslaeghe, E. Hatcher, C. Acharya, S. Kundu, S. Zhong, J. Shim, E. Darian, O. Guvench, P. Lopes, I. Vorobyov, and A. D. Mackerell, "Charmm general force field: A force field for drug-like molecules compatible with the charmm all-atom additive biological force fields," *J. Comput. Chem.*, vol. 31, no. 4, pp. 671–690, 2010.

[12] A. D. MacKerell, N. Banavali, and N. Foloppe, "Development and current status of the charmm force field for nucleic acids," *Biopolymers*, vol. 56, no. 4, pp. 257–265, 2000.

[13] W. L. Jorgensen and J. Tirado-Rives, "The opls [optimized potentials for liquid simulations] potential functions for proteins, energy minimizations for crystals of cyclic peptides and crambin," *J. Am. Chem. Soc.*, vol. 110, no. 6, pp. 1657–1666, 1988.

[14] R. Byrd, P. Lu, J. Nocedal, and C. Zhu, "A limited memory algorithm for bound constrained optimization," *SIAM J. Sci. Comput.*, vol. 16, no. 5, pp. 1190–1208, 1995.

[15] G. Bussi, D. Donadio, and M. Parrinello, "Canonical sampling through velocity rescaling," *J. Chem. Phys.*, vol. 126, no. 1, p. 014101, 2007.

[16] H. J. C. Berendsen, J. P. M. Postma, W. F. van Gunsteren, A. DiNola, and J. R. Haak, "Molecular dynamics with coupling to an external bath," *J. Chem. Phys.*, vol. 81, no. 8, pp. 3684–3690, 1984.

[17] M. Parrinello and A. Rahman, "Polymorphic transitions in single crystals: A new molecular dynamics method," *J. Appl. Phys.*, vol. 52, no. 12, pp. 7182–7190, 1981.

[18] B. Hess, H. Bekker, H. J. C. Berendsen, and J. G. E. M. Fraaije, "Lincs: A linear

solver for molecular simulations," *J. Comput. Chem.*, vol. 18, no. 12, pp. 1463–1472, 1997.

[19] T. Darden, D. York, and L. Pedersen, "Particle mesh ewald: An $n \cdot log(n)$ method for ewald sums in large systems," *J. Chem. Phys.*, vol. 98, no. 12, pp. 10089–10092, 1993.

[20] H. J. C. Berendsen, D. van der Spoel, and R. van Drunen, "Gromacs: A message-passing parallel molecular dynamics implementation," *Comput. Phys. Commun.*, vol. 91, no. 1-3, pp. 43–56, 1995.

[21] A.-C. Genix, A. Arbe, F. Alvarez, J. Colmenero, W. Schweika, and D. Richter, "Local structure of syndiotactic poly (methyl methacrylate). a combined study by neutron diffraction with polarization analysis and atomistic molecular dynamics simulations," *Macromolecules*, vol. 39, no. 11, pp. 3947–3958, 2006.

[22] J. G. Kirkwood and F. P. Buff, "The statistical mechanical theory of surface tension," *J. Chem. Phys.*, vol. 17, no. 3, p. 338, 1949.

[23] G. A. Chapela, G. Saville, S. M. Thompson, and J. S. Rowlinson, "Computer simulation of a gas/liquid surface. part 1," *J. Chem. Soc. Faraday Trans.*, vol. 73, no. 7, p. 1133, 1977.

[24] J. Mark, *Physical Properties of Polymers Handbook*. Springer, 2007.

[25] H. J. C. Berendsen, J. R. Grigera, and T. P. Straatsma, "The missing term in effective pair potentials," *J. Phys. Chem.*, vol. 91, no. 24, pp. 6269–6271, 1987.

[26] S. Miyamoto and P. A. Kollman, "Settle: An analytical version of the shake and rattle algorithm for rigid water models," *J. Comput. Chem.*, vol. 13, no. 8, pp. 952–962, 1992.

[27] J. Alejandre, D. J. Tildesley, and G. A. Chapela, "Molecular dynamics simulation of the orthobaric densities and surface tension of water," *J. Chem. Phys.*, vol. 102, no. 11, p. 4574, 1995.

[28] M. R. Farrow, P. J. Camp, P. J. Dowding, and K. Lewtas, "The effects of surface curvature on the adsorption of surfactants at the solid–liquid interface," *Phys. Chem. Chem. Phys.*, vol. 15, no. 28, pp. 11653–11660, 2013.

[29] D. J. Barlow, A.-M. Muslim, J. R. Webster, J. Penfold, C. M. Hollinshead, and M. J. Lawrence, "Molecular modelling of surfactant monolayers under constraints derived from neutron reflectance measurements," *Phys. Chem. Chem. Phys.*, vol. 2, no. 22, pp. 5208–5213, 2000.

[30] J. M. Castillo, M. Klos, K. Jacobs, M. Horsch, and H. Hasse, "Characterization of alkylsilane self-assembled monolayers by molecular simulation," *Langmuir*, vol. 31, no. 9, pp. 2630–2638, 2015.

[31] R. Godawat, S. N. Jamadagni, and S. Garde, "Characterizing hydrophobicity of interfaces by using cavity formation, solute binding, and water correlations," *Proc. Natl. Acad. Sci. U.S.A.*, vol. 106, no. 36, pp. 15119–15124, 2009.

[32] G. Hummer and S. Garde, "Cavity expulsion and weak dewetting of hydrophobic solutes in water," *Phys. Rev. Lett.*, vol. 80, no. 19, p. 4193, 1998.

[33] N. R. Tummala, S. Liu, D. Argyris, and A. Striolo, "Interfacial water properties in the presence of surfactants," *Langmuir*, vol. 31, no. 7, pp. 2084–2094, 2015.

[34] D. E. Rosenfeld and C. A. Schmuttenmaer, "Dynamics of the water hydrogen bond network at ionic, nonionic, and hydrophobic interfaces in nanopores and reverse micelles," *J. Phys. Chem. B*, vol. 115, no. 5, pp. 1021–1031, 2010.

[35] J. Boisson, G. Stirnemann, D. Laage, and J. T. Hynes, "Water reorientation dynamics in the first hydration shells of f- and i-," *Phys. Chem. Chem. Phys.*, vol. 13, no. 44, pp. 19895–19901, 2011.

[36] T. Ohto, A. Mishra, S. Yoshimune, H. Nakamura, M. Bonn, and Y. Nagata, "Influence of surface polarity on water dynamics at the water/rutile tio2 (110) interface.," *J. Phys. Condens. Matter*, vol. 26, no. 24, pp. 244102–244102, 2014.

CHAPTER III

Potentials of Mean Force and Escape Times of Surfactants from Micelles and Hydrophobic Surfaces Using Molecular Dynamics Simulations

This chapter is adapted with minor modifications from Ref[1].

3.1 Abstract

In this chapter, we calculate potentials of mean force (PMFs) and mean first passage times for a surfactant to escape a micelle, for both ionic sodium dodecyl sulfate (SDS) and nonionic ethoxylated alcohol (C12E5) micelles using both atomistic and coarse-grained molecular dynamics (MD) simulations. The PMFs are obtained by umbrella sampling and used in a Smoluchowski first-passage-time theory to obtain the times for a surfactant to escape a micelle. The calculated mean first passage time for an SDS molecule to break away from a micelle (with an aggregation number of 60) is around 2 μs, which is consistent with previous experimental measurements of the "fast relaxation time" for exchange of surfactants between the micellar phase and the bulk solvent. The corresponding escape time calculated for a nonionic ethoxylated alcohol C12E5, with the same tail length as SDS, is 60 μs, which is significantly longer than for SDS primarily because the PMF for surfactant desorption is about 3kT smaller than

for C12E5. We also show that two coarse-grained (CG) force fields, MARTINI and SDK, give predictions similar to the atomistic CHARMM force field for the nonionic C12E5 surfactant, but for the ionic SDS surfactant, the CG simulations give a PMF similar to that obtained with CHARMM only if long-range electrostatic interactions are included in the CG simulations, rather than using a shifted truncated electrostatic interaction. We also calculate that the mean first passage time for an SDS and a C12E5 to escape from a latex binder surface is of the order of milliseconds, which is more than 100 times longer than the time for escape from the micelle, indicating that in latex waterborne coatings, SDS and C12E5 surfactants likely bind preferentially to the latex polymer interface rather than form micelles, at least at low surfactant concentrations.

3.2 Introduction

There are two major kinetic processes by which micelles change size, governed respectively by what are called the "fast" and "slow" relaxation times, τ_1 and τ_2, respectively[2]. The fast relaxation time is the average time for surfactant exchange between micelles and the bulk solution, and is generally of the order of microseconds for small-molecule surfactants such as sodium dodecyl sulfate. The characteristic diffusion length in water, which is roughly equal to the average distance between two micelles, can be estimated from the equilibrium aggregation number and micelle diameter[3]. The second relaxation time is associated with micelle breakup and formation and is on the order of milliseconds to seconds[4, 5, 6]. The longer these relaxation times are, the more stable is the micelle, and the longer is the time it takes for processes such as wetting of fabrics and emulsification[2]. The fast relaxation time (τ_1) is typically detected by means of a temperature jump, ultrasonic absorption, EPR[7] or shock tube method, while the slow time constant (τ_2) has been detected by pressure and /or temperature jump experiments.[8, 9, 10, 11, 12]

Numerous theoretical models have been developed over the last few decades for the micellar kinetics. As summarized by Danov et al.[13], one of the earliest and best-known models of micelle kinetics, developed by Aniansson and Wall[14], can be used to predict the two relaxation times observed in ultrasound experiments for spatially uniform solutions. The model was further improved in several subsequent studies to explain experimental results for various micellar solutions[15, 16]. For example, in their first model[14] τ_1 was predicted to be independent of the total concentration of surfactants, which was in contrast to experimental observations. A linear dependence of $1/\tau_1$ on concentration was predicted in their later models[15, 16]. The theory of Aniansson and Wall, and improved versions of it, have shown success in predicting the results of numerous kinetic studies of micellar solutions. In 2001, Rusanov et al. [17, 18, 19] provided a thorough mathematical analysis of the micellization process, based on the Aniansson and Wall kinetic model, that outlines nine characteristic kinetic times of micellization in non-ionic surfactant solutions.

In the Aniansson and Wall model, the fast relaxation time τ_1 is controlled by the half-width of the distribution of micellar sizes, the stepwise dissociation rate constant, the total surfactant concentration, and the critical micelle concentration.

The fast time constant τ_1 can be further broken down into two sub-processes, i.e. the escape of a surfactant from its micelle, and the diffusion of the surfactant through the bulk solution to another micelle. Goldmints et al. [3] showed that for P85 (a PEO-PPO-PEO block copolymer $EO_{26}PO_{40}EO_{26}$,where the numbers are the degrees of polymerization of the blocks) the diffusion time for a surfactant molecule that has escaped a micelle through the solvent a distance comparable to the inter-micelle distance is 10 times smaller than τ_1. They therefore conclude that the escape of the surfactant from the micelle through the micellar corona must play an important role in the fast relaxation process.

The main purpose of the present work is to directly calculate the surfactant es-

cape time from the micelle, using molecular dynamic (MD) simulations, potentials of mean force (PMFs) along the surfactant escape coordinate using a weighted histogram method (WHAM), and a first passage time calculation. We also validate two commonly used coarse-grained force fields by comparing their predictions of their PMFs to that of an atomistic simulation. The coarse-grained models examined here are MARTINI, which on average groups four heavy atoms into one coarse-grained bead (i.e., a 4:1 mapping)[20], and the SDK model developed by Shinoda et al., which uses a 3:1 mapping, and improves the water/air surface tension predictions over those obtained from MARTINI [21, 22, 23]. Previous evaluations of coarse-grained force fields have been limited to their predictions of structural properties [21, 23, 24] (i.e. micelle size, shape and spatial distributions of different groups within the micelle), which are often fairly similar for various force fields, at least for spherical micelles. However, free energies and dynamic properties, such as the free energy for a surfactant to escape from its micelle, and the time scale of this process, have yet to be assessed for coarse-grained models, and will be computed in the following.

3.3 Theory

Because the time scale for micelle desorption is much longer than that for relaxation of velocity correlations, and therefore inertial effects can be neglected[25], the motion of the surfactant is governed by a Smoluchowski equation for the probability distribution p(x,t) of finding a surfactant at a position x at time t, namely

$$\frac{\partial p(x,t)}{\partial t} = \frac{\partial}{\partial x}\Big\{ D(x) e^{-W(x)/kT} \frac{\partial}{\partial x} [e^{W(x)/kT} p(x,t)] \Big\} \tag{3.1}$$

Here x is a positional order parameter used to characterize distance along the reaction coordinate, D(x) is the diffusivity landscape, and W (x) is the free energy landscape.

The mean first-passage time is given by[26]

$$\tau(x, x_f) = \int_{x}^{x_f} dx' \frac{exp[W(x')/kT]}{D(x')} \times \int_{x_0}^{x'} dx'' exp[-W(x'')/kT] \tag{3.2}$$

Here, $\tau(x, x_f)$ is here the average time it takes for a surfactant to travel from a position x (which is close to the COM of the micelle, and has the smallest free energy along the reaction coordinate) to position x_f, the final state. x_0 corresponds to a reflective boundary for the Smoluchowski equation, and in this study its value is set to be the smallest reaction coordinate (which corresponds to a high free energy).

3.4 Methods

3.4.1 Simulation of SDS micelle

All atomistic simulations were conducted using GROMACS, version 4.5.5[27], with the CHARMM force field[28]. In particular, the SDS was simulated using CHARMM27, and C12E5 using CHARMM c35r[29]. To simulate an SDS micelle, 60 SDS surfactants were pre-packed into a sphere, with their hydrophobic tails facing inward, using the Saff-Kuiijlaars method[30]. The pre-packed micelle was then placed in a cubic box of 8 nm on each side containing TIP3P water, to which neutralizing sodium ions were added. After a steepest-descent minimization followed by a short simulation for the micelle to reach its equilibrated shape, production MD simulations were conducted for 10 ns with a time step of 2 fs, during which V-rescale[31] and the Parrinello-Rahman barostat[32] were used to regulate temperature and pressure respectively, in an NPT ensemble[33].

The configuration at the end of an NPT trajectory was used as the initial structure for a "pulling" simulation, to generate the initial configurations for umbrella sampling within each window, defined below. The center of mass (COM) distances

between each surfactant and the rest of the micelle were calculated, and the surfactant molecule with the shortest COM distance from the rest of the micelle was selected and then pulled relatively rapidly away from the micelle over a 1 ns timescale using a spring constant of 1000 $kJ^{-1}nm^{-2}$ and a pulling rate of 0.004 nm ps^{-1}. This pulling was carried out to create a set of starting configurations, one for each "window" to be used in the weighted histogram free energy calculations described shortly. The pulling rate used in this stage is sufficiently slow to allow the average position of the surfactant to keep up with the position of the minimum in the pulling potential. The final center of mass distance between the pulled SDS molecule and the rest of the micelle was about 5nm. To generate the starting configurations for the umbrella sampling[34] windows to be used in subsequent parallel simultaneous runs on a multi-core computer, snapshots were taken from this "fast" pulling trajectory with uniform spacing of windows.

A total of 67 windows were used with a spacing of 0.06 nm COM separation between them. In each window, a 10 ns MD simulation was performed for umbrella sampling. A harmonic force with a force constant of 1200 $kJmol^{-1}nm^{-2}$ was applied for each umbrella-sampling window. To generate the potentials of mean force (PMFs), the weighed histogram analysis method (WHAM)[35] was used, specifically the Gromacs facility g_wham[36], as well as an in-house WHAM code.

Coarse-grained simulations of SDS micelles employed a similar procedure; time steps for the coarse-grained simulations were 10 fs, and the total duration of each production simulating was 100 ns for both MARTINI and SDK CG force fields for each umbrella-sampling window. The parameters for the SDK CG model were taken from the work published by Shinoda et al. in 2011[23, 37]. The sizes of the simulation boxes as well as the number of water molecules for all three force fields can be found in Table 3.1. All simulations were carried out at a temperature of 298K.

3.4.2 C12E5 micelle

A C12E5 micelle was created by pre-packing 54 surfactants into a spherical configuration. This aggregation number was chosen based on the work of M. Velinova et al., [38] who reported a mean aggregation number of 54 ± 1 from their simulation studies of C12E5 surfactants. We used three force fields (CHARMM, MARTINI, SDK) to simulate the micelle, in cubic simulation boxes; the sizes of these boxes and the numbers of water molecules in the box can be found in Table 3.1.

After a steepest descent minimization, production simulations were carried out for 10 ns for atomistic simulations or 100 ns for coarse-grained simulations to determine structural properties. Then after the 'pulling' process, a 10 ns or 100 ns umbrella sampling was conducted in each window for the atomistic force field and the coarse-grained force fields, respectively. An umbrella sampling window spacing of 0.06 nm was used for all simulations. The parameters for C12E5 micelle were adopted from CHARMM c35r[29]. The parameters for the SDK model were taken from ref. [37].

3.4.3 Latex binder slab simulations

In this study, a slab of random copolymer of methl methacrylate (MMA) /n-butyl acrylate (BA) with 1:1 molar ratio was used to represent the latex binder/water interface. The slab is comprised of 36 random copolymers each composing 10 MMA and 10 BA monomers simulated using CGenFF as been discussed in the work of Li et al. [39] The copolymer slab was placed in a middle of a simulation box with the z dimensions (13.3 nm) bigger than the x and y (5.1 nm) dimensions, and then water molecules (simulated with the TIP3P model) were introduced into the simulation box on both sides of the copolymer slab. After energy minimization, a 10 ns NPT simulation was conducted to equilibrate the copolymer/water system. A single surfactant molecule was then introduced into the simulation box near the interfacial region, and all overlapping water molecules were removed. The final system has 7341 water

molecules. Then a 20 ns NPT simulation was conducted at 298K. A snapshot at the end of the NPT simulation is shown in Fig. 3.1. After this, the SDS molecule was "pulled" away from the polymer/water interface to generate the initial configurations for each umbrella sampling window over a 1 ns timescale using a spring constant of $1000kJ^{-1}nm^{-2}$ and a pulling rate of 0.004 nm ps^{-1}. Snapshots were taken from this "fast" pulling trajectory with uniform spacing of windows of 0.6 nm. In each window, a 10 ns MD simulation was performed for umbrella sampling. A harmonic force with a force constant of 1200 kJ $mol^{-1}nm^{-2}$ was applied for each umbrella-sampling window. The potential of mean force (PMF) was then calculated using *g_wham*.

For each PMF curve, we calculated two PMFs, one using the first half of the simulations and the other using the last half of the simulations. The average and the standard deviation from the two PMFs are reported.

All computations were carried out on supercomputers provided by the Extreme Science and Engineering Discovery Environment (XSEDE), which is supported by National Science Foundation grant number OCI-1053575.

3.5 Results and discussion

3.5.1 Structural properties of SDS and C12E5 micelles

3.5.1.1 Micelle sizes and shapes

The micelle radii obtained using all three force fields are summarized in Table 3.2, where the radius (R_s) is defined as $Rs = \sqrt{\frac{5}{3}}R_g$, where R_g is the radius of gyration.

As shown in Table 3.2, for the nonionic C12E5 micelle, the radii for all three force fields agree with each other, within the standard error, while for the ionic SDS micelle, the MARTINI force field underestimates the radius by about 10%, presumably because the MARTINI force field uses a truncated electrostatic potential rather than the long-range electrostatics using particle mesh Ewald summation, which is used in

the CHARMM and SDK force fields. The truncated electrostatics allows head groups to approach each other more closely, shrinking the micelle radius. Another important structural property of interest is the shape of the micelle. Micelle deviation from sphericity depends on salt concentration, temperature and surfactant concentration and can be characterized by the eccentricity (e), which is defined using the three principal moments of inertia, as [40]

$$e = 1 - \frac{I_{min}}{I_{avg}} \tag{3.3}$$

where I_{avg} is the average of the three principal moments of inertia (namely, I_{min}, I_{mid} , I_{max}). Here, I_{min} is the smallest of the three moments of inertia and, I_{max} is the largest.

Table 3.2 shows that all three force fields predict a similar shape for the C12E5 micelle, while for the ionic micelle, the MARTINI force field overestimates the eccentricity of the micelle compared with the other two force fields. For atomistic simulations of SDS micelle, our results indicate a less spherical (more eccentric) micelle shape than found in some early, short, simulations (where I_{max}/I_{min} was reported to be 1.13 by Shelley et al. [41], 1.03 by MacKerell et al. [42] and 1.05 by Bruce et al. [43]). However, in a more recent study published in 2011 (using the GAFF force field), Palazzesi et al. reported an eccentricity of 0.154 [44], which is within the error bars of our simulation results.

3.5.1.2 Spatial distributions of chemical groups

In Fig. 3.3 we compare the distributions of distances of carbon atoms, sulfur atoms and sodium atoms from the COM of the SDS micelle from our work with those of Palazzesi et al.[44], who used the Generalized Amber Force Field (GAFF). All three force fields that we studied, and that of Palazzesi et al., result in a rapid fall-off

in hydrocarbon tail density between 15 to 21 Å from the micelle COM, while the sulfur atom density decreases rapidly between 20 and 25 Å. Although the CHARMM and MARTINI force field give generally good agreement with the results of Palazzesi et al., the SDK force field shows a deeper permeation of the sodium ions into the micelles than is shown by the other force fields, which was also reported in the first publication of the SDK model[23]. The shift (0.1 nm) is smaller than the CG particles size ($\sigma = 0.42$ nm), and therefore should be not considered very significant.

In Fig. 3.2, which is the corresponding characterization of the C12E5 micelle, all three force fields show that the most probable position for the tail group beads is about 1.3 nm from the COM of the micelle, while head group beads are most likely to be found around 1.9 nm from the COM.

3.5.2 Desorption energies and critical micelle concentrations

We here calculate the free energy of desorption of a surfactant from the micelle using umbrella sampling and the weighted histogram analysis method (WHAM). As discussed above, a single surfactant is "pulled away" from the rest of the micelle and the associated potential of mean force (PMF) is calculated during this process. The PMFs calculated using g_wham (and in the house WHAM code) are shown in Fig. 3.4. As shown in Fig. 3.4, the two coarse-grained force fields agree reasonably well with the atomistic force field from r=1.0 nm to r = 2.7 nm and the minimum of the potential of mean force occurs at r=1.6 nm for all three force fields, which is comparable to the radius of gyration Rg of the micelle, and indicates the most probable location for the center of mass of an SDS molecule within the micelle.

Above R = 3.5 nm, PMFs from all three force field start to decrease with increasing R. Part of this decrease is simply due to an entropic effect, i.e. the phase volume as a function of R is $4\pi R^2 dr$ where dr is the bin width, and a larger R value corresponds to a bigger volume than a smaller one.

To remove this entropic contribution, PMFs were corrected using $PMF_{corrected} = PMF_{original} + kTln(R^2)$ and re-plotted Fig.5. (Since the bin width dr is a constant, this and other multiplicative constants that go into the expression for the phase volume appear as additive constants once the logarithm is taken, and therefore are scaled out of the PMF when it is zeroed at its minimum.) Fig. 5 shows that, with this correction, the decrease in PMF at large R has disappeared for the MARTINI force field, but remains for the force fields with long-range electrostatics. Beyond the maximum at R= about 2.7 nm for CHARMM, where the PMF height of is about 10kT (k is Boltzmann's constant), the subsequent decrease in the PMF can be explained by the repulsion of the positively charged SDS molecule from the positively charged micelle, once the surfactant tail loses contact with the hydrophobic core of the micelle.

Thus, the difference between the PMF from the SDK and that from the MARTINI force field is explained by their different treatments of the electrostatic interactions. While the SDK force field employs PME electrostatics, the MARTINI force field uses a shifted cut-off scheme and therefore possibly underestimates the electrostatic contributions to the PMF. The surfactant desorption free energy estimated from the CMC of SDS[45] is $-kT\ln(CMC) = -kT\ln(8\times10^{-3}/55.5) \approx 9kT$, where the CMC has been converted to mole fraction. The desorption free energy obtained from the CMC is in reasonable agreement with the PMF height for pulling the SDS far from the micelle (well past the maximum) for both the CHARMM and SDK force fields.

PMFs calculated by atomistic and coarse-grained simulations of C12E5 (after phase volume correction) are shown in Fig 3.6. The PMFs for SDS and C12E5 micelles are similar for small pulling distances, as expected, since they have the same hydrophobic tail (C12), but for large pulling distances, the differences in PMFs are around 2-3 kT, owing to the difference in head groups. Similar to the PMFs for SDS desorption, the coarse-grained force fields, which are almost distinguishable for C12E5, give a higher free energy change, by about 2kT, than does the atomistic force

field. The PMF height estimated from the CMC of C12E5 [46] is $-kT\ln(CMC) = -kT\ln(7\times10^{-5}/55.5) \approx 14kT$, which is between the results of the CG force fields and atomistic CHARMM force fields.

Thus, for the nonionic micelle, the SDK and MARTINI PMFs agree, while for ionic surfactant, they differ somewhat, presumably due to their different treatment of electrostatic interactions. To validate that the difference is due to the modeling of electrostatic interactions, we also studied sodium octyl sulfate (SOS), a surfactant with a shorter, 8-carbon hydrocarbon tail than the 12-carbon tail of the SDS surfactant. As a result of the shorter tail, SOS is shed from the micelle much quicker than is SDS and an equilibrium distribution of micelle sizes can be achieved in CG simulations of modest duration. In fact, the exchange process by which SOS surfactants leave and reenter the micelles can be observed directly in CG simulations. Starting with an SOS micelle of aggregation number of 25 in a simulation box of 6nm $\times$ 6nm $\times$ 6nm, we tracked each SOS surfactant and calculated the fraction of time that it is absent from the micelle, where the surfactant is "absent" if all its hydrophobic tail CG beads are separated from the hydrophobic tail beads of the surfactants inside the micelle by at least 0.75nm[37]. As can be seen in Table 3, the average SOS surfactant is outside of the micelle only 2% of the time in the MARTINI model, but is absent 14% of the time in the SDK model. Additionally, we find that the method of implementation of the electrostatic interaction greatly affects the surfactant equilibrium distribution between micelle and free solution. As stated above, the MARTINI model uses a shifted cut-off of 1.2 nm, while the SDK model uses particle-mesh Ewald (PME) electrostatics. If we change the PME electrostatics to a shifted cut-off of 1.5 nm in the SDK model, the probability of SOS surfactant being an isolated monomer drops from 14% to around 5%, which is much closer to that of the MARTINI force field. On the other hand, if we replace the PME with the shifted cut-off in the MARTINI force field, the probability that an SOS surfactant is an isolated monomer increases to 8%,

which is closer to that of the SDK model. We note here that the implementation of the shifted cut-off in the MARTINI force fields speeds up the simulation but slows down the shedding kinetics of surfactants from the micelle.

3.5.3 Diffusion coefficient and mean first passage time

The free surfactant diffusion coefficient was obtained by simulating a single surfactant molecule in a water box with periodic boundary conditions. To take into account of the effect of the finite size of the simulation system on the diffusion coefficient, the Yeh-Hummer correction [47] was performed.

$$D_{sim} = D_{PBC} + \frac{k_B T \zeta}{6\pi\eta L} \tag{3.4}$$

In Equation 3.4, D_{PBC} is the diffusion coefficient calculated from a simulation with periodic boundary conditions, which could be calculated from a plot of the mean square displacement against time interval. ζ is a constant of 2.837297, k_B is the Boltzmann constant, T is the temperature, η is the viscosity, and L is the length of the cubic simulation box. To take into the account of the low viscosity of TIP3P water model, Equation 3.4 is further modified as below [48].

$$D_{sim} = [D_{PBC} + \frac{k_B T \zeta}{6\pi\eta L}] \times 0.375 \tag{3.5}$$

$$\eta = \eta_{TIP3P}(1 = 2.5\phi) \tag{3.6}$$

Here, the scaling factor of 0.375 is calculated from η_{TIP3P}/η_w, where $\eta_{TIP3P} = 0.35$ cP and $\eta_w = 0.93$ cP are the viscosity calculated using TIP3P water model and the experimental viscosity of water at room temperature respectively, and ϕ is the volume fraction of the solute. Using these equations, the diffusion coefficients of surfactants are calculated to be D $=0.74 \pm 0.06 \times 10^{-5}$ cm^2/s for SDS and D $=0.47 \pm 0.03 \times 10^{-5}$ cm^2/s for C12E5. The diffusion coefficient of SDS is consistent with

experimental results of E. Sutherland et al., who reported D = $0.80 \times 10^{-5} cm^2/s$ for SDS free monomers [49], using dynamic light scattering at 25 °C and of Deng et al.[50] who reported $D = 0.836 \times 10^{-5} cm^2/s$ for SDS monomers at 25 °C using Taylor dispersion measurements.

The free monomer diffusion coefficient for C12E5 has not been reported; however, the monomer diffusion coefficient of C12E8 was estimated to be $0.35 \times 10^{-5} cm^2/s$ at 25° C [51] , $0.17 \times 10^{-5} cm^2/s$ at 5 ° C , and $0.90 \times 10^{-5} cm2/s$ at 70° C[52], and the diffusion coefficient of C12E5 calculated by the current study has the same magnitude with these estimated coefficients. These diffusion coefficients are only rough approximations to the diffusion coefficients for migration of the surfactant through the corona region of the micelle. More precise values would depend on the reaction coordinate and we do not attempt to calculate them here.

Inserting the PMF profiles (without the phase space correction) and the above diffusion coefficient into Equation 2, one obtains the mean first passage times for a surfactant to travel from the position with the lowest free energy to a distance R from the center of mass of the micelle, which is plotted in Fig.3.7 for both SDS and C12E5 micelles simulated using the CHARMM force field. The mean time for an SDS molecule to travel 3.5 nm away from COM of micelle is around 2.0 μs, while for C12E5 surfactant to move 4.5 nm away from COM of micelle is around 60 μs. Beyond these positions (3.5 nm for SDS and 4.5 nm for C12E5), which correspond roughly to the positions at which the PMFs reach their plateaus, the mean first passage times level off. Note that it takes a C12E5 surfactant about more than 10 times longer to escape the micelle than it does for an SDS surfactant to escape its micelle, due to the higher (3kT higher) free energy change the C12E5 surfactant must overcome to escape the micelle.

Lang et al. [4] demonstrated that $1/\tau_1$ increases roughly linearly with overall surfactant concentration, with a value of $\tau_1 = 7.1$ μs at an SDS concentration of

$14 \times 10^{-3} M/L$, and $\tau_1 = 20$ μs at 9×10^{-3}M/L. The first passage time calculated here is of the same order of magnitude as these experimental results, and is in fact closer to the experimental for the higher surfactant concentration, where the escape time of the surfactant from the micelle, rather than time of diffusion through the solvent, should dominate τ_1. The above comparison indicates that the first passage time of the surfactant is likely closely related to the micellar fast relaxation times obtained experimentally via temperate jump and shock tube methods.

3.5.4 Surfactant escape time from latex copolymer surface

The same method of calculating the mean first passage time can be applied to other problems. For example, surfactants such as SDS are commonly used in waterborne coatings to improve shelf life, mechanical stability, freeze-thaw stability and elasticity[53]. The comparison of the time it takes for a surfactant to escape from the latex binder to that escaping from the micelle is of interest as it could reveal the distribution of surfactants in the waterborne coating system. Fig. 8 shows the potential of mean force profile for pulling an SDS or a C12E5 surfactant from the latex surface along the z axis (0 is the center of mass of copolymer slab in the simulation).

Inserting this PMF into equation 2, we obtain the mean first passage time profile for an SDS or a C12E5 to escape from the latex surface, and compare these profiles with that of an SDS molecule or C12E5 molecule escaping from the micelle as plotted in Fig. 3.9. Fig. 3.9 shows that the time it takes for a surfactant to break away from the latex surface is around a millisecond, which is much longer than for the escape process from a micelle. The differences in escape times indicate that SDS or C12E5 surfactants are more likely to reside on the latex binder surface than to form micelles in waterborne coatings when the total concentration of surfactants is low.

3.6 Conclusions

We have compared the predictions of MD simulations using two coarse-grained models, namely the SDK model and MARTINI model, to that of the atomistic CHARMM force field for SDS and CHARMMc35r for C12E5. We compared the micelle density distributions of tail and head groups and the potentials of mean force (PMFs) for a surfactant to leave the micelle, where we took the micelle aggregation numbers to be 60 and 54, respectively, for SDS and C12E5 micelles. The predictions of the SDK model agree reasonably well with those of the atomistic force field for both ionic and nonionic micelles. The MARTINI predictions agree with those of CHARMM for the nonionic surfactant, but show poorer agreement for the ionic surfactant. The MARTINI model underestimates the radius and eccentricity of the SDS micelle, and also fails to generate the correct shape of the PMF for desorption of a surfactant from a micelle at large distances from the micelle primarily because of its use of a shifted cut-off to describe electrostatic interactions rather than the more accurate long-range Particle Mesh Ewald (PME) interactions used in the SDK force field. Replacing the cut-off scheme with PME electrostatics greatly improves the performance of the MARTINI model at the cost of longer run times. Using the PMF, the mean first passage time for exit of an SDS ionic surfactant to a distance of around 4 nm from the micelle center of mass is around 2 μs, which is a factor of 30 smaller than that for a nonionic C12E5 surfactant with the same tail length. The surfactant escape time from the micelle is of the same magnitude with the experimental fast relaxation times. The escape time for an SDS or a C12E5 molecule from a PMMA/PBA latex binder surface is more than100 times longer than that from the micelle, which indicates that in waterborne coating systems, SDS or C12E5 surfactants are more likely to be adsorbed onto the latex surfaces than to form micelles at low concentrations.

Table 3.1: Simulation box sizes and total number of water molecules for SDS and C12E5 simulations using three force fields

	CHARMM		MARTINI		SDK	
	SDS	C12E5	SDS	C12E5	SDS	C12E5
box size (nm)	7.95	10.81	10.19	11.80	11.78	11.77
water molecules	15787	40490	8605×4	13417×4	17987 × 3	17854 × 3

Table 3.2: Radii, ratios of principal moments and eccentricities for SDS and C12E5 micelles using three force fields

	R_s (nm)		I_{max}/I_{mid}		I_{mid}/I_{min}		e	
	SDS	C12E5	SDS	C12E5	SDS	C12E5	SDS	C12E5
CHARMM	2.10	2.35	1.27	1.28	1.17	1.18	0.12	0.13
MARTINI	1.90	2.31	1.43	1.20	1.27	1.11	0.18	0.093
SDK	2.10	2.36	1.28	1.25	1.17	1.14	0.12	0.11

Table 3.3: Average probability for a surfactant to be in the bulk for a simulation of 25 SOS surfactant molecules in a 6 nm × 6 nm × 6 nm box

	SDK(PME)	MARTINI (Cut-off)	MARTINI (PME)	SDK (Cut-off)
Probability	14.3%	2.44%	7.94%	5.10%

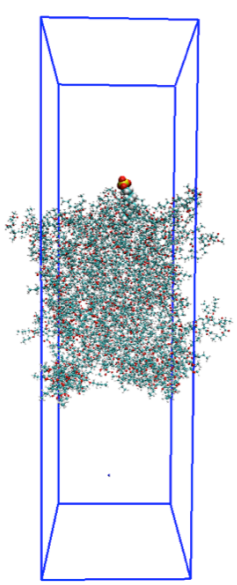

Figure 3.1: Snapshot of the latex polymer slab and SDS before the pulling experiment. Waters are removed for clarity.

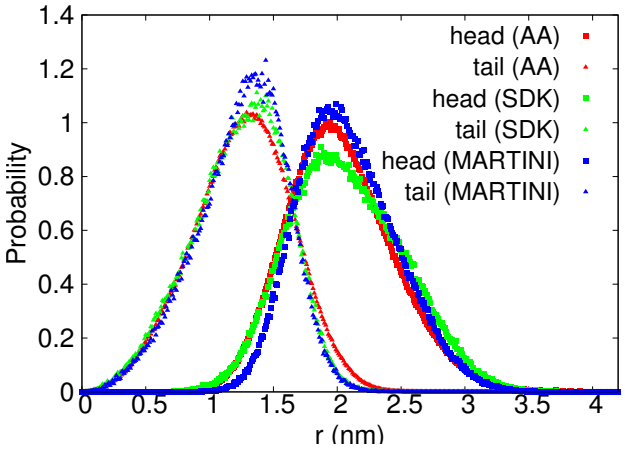

Figure 3.2: Probability distribution of the distance of head or tail groups to the COM of the micelle. Filled triangles represent tail groups, while filled squares represent head groups.

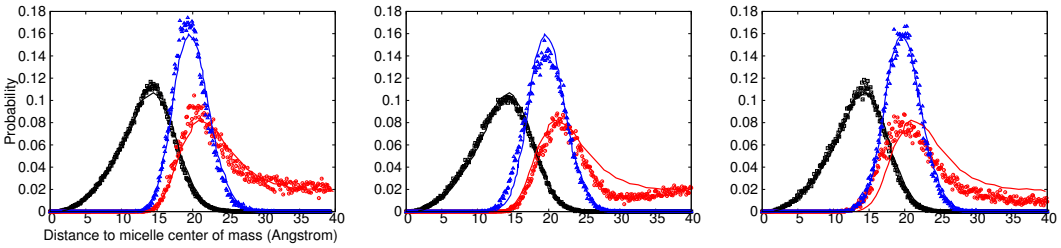

Figure 3.3: Probability distributions of distances of carbon (black), sulfur (blue) and sodium (red) atoms from the micelle COM. Symbols are from the current work and lines are from reference [44].

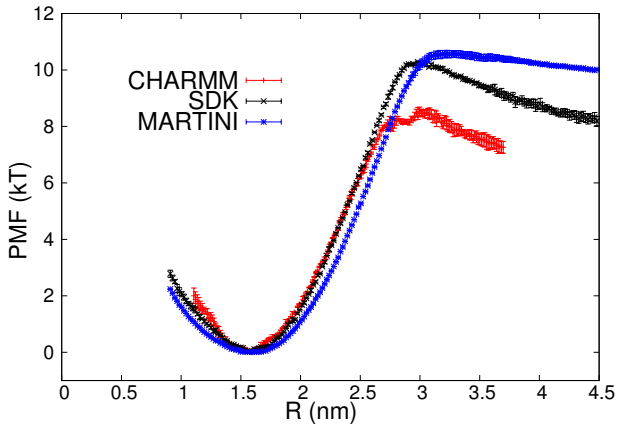

Figure 3.4: Potentials of mean force along the reaction coordinate for an SDS surfactant pulled from the COM of the rest of the micelle, using the CHARMM, MARTINI and SDK force fields. The error bars indicate the standard deviations of the values.

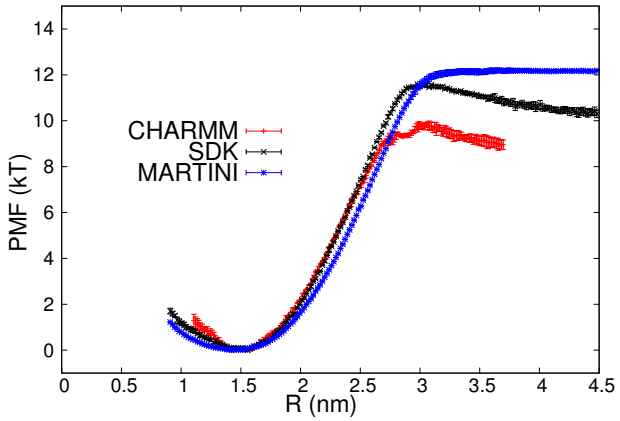

Figure 3.5: The same as Fig.3.4,except with spherical phase volume corrections, $PMF_{corrected} = PMF_{original} + 2kTln(R)$ as described in the text. The error bars indicate the standard deviations of the values.

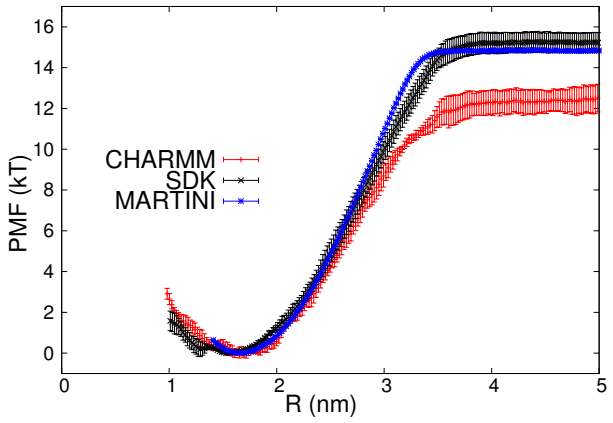

Figure 3.6: The same as Fig.3.5, except for a C12E5 surfactant pulled away from the COM of a C12E5 micelle. The error bars indicate the standard deviations of the values.

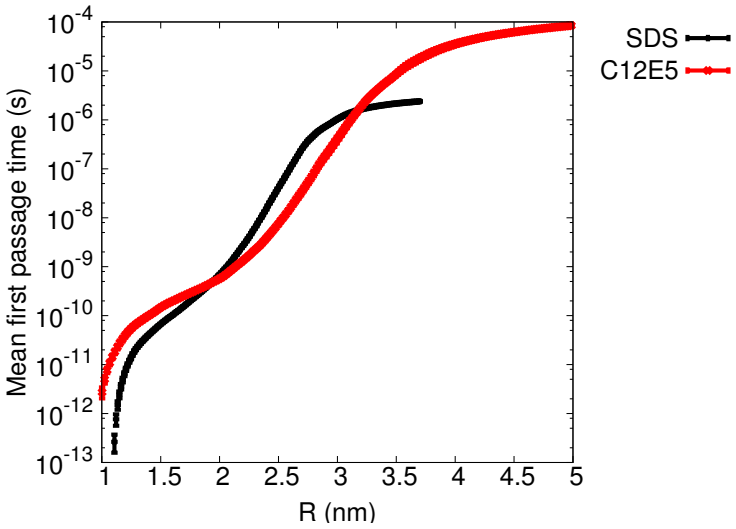

Figure 3.7: Mean first passage time profile of a surfactant escaping an SDS micelle and a C12E5 micelle.

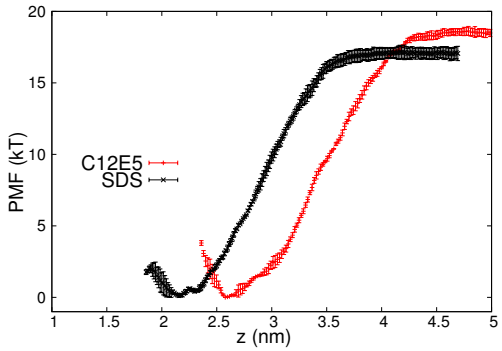

Figure 3.8: Potential of mean force along the reaction coordinate of SDS and C12E5 surfactants pulled away a latex polymer surface, with CHARMM force field.

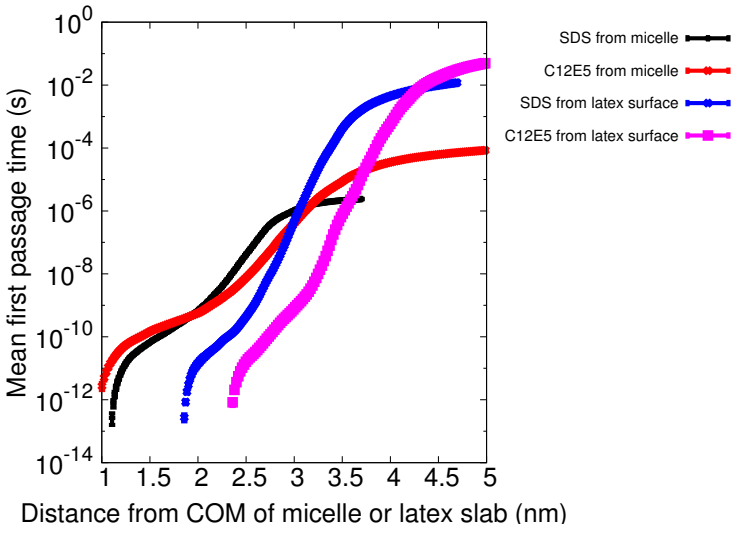

Figure 3.9: Mean first passage time profile of a surfactant escaping an SDS or C12E5 micelle and from the latex polymer surface.

Bibliography

[1] F. Yuan, S. Wang, and R. G. Larson, "Potentials of mean force and escape times of surfactants from micelles and hydrophobic surfaces using molecular dynamics simulations," *Langmuir*, 2015.

[2] A. Patist, J. R. Kanicky, P. K. Shukla, and D. O. Shah, "Importance of micellar kinetics in relation to technological processes," *J. Colloid Interface Sci.*, vol. 245, no. 1, pp. 1–15, 2002.

[3] I. Goldmints, J. F. Holzwarth, K. A. Smith, and T. A. Hatton, "Micellar dynamics in aqueous solutions of peo-ppo-peo block copolymers," *Langmuir*, vol. 13, no. 23, pp. 6130–6134, 1997.

[4] R. Zana, "Chemical relaxation studies of micellar equilibria," in *Chemical and Biological Applications of Relaxation Spectrometry*, pp. 139–141, Springer, 1975.

[5] S. Oh and D. Shah, "The effect of micellar lifetime on the rate of solubilization and detergency in sodium dodecyl sulfate solutions," *J. Am. Oil Chem. Soc.*, vol. 70, no. 7, pp. 673–678, 1993.

[6] A. Patist, B. Jha, S.-G. Oh, and D. Shah, "Importance of micellar relaxation time on detergent properties," *J. Surfactants Deterg.*, vol. 2, no. 3, pp. 317–324, 1999.

[7] K. Fox, "Determination of the monomer-micelle exchange frequency of a paramagnetic surfactant," *Trans. Faraday Soc.*, vol. 67, pp. 2802–2809, 1971.

[8] A. D. James, B. H. Robinson, and N. C. White, "Dynamics of small molecule-micelle interactions: Charge and ph effects on the kinetics of the interaction of dyes with micelles," *J. Colloid Interface Sci.*, vol. 59, no. 2, pp. 328–336, 1977.

[9] C. Tondre, J. Lang, and R. Zana, "On the use of dyes for the kinetic study of micellar equilibria," *J. Colloid Interface Sci.*, vol. 52, no. 2, pp. 372–379, 1975.

[10] M. Frindi, B. Michels, and R. Zana, "Ultrasonic absorption studies of surfactant exchange between micelles and bulk phase in aqueous micellar solutions of nonionic surfactants with a short alkyl chain. 3. surfactants with a sugar head group," *J. Phys. Chem.*, vol. 96, no. 20, pp. 8137–8141, 1992.

[11] S. Kato, S. Harada, and H. Sahara, "Ultrasonic relaxation and volumetric studies of the micelle/monomer exchange process in aqueous solutions of the nonionic surfactants c7e4, c8e4, and c8e5," *J. Phys. Chem.*, vol. 99, no. 33, pp. 12570–12575, 1995.

[12] T. Yasunaga, H. Oguri, and M. Miura, "Acoustic study on the kinetics for the dissociation-recombination reaction between micelle and counterion in sodium dodecyl sulfate solution," *J. Colloid Interface Sci.*, vol. 23, no. 3, pp. 352–357, 1967.

[13] K. Danov, P. Kralchevsky, N. Denkov, K. Ananthapadmanabhan, and A. Lips, "Mass transport in micellar surfactant solutions: 1. relaxation of micelle concentration, aggregation number and polydispersity," *Adv. Colloid Interface Sci.*, vol. 119, no. 1, pp. 1–16, 2006.

[14] E. Aniansson and S. N. Wall, "Kinetics of step-wise micelle association," *J. Phys. Chem.*, vol. 78, no. 10, pp. 1024–1030, 1974.

[15] E. Aniansson, S. Wall, M. Almgren, H. Hoffmann, I. Kielmann, W. Ulbricht, R. Zana, J. Lang, and C. Tondre, "Theory of the kinetics of micellar equilibria and quantitative interpretation of chemical relaxation studies of micellar solutions of ionic surfactants," *J. Phys. Chem.*, vol. 80, no. 9, pp. 905–922, 1976.

[16] S. N. Wall and G. E. A. Aniansson, "Numerical calculations on the kinetics of stepwise micelle association," *J. Phys. Chem.*, vol. 84, no. 7, pp. 727–736, 1980.

[17] F. Kuni, A. Grinin, A. Shchekin, and A. Rusanov, "Thermodynamic and kinetic foundations of the micellization theory. 3. initial stages of micellization," *Colloid J.*, vol. 62, no. 4, pp. 451–456, 2000.

[18] F. Kuni, A. Grinin, A. Shchekin, and A. Rusanov, "Thermodynamic and kinetic foundations of the micellization theory: 4. kinetics of establishment of equilibrium in a micellar solution," *Colloid J.*, vol. 63, no. 2, pp. 197–204, 2001.

[19] F. Kuni, A. Rusanov, A. Grinin, and A. Shchekin, "Thermodynamic and kinetic foundations of the micellization theory: 5. hierarchy of kinetic times," *Colloid J.*, vol. 63, no. 6, pp. 723–730, 2001.

[20] S. J. Marrink, H. J. Risselada, S. Yefimov, D. P. Tieleman, and A. H. de Vries, "The martini force field: coarse grained model for biomolecular simulations," *J. Phys. Chem. B*, vol. 111, no. 27, pp. 7812–7824, 2007.

[21] W. Shinoda, R. DeVane, and M. L. Klein, "Coarse-grained molecular modeling of non-ionic surfactant self-assembly," *Soft Matter*, vol. 4, no. 12, pp. 2454–2462, 2008.

[22] X. He, W. Shinoda, R. DeVane, and M. L. Klein, "Exploring the utility of coarse-grained water models for computational studies of interfacial systems," *Mol. Phys.*, vol. 108, no. 15, pp. 2007–2020, 2010.

[23] W. Shinoda, R. DeVane, and M. L. Klein, "Coarse-grained force field for ionic surfactants," *Soft Matter*, vol. 7, no. 13, pp. 6178–6186, 2011.

[24] S. Jalili and M. Akhavan, "A coarse-grained molecular dynamics simulation of a

sodium dodecyl sulfate micelle in aqueous solution," *Colloids Surf., A*, vol. 352, no. 1, pp. 99–102, 2009.

[25] S. Izrailev, S. Stepaniants, M. Balsera, Y. Oono, and K. Schulten, "Molecular dynamics study of unbinding of the avidin-biotin complex," *Biophys. J.*, vol. 72, no. 4, pp. 1568–1581, 1997.

[26] D. J. Beltran-Villegas, R. M. Sehgal, D. Maroudas, D. M. Ford, and M. A. Bevan, "A smoluchowski model of crystallization dynamics of small colloidal clusters," *J. Chem. Phys.*, vol. 135, no. 15, p. 154506, 2011.

[27] S. Pronk and E. Lindahl, "Gromacs 4.5: a high-throughput and highly parallel open source molecular simulation toolkit," *Bioinformatics*, vol. 29, no. 7, pp. 845–854, 2013.

[28] P. Bjelkmar, P. Larsson, M. A. Cuendet, B. Hess, and E. Lindahl, "Implementation of the charmm force field in gromacs: Analysis of protein stability effects from correction maps, virtual interaction sites, and water models," *J. Chem. Theory Comput.*, vol. 6, no. 2, pp. 459–466, 2010.

[29] H. Lee, R. M. Venable, A. D. MacKerell Jr, and R. W. Pastor, "Molecular dynamics studies of polyethylene oxide and polyethylene glycol: hydrodynamic radius and shape anisotropy," *Biophys. J.*, vol. 95, no. 4, pp. 1590–1599, 2008.

[30] E. B. Saff and A. B. Kuijlaars, "Distributing many points on a sphere," *Math. Intell.*, vol. 19, no. 1, pp. 5–11, 1997.

[31] G. Bussi, D. Donadio, and M. Parrinello, "Canonical sampling through velocity rescaling," *J. Chem. Phys.*, vol. 126, no. 1, p. 014101, 2007.

[32] M. Parrinello and A. Rahman, "Polymorphic transitions in single crystals: A new molecular dynamics method," *J. Appl. Phys.*, vol. 52, p. 7182, 1981.

[33] J. A. Lemkul and D. R. Bevan, "Assessing the stability of alzheimer's amyloid protofibrils using molecular dynamics," *J. Phys. Chem. B*, vol. 114, no. 4, pp. 1652–1660, 2010.

[34] G. M. Torrie and J. P. Valleau, "Nonphysical sampling distributions in monte carlo free-energy estimation: Umbrella sampling," *J. Comput. Phys.*, vol. 23, no. 2, pp. 187–199, 1977.

[35] S. Kumar, J. M. Rosenberg, D. Bouzida, R. H. Swendsen, and P. A. Kollman, "The weighted histogram analysis method for free-energy calculations on biomolecules. i. the method," *J. Comput. Chem.*, vol. 13, no. 8, pp. 1011–1021, 1992.

[36] J. S. Hub, B. L. De Groot, and D. Van Der Spoel, "g_wham:a free weighted histogram analysis implementation including robust error and autocorrelation estimates," *J. Chem. Theory Comput.*, vol. 6, no. 12, pp. 3713–3720, 2010.

[37] D. N. LeBard, B. G. Levine, P. Mertmann, S. A. Barr, A. Jusufi, S. Sanders, M. L. Klein, and A. Z. Panagiotopoulos, "Self-assembly of coarse-grained ionic surfactants accelerated by graphics processing units," *Soft Matter*, vol. 8, no. 8, pp. 2385–2397, 2012.

[38] M. Velinova, D. Sengupta, A. V. Tadjer, and S.-J. Marrink, "Sphere-to-rod transitions of nonionic surfactant micelles in aqueous solution modeled by molecular dynamics simulations," *Langmuir*, vol. 27, no. 23, pp. 14071–14077, 2011.

[39] Z. Li, F. Yuan, K. A. Fichthorn, S. T. Milner, and R. G. Larson, "Molecular view of polymer/water interfaces in latex paint," *Macromolecules*, vol. 47, no. 18, pp. 6441–6452, 2014.

[40] S. Salaniwal, S. Cui, H. Cochran, and P. Cummings, "Molecular simulation of

a dichain surfactant/water/carbon dioxide system. 1. structural properties of aggregates," *Langmuir*, vol. 17, no. 5, pp. 1773–1783, 2001.

[41] J. Shelley, K. Watanabe, and M. L. Klein, "Simulation of a sodium dodecylsulfate micelle in aqueous solution," *Int. J. Quantum Chem.*, vol. 38, no. S17, pp. 103–117, 1990.

[42] A. D. MacKerell Jr, "Molecular dynamics simulation analysis of a sodium dodecyl sulfate micelle in aqueous solution: decreased fluidity of the micelle hydrocarbon interior," *J. Phys. Chem.*, vol. 99, no. 7, pp. 1846–1855, 1995.

[43] C. D. Bruce, M. L. Berkowitz, L. Perera, and M. D. Forbes, "Molecular dynamics simulation of sodium dodecyl sulfate micelle in water: micellar structural characteristics and counterion distribution," *J. Phys. Chem. B*, vol. 106, no. 15, pp. 3788–3793, 2002.

[44] F. Palazzesi, M. Calvaresi, and F. Zerbetto, "A molecular dynamics investigation of structure and dynamics of sds and sdbs micelles," *Soft Matter*, vol. 7, no. 19, pp. 9148–9156, 2011.

[45] A. Dominguez, A. Fernandez, N. Gonzalez, E. Iglesias, and L. Montenegro, "Determination of critical micelle concentration of some surfactants by three techniques," *J. Chem. Educ.*, vol. 74, no. 10, p. 1227, 1997.

[46] K. Shinzawa-Itoh, H. Ueda, S. Yoshikawa, H. Aoyama, E. Yamashita, and T. Tsukihara, "Effects of ethyleneglycol chain length of dodecyl polyethyleneglycol monoether on the crystallization of bovine heart cytochrome oxidase," *J. Mol. Biol.*, vol. 246, no. 5, pp. 572–575, 1995.

[47] I.-C. Yeh and G. Hummer, "System-size dependence of diffusion coefficients and viscosities from molecular dynamics simulations with periodic boundary conditions," *J. Phys. Chem. B*, vol. 108, no. 40, pp. 15873–15879, 2004.

[48] E. R. Hatcher, O. Guvench, and A. D. MacKerell Jr, "Charmm additive all-atom force field for acyclic polyalcohols, acyclic carbohydrates, and inositol," *J. Chem. Theory Comput.*, vol. 5, no. 5, pp. 1315–1327, 2009.

[49] E. Sutherland, S. M. Mercer, M. Everist, and D. G. Leaist, "Diffusion in solutions of micelles. what does dynamic light scattering measure?," *J. Chem. Eng. Data*, vol. 54, no. 2, pp. 272–278, 2008.

[50] Z. Deng, H. Lü, and D. G. Leaist, "Mutual diffusion coefficients and resistance coefficients for aqueous solutions of sodium alkanoate surfactants," *J. Chem. Eng. Data*, vol. 41, no. 2, pp. 214–217, 1996.

[51] P. G. Nilsson, H. Wennerstroem, and B. Lindman, "Structure of micellar solutions of nonionic surfactants. nuclear magnetic resonance self-diffusion and proton relaxation studies of poly (ethylene oxide) alkyl ethers," *J. Phys. Chem.*, vol. 87, no. 8, pp. 1377–1385, 1983.

[52] M. Jonströmer, B. Jönsson, and B. Lindman, "Self-diffusion in nonionic surfactant-water systems," *J. Phys. Chem.*, vol. 95, no. 8, pp. 3293–3300, 1991.

[53] E. W. Hagan, M. N. Charalambides, C. R. Young, T. J. Learner, and S. Hackney, "Viscoelastic properties of latex paint films in tension: Influence of the inorganic phase and surfactants," *Prog. Org. Coat.*, vol. 69, no. 1, pp. 73–81, 2010.

CHAPTER IV

Multi-scale Molecular Dynamics Simulations of Model Hydrophobically Modified Ethylene Oxide Urethane (HEUR) Micelles

4.1 abstract

The flower-like micelles of various aggregation numbers of a model hydrophobically modified ethylene oxide urethane (HEUR) molecule $C_{16}EO_{45}C_{16}$ and their corresponding star-like micelles containing the surfactants $C_{16}EO_{22}$ and $C_{16}EO_{23}$, were studied using both atomistic and coarse-grained molecular dynamic (MD) simulations. We use free energies from umbrella sampling to calculate the size distribution of micelle sizes and the average time for escape of a hydrophobic group from the micelle. Using the coarse-grained MARTINI forcefield, the most probable size of the model HEUR molecule is thereby determined to be about 80 hydrophobes per micelle, and the average hydrophobe escape time to be about 0.1 second, both consistent with previous experimental studies. Atomistic simulations reveal that hydrogen bond formation and mean life time of hydration waters of the poly(ethylene oxide) (or PEO) groups are location dependent in the HEUR micelle, with PEO groups immediately adjacent to the C16 groups forming the fewest hydrogen bonds with water and having hydration waters with longer lifetime than PEO groups located further away from the

C16 groups.

4.2 Introduction

Associative polymers or "associative thickeners" have attracted much interest in recent years. These water-soluble block copolymers contain both hydrophilic and hydrophobic moieties and are widely used as rheological modifiers in various industrial applications for example paints, food, cosmetics and drug delivery systems[1, 2, 3]. Among the most commonly used thickeners are hydrophobically modified ethylene oxide urethanes (HEURs) which are known to assemble into flower-like micelles in aqueous solutions[4, 5, 6] above the critical micelle concentration (CMC). Telechelic HEUR polymers, which have associating groups only at their chain-ends, have unique flow properties in solution, showing Newtonian behavior at low shear rates, followed by a shear thickening regime, and then shear thinning at high shear rates, as summarized by Tripathi et al. [6]. Fig.4.1 (top image) shows the structure of a typical commercially available HEUR molecule.

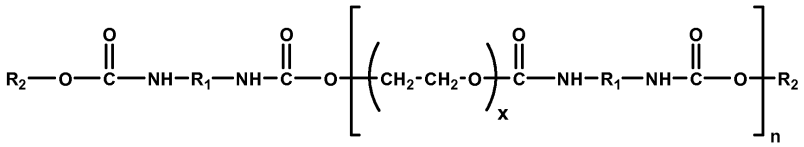

$CH_3\text{-}\left(CH_2\right)_{15}\text{-}(CH_2\text{-}O\text{-}CH_2)_{45}\text{-}\left(CH_2\right)_{15}\text{-}CH_3$

Figure 4.1: Top: An example of a commercially available HEUR molecule; R_2 is a hydrophobic group. Bottom: Simplified short HEUR molecule simulated in this study

The chemical formula for a model telechelic HEUR is $CH_3\text{-}(CH_2)_i\text{-}(CH_2OCH_2)_j\text{-}(CH_2)_i\text{-}CH_3$. Here the subscripts j and i+1 are the degrees of polymerization of the main chain poly(ethylene oxide) or PEO, and of the hydrophobe, respectively; i+1 typically varies from 8 to 18, and j from 500 to 9,000 [7]. Above the critical aggregation concentration, the HEUR molecules form flower-like aggregates with each

HEUR looping into a "petal". At higher concentrations, the coronas of the micelles begin to overlap, leading to the formation of bridges between the micelles[7]. The structure of these aggregates profoundly affects the macroscopic properties, such as rheology[8]. The viscosity remains low in the pre-aggregate and the non-interacting micelle regimes, but increases very rapidly when bridging between the micelles starts. This study will focus on the non-interacting micelle regime.

The formation of the flower-like micelle structure results from two competitive effects: in water, the hydrophilic PEOs tend to dissolve and the hydrophobes tend to aggregate; the hydrophobe aggregation number (n, number of hydrophobic groups per micelle) and the CMC depend on the relative length of the hydrophobic and hydrophilic block. For a given soluble block length, n increases and the CMC decreases with increasing the length of the hydrophobe [9, 10, 11]. Various techniques have been employed to determine the aggregation number and the CMC, such as fluorescence quenching[12, 13], static light scattering [14, 15, 16, 17] neutron scattering[18] and a combination of dynamic light scattering and viscometry[19]. Unfortunately, the results from these different techniques usually disagree somewhat with each other. The aggregation number measured by static light scattering is slightly lower than from dynamic light scattering and viscometry, while the results from static fluorescence are lowest of all[12, 20, 8].

On the other hand, there have been a number of theoretical works on micelle formation and size distribution. In particular, Hoeve and Benson[21] and Poland and Scheraga [22, 23] developed statistical-thermodynamic models in which the free energy of formation of micelles is decomposed into individual contributions including the free energy for transferring the surfactant tail from water to micelle and the surface free energy associated with the exposed hydrophobic surface of the micelle[24]. However, their method includes expressions that can only be solved by using drastic approximations[25].

Molecular dynamics (MD) simulation is a powerful tool in assessing micelle formation. Micelles size distributions can in principle be obtained using MD by placing a large number of surfactant molecules into a large volume and allowing the system to explore phase space adequately. However this approach is usually computationally too costly and can only be accomplished for surfactants with short hydrophobic tail length or with implicit solvent[26]. Alternatively, free energy calculations could be used to calculate the micelle size distribution by treating micelles of different sizes as different chemical species[27, 28] and using the thermodynamic relationship between the equilibrium constant and species free energies. Yoshii et al. [28] applied thermodynamic integrations to calculate the free energy of adding one sodium dodecyl sulfate (SDS) surfactant to micelles of different sizes, from which they determined the most probable aggregation number of SDS to be 57 near the CMC, agreeing nicely with the experimental value. In our study, based on this chemical species model, we will determine the size distribution of HEUR flower-like micelles through free energies obtained using umbrella sampling. Serero et al. [18] concluded from light scattering experiments that "star-like micelles" formed by singly end-capped (or diblock) copolymers have the same size distribution as the flower-like micelles formed by the doubly end-capped telechelic polymers (or triblock copolymers) for telechelics having twice the molecular weight of the single end-capped molecules and the same end-cap group. Thus, we can obtain the micelle size distribution of the flower-like micelles from that of the corresponding star-like micelles. Our group[29] showed earlier that the coarse-grained (CG) MARTINI [30, 31] force field demonstrates high accuracy in obtaining the micelle structure and desorption energy of the nonionic surfactant C12E5. Therefore, because of its efficiency, the MARTINI force field is applied in the current study to obtain the micelle size distributions.

MD simulations at the CG level are proficient for obtaining the free energy information, while atomistic resolution simulations are more competent for studying the

finer details of the structures such as the interaction with the surrounding molecules, including the solvent, or cosolutes[32]. Thus, we also carry out all atom (AA) simulations of HEUR flower-like micelles of various sizes, which reveal the interactions of HEUR micelle with water molecules, including the average life time that a water molecule hydrates a HEUR micelle.

4.3 Computational models and simulation methods

4.3.1 CHARMM and MARTINI force fields

The GROMACS 4.5.5 simulation engine[33] was used in the current study. Atomistic simulations were carried out with CHARMM version C35r developed by Lee *et al.* [34]. This version of CHARMM contains empirical force field parameters for linear and cyclic ethers that are consistent with the CHARMM framework. In the C35r version of the forcefield, the oxygen partial charges were adjusted to reproduce linear ether liquid properties as well as their interactions with water and solvation energies, and the Lennard-Jones (LJ) parameters were chosen to reproduce the target condensed-phase properties of cyclic ethers. Lee et al. showed that the C35r version yielded a persistence length of 0.37 nm for PEG (polyethylene glycol) and PEO (polyethylene oxide), in agreement with experimentally obtained values; excellent agreement with experiment values for hydrodynamic radii of PEG was also reported[34].

The standard MARTINI force field[30, 35, 31, 36] is used here in all CG simulations using the parameters of the PEO groups developed by Lee et al. [37, 38] within the MARTINI framework. The bonded potentials were developed by comparing the bond, angle and dihedral distributions from the MARTINI force field with results from CHARMM C35r simulations. Nonbonded interactions between CG beads were parametrized using experimental densities of low molecular weight PEO. These pa-

rameters have been applied in several simulations involving the ethylene oxide (EO) group, such as the self-assembly[39] and micellar desorption energies[29] of pentaethylene glycol monododecyl ether (C12E5). In our study, the parameters are adopted from Ref. [39], where each C4 group is represented by a C1 CG bead, and each ethylene oxide group is represented by a SNa CG bead.

4.3.2 Simulation setups

A simplified HEUR molecule that doesn't contain any urethane groups is used in this study. The model HEUR molecule has 45 repeating PEO units which are end capped by a hexadecyl group (C16) on each end. The choice of 45 PEO units represents a compromise between computational cost and fidelity to the commercially available HEUR molecules. The C16 end group is chosen for this study because HEURs with this hydrophobe are widely used both as commercial thickeners and were used in previous experimental studies[6, 40, 41].

Due to the relatively high free energy change associated with the assembly and disassembly of the chosen model HEUR surfactant, the direct simulation of self-assembly of HEUR-C16E45C16 into a micelle is not computationally feasible even with a coarse grained force field. As an alternative, preassembling micelles has been widely used in previous studies for various surfactants[42, 43, 44, 45, 42, 46, 29], and we adopt this method in the investigation of the HEUR micelles in the current study.

To simulate the flower-like structure of the HEUR micelle, one individual HEUR molecule was "bent" at six points to form a loop, then n×0.5 of these molecules were preassembled to form a micelle with the hydrophobic parts facing inward as shown in Figure 4.2 (left image). The centers of mass of the model HEUR molecules were spread evenly on a sphere of radius 3.5 Angstrom using the Saff-Kuijlaars spiral method [47], with the vector connecting from the COM of the sphere to the COM of the HEUR molecule directed perpendicular to the surface of the sphere (see Fig. 4.2,

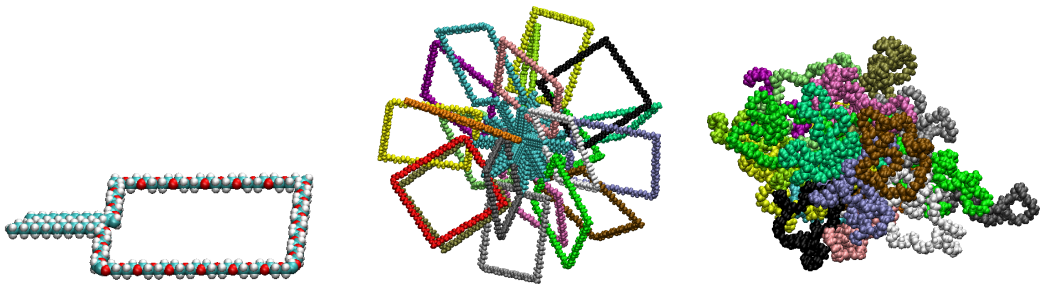

Figure 4.2: Snapshots of the loop created as the initial configuration of a HEUR-$C_{16}E_{45}C_{16}$ molecule (left) and the flower-like micelle with n=40 hydrophobes and 20 HEUR molecules created initially (center) by packing these surfactants together and the configuration after 10 ns of NPT simulation (right). In the left image, the hydrogen atoms are represented by white beads, the carbon atoms by cyan beads, and oxygen atoms by red beads. In the middle and right images, each HEUR molecule is presented by a different color.

middle image). Then the micelle was placed in a cubic box of 17 nm on each side , and energy minimization was conducted, before the simulation box was filled by 157,530 TIP3P water molecules. A 2 ns NPT simulation was then conducted to allow the micelle to further relax, during which time the radius of gyration (R_g) of the micelle was reduced from 4.6 nm to 3.4 nm. To reduce the number of water molecules and accelerate the simulations, the final configuration of the HEUR micelle was then put in a smaller water box of 14 nm on each side with all the overlapping water molecules being deleted.

The final configurations of the micelles were mapped to the coarse-grained scale by replacing each four hydrophobic methylene groups by one C1 bead, and grouping each ethylene glycol group into one SNa bead. The standard MARTINI water beads then were filled into the simulation box followed by energy minimization, pre-production equilibration simulations and production simulations of 1,000 ns duration. The simulation details including the final box size, total number of water molecules, simulation time step and simulation time are listed in Table 4.1. The simulations of star-like

micelles are conducted by removing bonded interactions involving the bond between the 22nd and the 23rd EO groups. Each star-like micelle investigated therefore has equal numbers of $C_{16}E_{22}$ and $C_{16}E_{23}$ molecules. The trajectories of the last 20% of the production runs were used for analysis. Atomistic simulations with hydrophobe aggregation numbers n=10, 20, 40 and 80 were conducted for flower-like micelles, and CG simulations with n=10, 20, 30, 40, 50, 60, 70, 90, 110 were conducted for both flower-like and star-like micelles.

Table 4.1: Details of selected simulations of a single HEUR micelle

	All-atom			Coarse-grained		
n	10	20	40	10	20	40
time step (fs)	2.5	2.5	2.5	10.0	10.0	10.0
simulation time (ns)	100	100	100	1,000	1,000	1,000
box size (nm)	14.1	14.1	13.7	14.1	14.2	13.7
number of water molecules	92,603	91,977	84,352	23,562×4	23,562×4	20,775×4

4.3.3 MD simulation details

For atomistic simulations, production MD simulations were conducted with using V-rescale[48] and the Parrinello-Rahman barostat[49] to regulate temperature and pressure respectively, in an NPT ensemble[50] at 1 bar, 298K, with a pressure time constant of $\tau_p = 0.1$ ps. A cutoff scheme was used for short-range nonbonded interactions (van der Waals, 1.4 nm; real-space Coulomb, 0.9 nm), and long-range electrostatic interactions were computed using the particle mesh Eward (PME) technique (grid spacing of 0.12 nm). Bond lengths were constrained with LINCS, while the water geometry was constrained using SETTLE; energy minimization was performed until the maximum force on any atom was below 100 kJ mol^{-1} nm^{-1}.

4.3.4 Thermodynamics of micelle size distribution

A dilute nonionic micellar solution can be considered as an ideal solution [51, 52, 53, 54]. Micelles of different sizes are treated as different chemical species to describe the free energy of micelles in solution. The chemical potential μ_n of a micelle composed of n surfactants can be written as

$$\mu_n = \mu_n^0 + k_B T ln X_n \tag{4.1}$$

where μ_n^0 and X_n are the standard-state free energy of the n-mer micelle[55] and its mole fraction in solution respectively. The mole fraction of micelles of aggregation number n is defined as $X_n = N_n / \left(\sum_1^\infty N_i + N_w\right)$, where N_i and N_w denote the total number of micelles of size n and number of water molecules respectively. k_B and T are the Bolzmann constant and temperature respectively.

When an association reaction occurs in solution,

$$A_n + A \rightarrow A_{n+1}$$

the free energy change ΔG per micelle of A_{n+1} associated with this process can be written as

$$\begin{aligned}
\Delta G &= \mu_{n+1} - (\mu_n + \mu_1) \\
&= (\mu_{n+1}^0 + k_B T \ln X_{n+1}) - (\mu_n^0 + k_B T \ln X_n) \\
&\quad - (\mu_1^0 + k_B T \ln X_1) \\
&= \Delta\mu_{n+1}^0 + k_B T \ln \frac{X_{n+1}}{X_n X_1}
\end{aligned} \tag{4.2}$$

where

$$\Delta\mu_{n+1}^0 = \mu_{n+1}^0 - (\mu_n^0 + \mu_1^0) \tag{4.3}$$

is the free energy change at infinite dilution. At equilibrium, $\Delta G = 0$, which results in,

$$\frac{X_{n+1}}{X_n} = X_1 \exp\big(-\frac{\Delta\mu^0_{n+1}}{k_B T}\big) \tag{4.4}$$

and

$$X_n = X_1^n \exp\left(-\frac{1}{k_B T}\sum_{j=2}^{n}\Delta\mu_j^0\right) \tag{4.5}$$

Thus, the size distribution of micelles of the solution can be calculated from Equation 4.5 if the values of $\Delta\mu_j^0$ are known. These can be obtained by calculating the free energy change associated with "pulling" a surfactant molecule from its equilibrated location in a micelle of size j into the solution using umbrella sampling, removing the entropy of mixing of the surfactant with the solvent as described below. Here, for future reference, we define the CMC as the surfactant concentration at which half of the surfactants are isolated molecules and the other half are in aggregated form. That is, at the CMC, the following condition holds:

$$X_1 = \sum_{i=2}^{\infty} iX_i \tag{4.6}$$

We now define C_t as the total concentration of surfactant (in units of mol/L). To convert the mole fractions to the molar concentrations, we consider that in dilute solutions, the molar concentration of water is 55.5 mol/L.

For micelles of aggregation number n whose mole fraction is X_n, the molar concentration is then $C_n = X_n \times 55.5$ mol/L, and the total molar concentration of surfactant can be written as:

$$C_t = \sum_{i=1}^{\infty} iC_i \tag{4.7}$$

4.3.5 Umbrella sampling

Umbrella sampling[56] was used to find the free energy profile for transferring a single C16 group from an aggregate to bulk water. The configuration at the end of an NPT trajectory was used as the initial structure for a "pulling" simulation, to generate the initial configurations for umbrella sampling within each window, defined below. The center of mass (COM) distance R between each C16 group and the rest of the micelle (excluding the molecule that contains the above-mentioned C16 group) was calculated, and the C16 group with the shortest COM distance from the rest of the micelle was selected and then pulled relatively rapidly away from the micelle over a 10 ns timescale using a spring constant of 1000 $\mathrm{kJ^{-1}nm^{-2}}$ and a pulling rate of 0.007 nm $\mathrm{ps^{-1}}$. This pulling was carried out to create a set of starting configurations, one for each "window" to be used in the weighted histogram free energy calculations described shortly. The pulling rate used in this stage, although relatively fast, was nevertheless slow enough to allow the average position of the surfactant to keep up with the position of the minimum in the pulling potential. The final center of mass distance between the pulled C16 group and the rest of the micelle was about 7 nm. To generate the starting configurations for the umbrella-sampling windows to be used in subsequent parallel simultaneous runs on a multi-core computer, snapshots were taken from this "fast" pulling trajectory with uniform spacing of windows.

A total of 60 windows were used with a spacing of 0.1 nm COM separation between them. In each window, a 100 ns MD simulation was performed for umbrella sampling. A harmonic force with a force constant of 1200 $kJmol^{-1}nm^{-2}$ was applied for each umbrella-sampling window. To generate the potentials of mean force (PMFs), the weighed histogram analysis method (WHAM)[57] was used, implemented by the Gromacs facility g_wham[58].

The resulting micelle PMF curves were adjusted by subtracting the phase volume contribution (or entropy of mixing) implicit in using a radial reaction coordinate R

that allows angular variations, to construct a one-dimensional PMF. That is, along the reaction coordinate R, there is an increase in accessible phase space due to the increased geometric volume, leaving to a continually decreasing PMF at large pulling distances. The free energy can be corrected for this by [29]

$$PMF_c = PMF_{US} + 2K_BTlog(R) \tag{4.8}$$

where PMF_c is the corrected PMF curve reported in this study and PMF_{US} is the PMF calculated from umbrella sampling simulations. (The units of distance in the correction term appear as an additive constant that is scaled out when the PMF is zeroed at a reference value of the reaction coordinate.) $-\Delta\mu_n$ is the difference between the maximum and the minimum values of PMF_c for a micelle with aggregation number n. Once corrected for the phase volume, the PMF becomes flat at large pulling distances [29], showing that the contribution due to entropy of mixing of the surfactant molecule with the solvent has been successfully removed. (The entropy of mixing is already accounted for in Eq. 1, and equations following it, by the logarithm of concentration and should therefore not be included in the difference in standard state chemical potential in Eq. 3, nor in the PMF used to calculate it.)

From the simulation results, we calculated two PMFs, one using the first half of the umbrella simulation, and the other from the second half. The average of the two PMFs and the standard deviation are reported. All configurations were visualized with VMD 1.9.1[59, 60].

4.4 Results and Discussion

4.4.1 Validation of the CG force filed

As explained above, 1 μs long MD simulations were performed for HEUR micelle of different micelle sizes. Our group [29] has demonstrated that the MARTINI

force field gives accurate structural properties and desorption energies for micelles of C12E5, which is chemically similar to the HEUR molecule studied here. To further demonstrate the accuracy of the CG parameters for simulating the model HEUR micelle, we show in Figure 4.3 that the spatial distribution of the head/tail groups obtained from CG simulations agree with those from atomistic simulations,for aggregation numbers 20 and 40, although the head groups in the CG simulations show a slightly narrower distributions than in the atomistic simulations. We also show in Table 4.2 that the radii of gyration (R_g) of the flower-like micelles of different aggregation numbers from all-atom (AA) and coarse-grained (CG) simulations are within one standard deviation of each other, indicating the accuracy of the CG force field in predicting the structural properties of the micelles.

Table 4.2: Comparison of radii of gyration of HEUR flower-like micelles calculated from all-atom and coarse-grained simulations. The "errors" given are standard deviations.

R_g (nm)	n=10	n=20	n=40
all-atom	1.67±0.08	1.97±0.04	2.47±0.03
coarse-grained	1.62±0.08	1.95±0.07	2.38±0.05

4.4.2 CG simulations

4.4.2.1 Sizes and shapes of flower-like and star-like micelles

Next, we study the effect of aggregation number on micelle size and shape by simulating HEUR flower-like micelles of different aggregation numbers and their corresponding star-like micelles that have the same hydrophobe aggregation numbers. Figure 4.4 (a) shows that the radii of gyration of star-like micelles are about 10% larger than those of the corresponding flow-like micelles, while the radii of gyration of the hydrophobic cores are indistinguishable for the same aggregation number. Star-like micelles are slightly larger than their corresponding flower-like micelles because

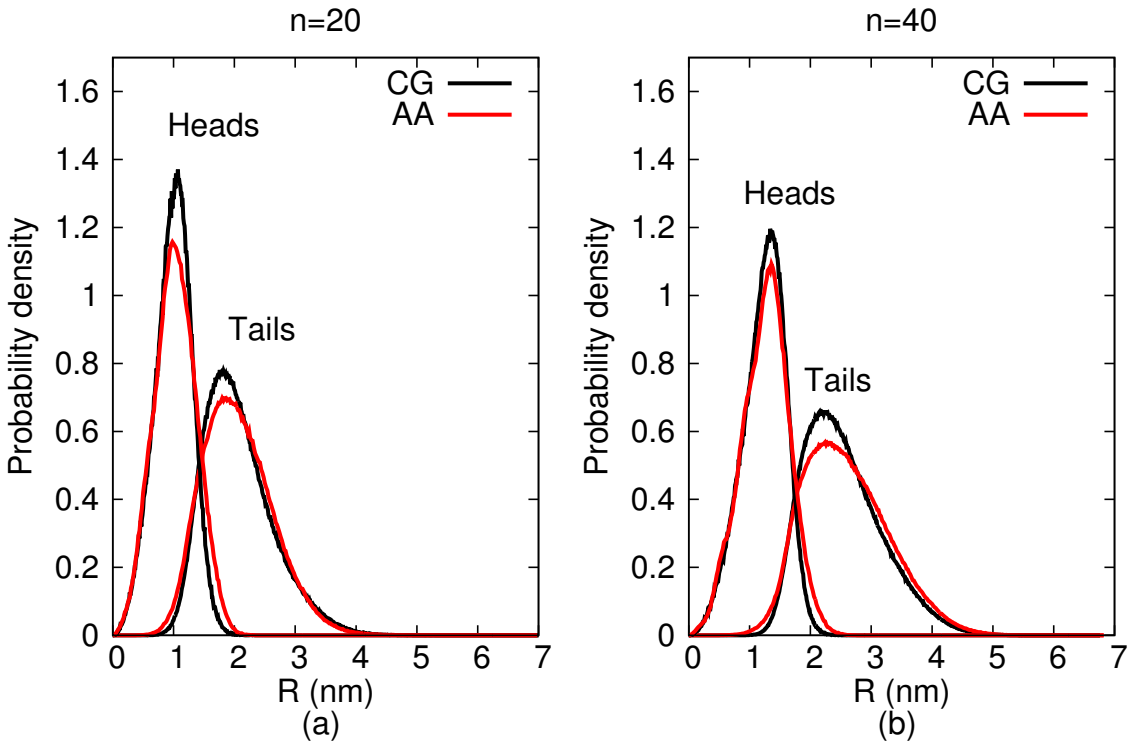

Figure 4.3: Probability density distributions of the distances of the head or tail group center of mass from the center of mass of the HEUR flower-like micelle for hydrophobe aggregation numbers of 20 and 40 from all-atom (AA) and coarse-grained (CG) simulations.

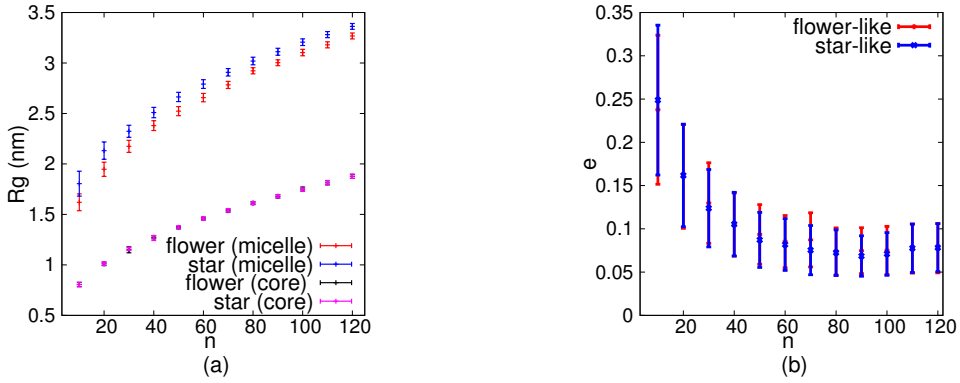

Figure 4.4: Radii of gyration R_g (a) and eccentricities e (b) of flower-like and star-like micelles as functions of hydrophobe aggregation number n. Error bars represent standard deviations.

the EO groups in the star-like micelles are less constrained than those in the flower-like micelles. As expected from the spherical geometry, the micelle size (R_g) increases faster with aggregation number for the lower aggregation numbers. The micelle shape is characterized by eccentricity e, defined as $e = 1 - \frac{I_3}{I_{avg}}$, where $I_{avg} = \frac{I_1+I_2+I_3}{3}$ and I_1, I_2 and I_3 are, respectively, averages of the largest, second largest, and the smallest values of the instantaneous principal values of the moment of inertia tensor. Figure 4.4 (b) shows that both flower-like and star-like micelles become more spherical (smaller value of e) as the aggregation number increases, and for the same aggregation number, star-like and flower-like micelles have similar eccentricities. Figure 4.5 shows that for most flower-like and star-like micelles in the range of aggregation number investigated, I_3/I_2 is larger I_2/I_1, indicating a prolate shape.

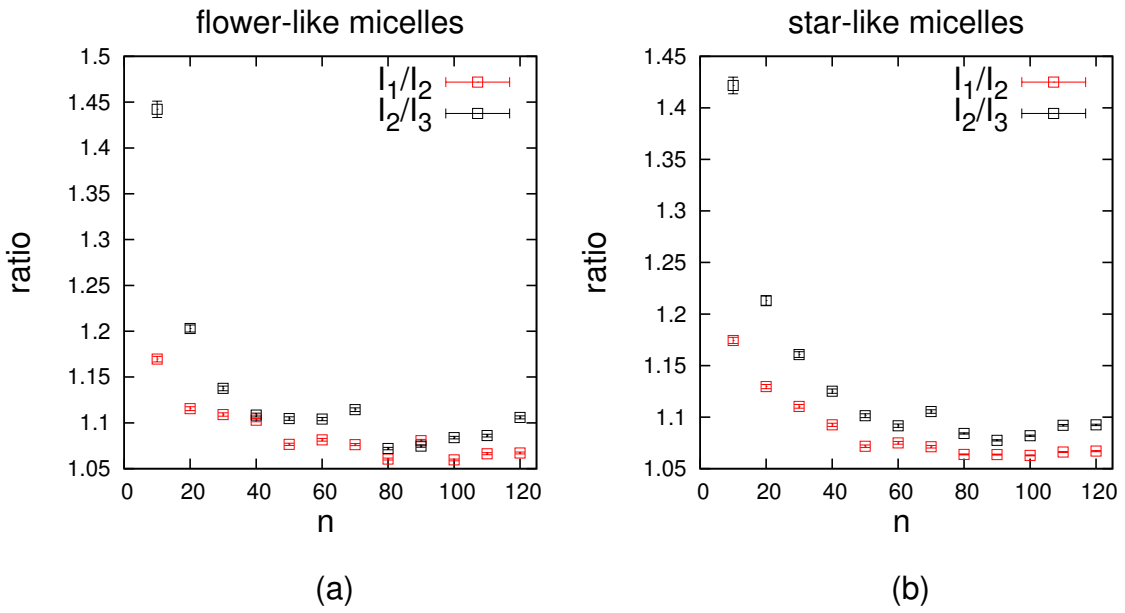

Figure 4.5: Comparisons of I_1/I_2 and I_2/I_3 for (a) flower-like micelles, and (b) star-like micelles; here error bars represent standard errors.

4.4.2.2 Potentials of mean force for flower-like and star-like micelles

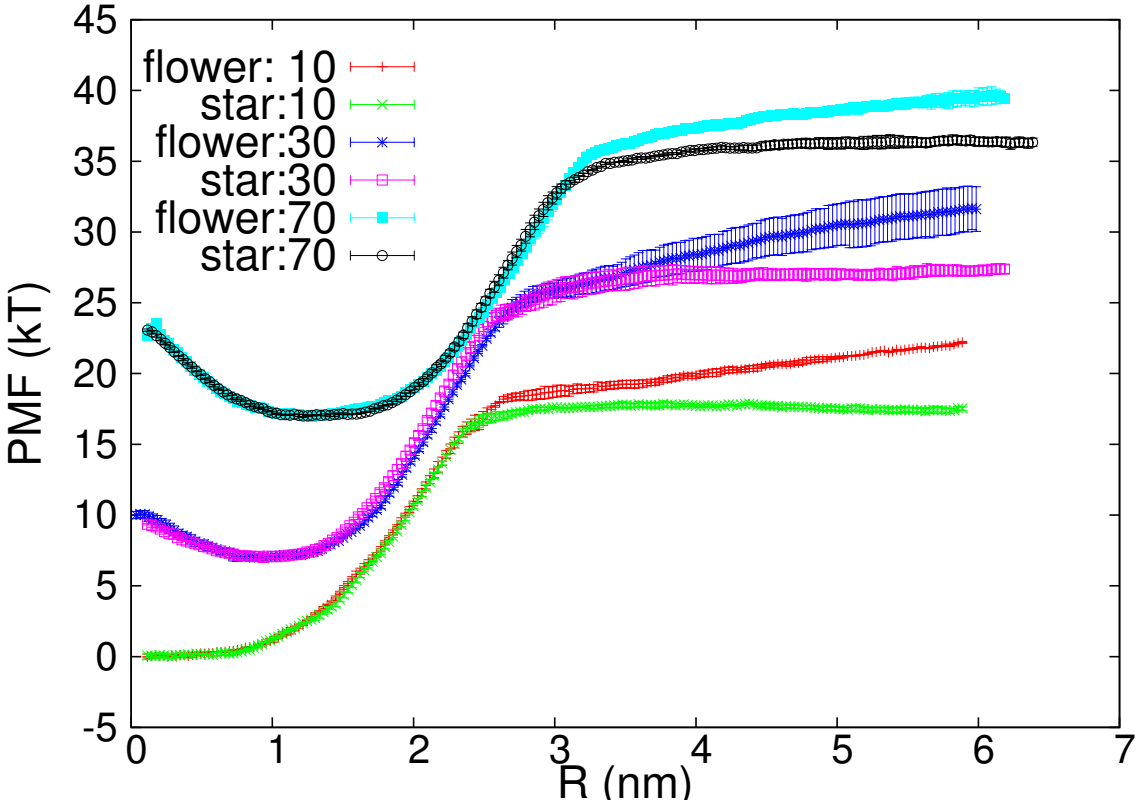

Figure 4.6: Potentials of mean force as a function of distance of C16 hydrophobe center of mass R from micelle center of mass of flower-like and star-like micelles. The numbers given in the legend are the hydrophobe aggregation numbers.

Figure 4.6 demonstrates that the PMFs for pulling a C16 group from a flower-like micelle into water is identical to that for the corresponding star-like micelle in the small R region. However, for R larger than the turning point in the PMF (which occurs at R around 2.5 to 3.5 nm), the PMFs of the star-like micelles level out while those of the flower-like micelles continue to increase. This increase is presumably due to the stretching of the EO segments that join the exiting hydrophobe to the hydrophobe remain in the flower-like micelle. To estimate the size distribution of the flower-like micelles, we apply the method discussed in Section 4.3.4 earlier using the

PMFs of the star-like micelles, to avoid the contributions of EO chain stretching. The hydrophobe aggregation number distribution thereby determined should also apply to flower-like micelles, since the two distributions are believed to be nearly the same for the flower-like and star-like micelles.

4.4.2.3 Micelle size distribution for star-like micelles

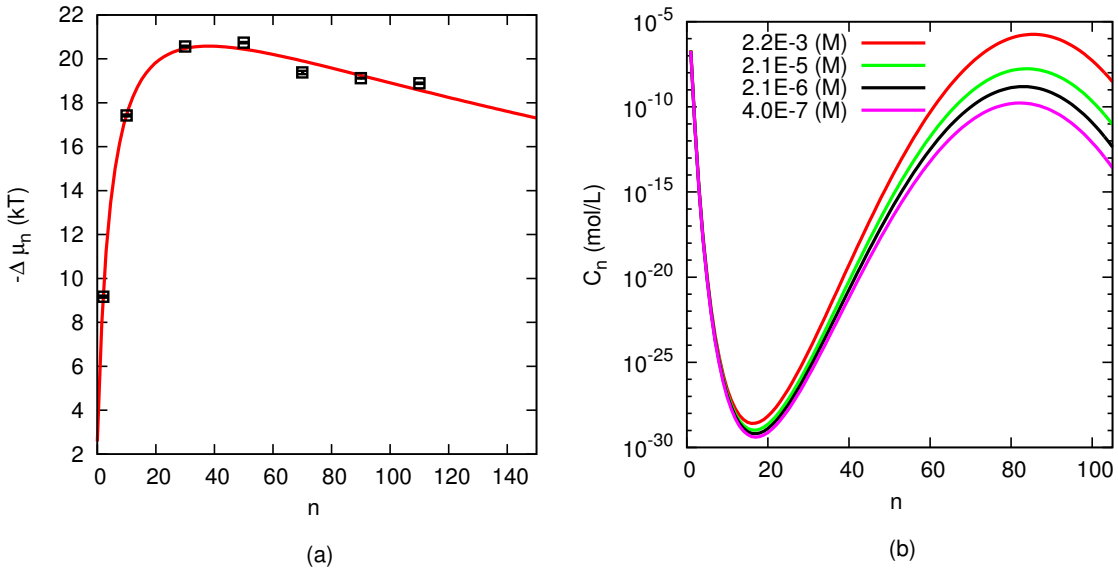

Figure 4.7: (a), -$\Delta\mu_n$ as a function of aggregation number for C16 groups in star-like micelles, where dots are from umbrella sampling, and the line is a fit using $f(n) = a + b \times n/(1 + c \times n + d \times n^2)$, and fitting parameters are a=2.58, b=4.67, c=0.21, d=6.91 $\times$ 10^{-4}; (b)computed hydrophobe aggregation distributions from Eq. 4.5 for star-like micelles at different total concentrations of surfactant (in mol/L) , given in the legend.

Figure 4.7 (a) shows the dependence of $-\Delta\mu_n$ on aggregation number for star-like micelles. As the aggregation number increases, the free energy for translating

Table 4.3: Dependence of monomer concentration (C_1) and peak aggregation number (N_p) in the micelle size distribution on total concentration of surfactant (C_t)

C_t (M)	C_1 (M)	N_p
3.8×10^{-7}	1.9×10^{-7}	82
2.0×10^{-6}	1.9×10^{-7}	83
2.0×10^{-5}	2.0×10^{-7}	84
2.1×10^{-3}	2.1×10^{-7}	85

a surfactant from its equilibrium position inside the micelle to water increases at low aggregation numbers, $-\Delta\mu_n$, reaches a maximum at about n=50, and then decreases slowly as n further increases. Applying Equation 4.5, one can use these data, interpolated using an empirical function given in the caption to Fig. 4.7, to obtain the micelle size distribution at different total surfactant concentrations, as shown in Fig. 4.7 (b) and Table 4.3. As the total concentration increases from 4×10^{-7} M (which is around the CMC) to 2×10^{-3} M (a 5000-fold increase), the monomer concentration is nearly unchanged at about 2×10^{-7} M, demonstrating that the CMC of C16E22/C12E23 micelle is about 2×10^{-7} M.

For all total surfactant concentrations considered in Fig. 4.7(b), we see the expected shape of the distribution[21], with a minimum in the region of small aggregates and a maximum in the region of full-size micelles[61]. The most probable micelle size is found to be about 80 in the proximity of the CMC, and as the total concentration of the surfactants increases, this shifts slightly to around 85 at the total concentration at about 10^4 times the CMC. We note here that since the largest micelle for which we obtained a PMF has an aggregation number of 110, we cannot be sure that there are not much larger cylindrical micelles formed at high surfactant concentrations.

Becher [62, 63] showed that for polyoxyethylene derivatives of lauryl alcohol (EO = 8 to 23) and nonylphenol (EO = 10 to 30) the peak position of the distribution N_p

was related to the polyoxyethylene chain by

$$N_p = a/R - b, \tag{4.9}$$

where R is the average ethylene oxide mole ratio (for surfactant C_iEO_j, $R = \frac{j}{i+j}$) and a and b are constants. Eini *et al.* [62] applied light scattering and hydrodynamic measurements and determined the aggregation numbers of C_{16} polyoxyethylene non-ionic surfactants of the form $C_{16}EO_j$, which we present in Figure 4.8 along with the fitting to Eq. 4.9, from which the most probable aggregation number for the micellar solutions investigated here (for which j = 22-23) is calculated to be 76, which is very similar to the peaks positions obtained from our simulations. The calculated distribution is rather sharp with a half width of about 10. This indicates that the size of micelles may be considered to be nearly monodisperse.

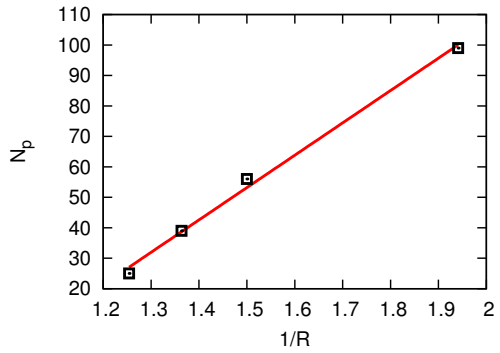

Figure 4.8: Dependence of micelle size on inverse ethylene oxide mole ratio 1/R for $C_{16}EO_j$ surfactants, where a and b are constants (a= 106.227, b= -106.151) Data are from Ref. [63]

4.4.2.4 Mean first passage time for star-like micelles

The mean first-passage times for a C16 group to escape from the micelle were also evaluated from the PMFs. The mean first-passage time is calculated from[64]

$$\tau(x, x_f) = \int_{x}^{x_f} dx' \frac{exp[W(x')/kT]}{D(x')} \times \int_{x_0}^{x'} dx'' exp[-W(x'')/kT] \tag{4.10}$$

Here, $\tau(x, x_f)$ is the mean time for a C16 group to first travel from a position x (which is close to the COM of the micelle) to position x_f, the final state. We take position x to be the same as the radial coordinate R. x_0 corresponds to a reflecting boundary for the Smoluchowski equation, and in this study its value is set to be the smallest reaction coordinate (which corresponds to a high free energy and thus the results are insensitive to its value). $D(x')$ corresponds to the position-dependent diffusion coefficient. In this study, the diffusion coefficient of the C16 group is considered to be constant equal to $8.5 \times 10^{-4} nm^2/ps$ [65], while W(x) represents the free energy profile (or PMF) along the reaction coordinate. Fig. 4.9 shows that the mean first-

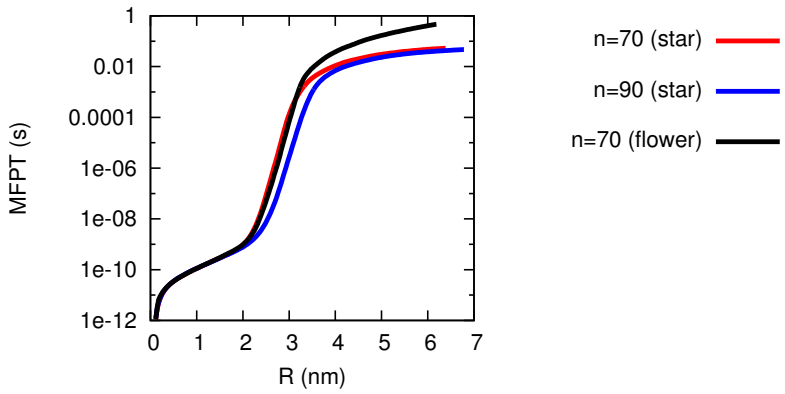

Figure 4.9: Mean first-passage time profile for a C16 group to transfer out of micelles of various aggregation numbers n

passage time (MFPT) profile for a C16 to escape from near the COM of a flower-like micelle to a distance 6 nm from the aggregate, for aggregation numbers close to the

most probable micelle size is around 0.05 - 0.1 s, which roughly agrees with the result of 0.1 s obtained experimentally by Annable et al. in 1993 [66]. The MFPT of a flower-like micelle of aggregation number 70 is identical to that of a star-like micelle of the same size up to R= 3nm, while at R larger than 3 nm, the MFPT increases much faster than for the corresponding star-like micelle, due to the stretching of the short polyethyl oxide chain in the HEUR molecule.

4.4.3 Atomistic MD simulations

4.4.3.1 Solvent accessible area (SASA)

Table 4.4 lists the solvent accessible surface areas (SASA) per surfactant for the model HEUR flower-like micelles with hydrophobe aggregation numbers of 10, 20, 40 and 80 obtained from atomistic simulations. The SASA is the surface area of a micelle that is accessible to a solvent molecule determined by rolling a probe of radius 0.14 nm over the surface of the micelle. The SASA per micelle grows linearly with aggregation number, which is the same dependence also observed in CHAPS ((3-[(3- cholamidopropyl)dimethylammonio]-1-propanesulfonate)) micelles[67]. The SASA per HEUR molecule, on the other hand, decreases as n increases, as has been observed in other micellar systems such as 1-hexanoyl-2-hydroxy-snglycero- 3-phosphocholine (HPC)[32] and dodecylphosphocholine (DPC)[68]. The hydrophobic SASA, which is the contribution to the SASA from hydrophobic contacts, suffers a more obvious decrease per surfactant molecule with increasing n than the hydrophilic one. A similar trend has been reported by Yoshii *et al.* [28] who found that the hydrophobic SASA percentage of SDS micelles decreases with increasing aggregation number, and Tileleman *et al.* who reported that when increasing DPC micelle aggregation number from 40 to 65, the hydrophobic percentage of SASA decreases from 25.9% to 19.7%.

Table 4.4: Solvent accessible surface area (SASA) for HEUR micelles of hydrophobe aggregation numbers 10, 20,40 and 80 using atomistic simulations

	single HEUR	n=10	n=20	n=40	n=80
SASA/surf.(nm^2)	26.5±1.4	21.7±1.0	19.7±0.8	18.6±0.3	17.3±0.3
SASA/mic.(nm^2)	-	108.7±5.1	196.9±7.7	372.6±6.9	690.6±13.4
hydrophobic % of SASA	-	5.8%	4.6%	3.7%	3.3%

4.4.3.2 Hydrogen bond formation and hydration water lifetime

The solubility of PEO is largely due to ability of ethylene glycol oxygens to form hydrogen bonds with water molecules. On average, each EO group forms one hydrogen bond with water in PEO[34]. Consistent with this, in our 2 ns simulation of dimethoxyethane (DME), which is a dimer of PEO, we found that the number of hydrogen bonds formed between a DME oxygen and water is 1.1+/-0.4. To study the

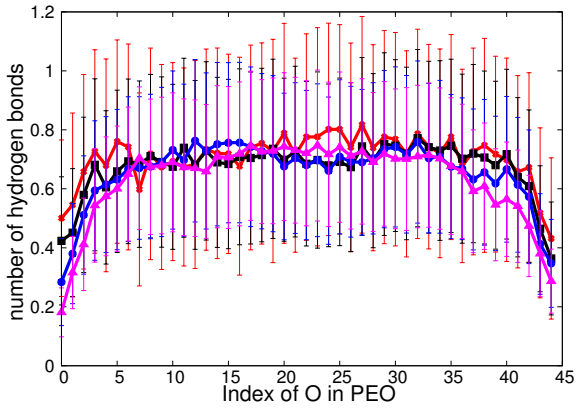

Figure 4.10: Average number of hydrogen bonds formed between each ethylene glycol unit, numbered sequentially along the HEUR, and water. Red lines and error bars represent n=10; black n=20; blue n=40; and purple n=80. The error bars are standard deviations.

effect of aggregation number on hydrogen-bond formation, we calculated the average number of hydrogen bonds formed by each ethylene glycol unit with water for three aggregation numbers. In this study, hydrogen bonds are defined by the requirements that (1) the distance between water oxygen and PEO oxygen must be less than 0.35

nm, and (2) the hydrogen bond angle (formed by the water oxygen, water hydrogen and polymer oxygen) should be greater than 150°[69]. Fig. 4.10 shows the average number and standard deviations of hydrogen bonds formed by each ethylene glycol unit with water molecules for three different aggregation numbers. The number of hydrogen bonds formed is location dependent; the EO unit immediately adjacent to the hydrophobic groups (index =0 or 44) has the lowest average number of hydrogen bonds, around 0.5, and this number gradually increases toward the middle of the chain to around 0.8, which is slightly lower than for DME. The aggregation number of the HEUR shows no influence on hydrogen bonding.

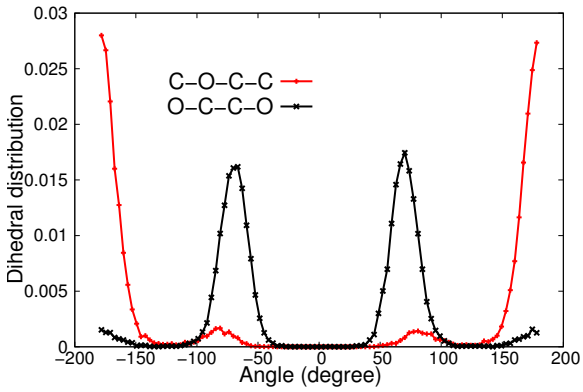

Figure 4.11: Distribution of the O-C-C-O and C-C-O-C dihedral angles in HEUR micelle (n=40)

We find that water enhances the gauche population of the O-C-C-O dihedral, apparently because gauche conformers present total dipole moments which strengthen the polymer-solvent interactions[70]. In Fig. 4.11, the distributions of the two dihedrals O-C-C-O and C-O-C-C of PEO groups in water are reported only for $n = 40$, since no significant variations were found among different aggregation numbers. As shown in Figure 4.11, the O-C-C-O dihedral angles predominantly take gauche configurations while the C-C-O-C dihedral angles are mostly trans, which is consistent with previous NMR[71, 70], and IR[72] experiments as well as simulation studies[73, 34] of PEO.

To further investigate the interactions of the PEO groups and water molecules, the residence time over which water molecules remain in proximity to the PEG oxygen was also evaluated for all three aggregation numbers. If the distance between the water oxygen and PEG oxygen is less than 0.35 nm, the water molecule is considered "near" enough to the PEG to be considered a water of hydration [74]. To evaluate the residence time of this "hydration" water, additional simulations of the micelles were carried out, with a time step set at 2.5 fs, total simulation time at 2 ns, and with the trajectory saved every 1 ps, the last 1 ns of which was used for analysis. For comparison, the residence time of hydration water near dimethoxyehane (DME) was also calculated by simulating one DME molecule with 886 water molecules in a cubic simulation box of 2.98 nm.

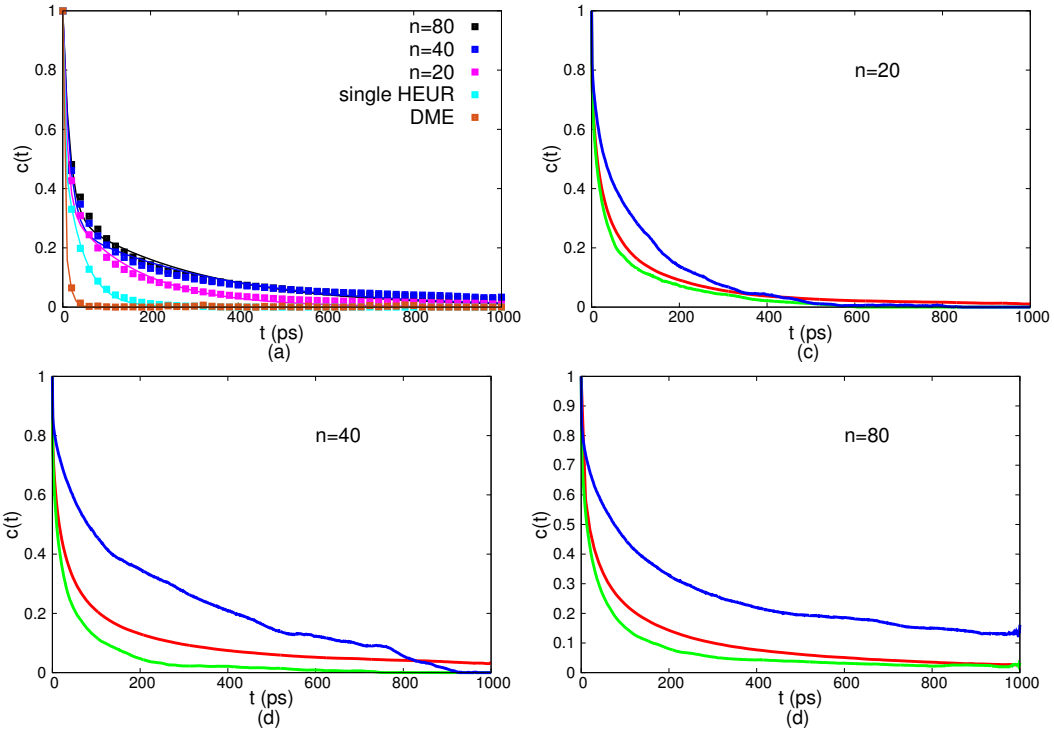

Figure 4.12: (a): Residence time distribution c(t) of hydration water in the vicinity of the EO groups in DME, near a single HEUR molecule, and near HEUR micelles of various aggregation numbers. (b)-(d): the same for hydration water of all EO groups (in red), of middle EO groups (in green) and of end EO groups (in blue)

Table 4.5: Slow and fast time constants and corresponding weights for residence times of hydration water for PEO groups in DME, in a single HEUR molecule, and in HEUR micelles of various aggregation numbers

	w_1	τ_1 (ps)	w_2	τ_2 (ps)
DME	0.43	10.0	0.57	1.3
Single HEUR	0.53	43.6	0.47	2.7
n=10	0.42	90.6	0.58	5.9
n=20	0.34	161.9	0.66	9.5
n=40	0.28	332.0	0.72	15.1
n=80	0.31	306.4	0.69	15.9
n=80 (end EO)	0.42	734.4	0.58	39.4
n=80 (middle EO)	0.24	228.3	0.76	14.0

We define the residence distribution c(t) as the ratio of the number of water molecules remaining near the EO groups of a HEUR micelle, a HEUR molecule, or a DME molecule continuously over a time period 't' to the number of water molecules initially in proximity to the EO groups at time zero (t = 0). c(t) is often fitted by a single exponential, but this fit is less than satisfactory in our system, and a double exponential resulted in a more accurate fit[75]:

$$c(\tau) = w_1 \; exp(-k_1\tau) + w_2 \; exp(-k_2\tau) \tag{4.11}$$

where k_1, w_1 and k_2, w_2 (w_2=1-w_1) are the rate constants and the weights for the slow and fast relaxing components respectively. The long and the short residence times are then defined as $\tau_1 = 1/k_1$ and $\tau_2 = 1/k_2$. c(t) for the hydration waters of all PEO groups in HEUR micelles of different n (including a single HEUR molecule) and of DME are plotted in Fig. 4.12a, and the fitting parameters are listed in Table 4.5. The long residence time τ_1 ($1/k_1$) of DME (10.0 ps) is not too much greater than the residence time of hydrogen bonds of water ($\approx$ 3ps)[74]. The τ_1 of a single HEUR molecule in water is found to be 43.6 ns in this study, roughly agreeing with previous simulation results [76, 77] and experimental studies of the residence time for short PEO chains in water. As n increases, the water decay slows down as shown

in Fig.4.12a and Table 4.5. Borodin et al. [77] reported that hydrogen bond lifetimes increase with increasing PEO concentration, and they attributed the slowing of water dynamics in condensed PEO/water solutions to PEO-water interactions being moderated by the formation of water clusters at high polymer concentrations.

We also calculated c(t) for the EO group immediately adjacent to the C16 groups namely, EO_0 and EO_{44}, and that of the EO group in the middle of the HEUR chain, namely EO_{22}. (The EO groups are numbered sequentially starting immediately adjacent to the first hydrophobe, which is "EO_0") Fig. 4.12 b-d compares c(t) for the end and middle EO groups and c(t) averaged for all EO groups for HEUR micelles of various sizes. The EO groups located farthest from the core of the HEUR micelle (EO_{22}) have shorter residence times than those located close to the hydrophobic core, indicting that the hydration waters trapped close to the hydrophobic region of the micelle have more difficulty escaping. This location-dependent water residence time was also reported in previous studies of micelles that contain PEO groups[74]. The longest residence times reported here for water near EO groups are 70 times longer than for a PEO dimer, dimethoxyethane.

4.5 Conclusions

We demonstrated a method to obtain the micelle size distribution of flower-like micelles formed by alkane-polyethylene oxide-alkane ($C_iE_jC_i$) type block copolymers based on a mass action model that treats each micelle size as a different species. We applied coarse-grained simulations and umbrella sampling to calculate the free energy change (or PMF) for transferring a hydrophobic group from micelles of various aggregation numbers to the surrounding water, and constructed the micelle aggregation number distribution at different total surfactant concentrations. The critical micelle concentration of $C_{16}E_{45}C_{16}$ was found to be about $2 \times 10^{-7} mol/L$, and the micelle size distribution to be sharply peaked at a most probable size of 80-85, consistent

with previous experimental results. Using atomistic simulations, we found that hydrogen bonds are formed between the EO groups in HEUR micelles and water, that the hydration waters decay faster for EO groups in smaller micelles than in bigger ones, and that the hydration waters of EO groups that are in closer proximity to the hydrophobes have significantly longer (by a factor of three) decay times than those of EO groups in the periphery of the micelles. The longest water residence times reported here for EO groups in HEUR micelles are around 70 times higher than for a dilute dimer of PEO, dimethoxyethane (DME). The use of atomistic and coarse-grained force fields, combined with computation of the potential of mean force, is found to give both structure and dynamical information about micelles over a broad range of time scales ranging from picoseconds to many milliseconds, which is the residence time of a HEUR hydrophobe in the micelle.

Bibliography

[1] A. Rösler, G. W. Vandermeulen, and H.-A. Klok, "Advanced drug delivery devices via self-assembly of amphiphilic block copolymers," *Adv. Drug Deliv. Rev.*, vol. 64, pp. 270–279, 2012.

[2] K. M. Ho, W. Y. Li, C. H. Wong, and P. Li, "Amphiphilic polymeric particles with core–shell nanostructures: emulsion-based syntheses and potential applications," *Colloid Polym. Sci.*, vol. 288, no. 16-17, pp. 1503–1523, 2010.

[3] Z. Iatridi, G. Mattheolabakis, K. Avgoustakis, and C. Tsitsilianis, "Self-assembly and drug delivery studies of ph/thermo-sensitive polyampholytic (a-co-b)-b-c-b-(a-co-b) segmented terpolymers," *Soft Matter*, vol. 7, no. 23, pp. 11160–11168, 2011.

[4] K. Tam, R. Jenkins, M. Winnik, and D. Bassett, "A structural model of hy-

drophobically modified urethane-ethoxylate (heur) associative polymers in shear flows," *Macromolecules*, vol. 31, no. 13, pp. 4149–4159, 1998.

[5] K. Tam, W. Ng, and R. Jenkins, "Further studies on the rheological properties of hydrophobically modified polyelectrolyte systems: effect of varying degree of ethoxylation," *Polym. Int.*, vol. 56, no. 4, pp. 569–575, 2007.

[6] A. Tripathi, K. C. Tam, and G. H. McKinley, "Rheology and dynamics of associative polymers in shear and extension: theory and experiments," *Macromolecules*, vol. 39, no. 5, pp. 1981–1999, 2006.

[7] B. Grassl, L. Billon, O. Borisov, and J. François, "Poly (ethylene oxide)-and poly (acrylamide)-based water-soluble associative polymers: synthesis, characterisation, properties in solution," *Polym. Int.*, vol. 55, no. 10, pp. 1169–1176, 2006.

[8] X.-X. Meng and W. B. Russel, "Structure and size of spherical micelles of telechelic polymers," *Macromolecules*, vol. 38, no. 2, pp. 593–600, 2005.

[9] P. Alexandridis and B. Lindman, *Amphiphilic Block Copolymers: Self-Assembly and Applications*. Elsevier, 2000.

[10] A. Kelarakis, Z. Yang, E. Pousia, S. K. Nixon, C. Price, C. Booth, I. W. Hamley, V. Castelletto, and J. Fundin, "Association properties of diblock copolymers of propylene oxide and ethylene oxide in aqueous solution. the effect of p and e block lengths," *Langmuir*, vol. 17, no. 26, pp. 8085–8091, 2001.

[11] F. Renou, T. Nicolai, E. Nicol, and L. Benyahia, "Structure and viscoelasticity of mixed micelles formed by poly (ethylene oxide) end capped with alkyl groups of different length," *Langmuir*, vol. 25, no. 1, pp. 515–521, 2008.

[12] O. Vorobyova, A. Yekta, M. A. Winnik, and W. Lau, "Fluorescent probe studies of the association in an aqueous solution of a hydrophobically modified poly(ethylene oxide)," *Macromolecules*, vol. 31, no. 25, pp. 8998–9007, 1998.

[13] P. T. Elliott, L.-l. Xing, W. H. Wetzel, and J. E. Glass, "Influence of terminal hydrophobe branching on the aqueous solution behavior of model hydrophobically modified ethoxylated urethane associative thickeners," *Macromolecules*, vol. 36, no. 22, pp. 8449–8460, 2003.

[14] M. Daoud and J. Cotton, "Star shaped polymers: a model for the conformation and its concentration dependence," *Eur. Phys. J.*, vol. 43, no. 3, pp. 531–538, 1982.

[15] C. Chassenieux, T. Nicolai, and D. Durand, "Association of hydrophobically end-capped poly (ethylene oxide)," *Macromolecules*, vol. 30, no. 17, pp. 4952–4958, 1997.

[16] C. Gourier, E. Beaudoin, M. Duval, D. Sarazin, S. Maitre, and J. François, "A light scattering study of the association of hydrophobically α-and α, ω-end-capped poly (ethylene oxide) in water," *J. Colloid Interface Sci.*, vol. 230, no. 1, pp. 41–52, 2000.

[17] E. Beaudoin, O. Borisov, A. Lapp, L. Billon, R. C. Hiorns, and J. François, "Neutron scattering of hydrophobically modified poly (ethylene oxide) in aqueous solutions," *Macromolecules*, vol. 35, no. 19, pp. 7436–7447, 2002.

[18] Y. Serero, R. Aznar, G. Porte, J.-F. Berret, D. Calvet, A. Collet, and M. Viguier, "Associating polymers: from "flowers" to transient networks," *Phys. Rev. Lett.*, vol. 81, no. 25, p. 5584, 1998.

[19] Q. Pham, W. Russel, J. Thibeault, and W. Lau, "Micellar solutions of associa-

tive triblock copolymers: Entropic attraction and gas-liquid transition," *Macromolecules*, vol. 32, no. 9, pp. 2996–3005, 1999.

[20] O. Vorobyova, W. Lau, and M. A. Winnik, "Aggregation number determination in aqueous solutions of a hydrophobically modified poly (ethylene oxide) by fluorescence probe techniques," *Langmuir*, vol. 17, no. 5, pp. 1357–1366, 2001.

[21] C. Hoeve and G. Benson, "On the statistical mechanical theory of micelle formation in detergent solutions," *J. Phys. Chem.*, vol. 61, no. 9, pp. 1149–1158, 1957.

[22] D. C. Poland and H. A. Scheraga, "Hydrophobic bonding and micelle stability1," *J. Phys. Chem.*, vol. 69, no. 7, pp. 2431–2442, 1965.

[23] D. C. Poland and H. A. Scheraga, "Hydrophobic bonding and micelle stability; the influence of ionic head groups," *J. Colloid Interface Sci.*, vol. 21, no. 3, pp. 273–283, 1966.

[24] L. S. Romsted, *Surfactant Science and Technology: Retrospects and Prospects*. CRC Press, 2014.

[25] A. Jódar-Reyes and F. Leermakers, "Self-consistent field modeling of linear nonionic micelles," *J. Phys. Chem. B*, vol. 110, no. 12, pp. 6300–6311, 2006.

[26] S. Wang and R. G. Larson, "Coarse-grained molecular dynamics simulation of self-assembly and surface adsorption of ionic surfactants using an implicit water model," *Langmuir*, 2015.

[27] P. Christopher and D. W. Oxtoby, "Free energy and size distributions of micelles in solution," *J. Chem. Phys.*, vol. 118, no. 12, pp. 5665–5672, 2003.

[28] N. Yoshii and S. Okazaki, "A molecular dynamics study of structural stability of

spherical sds micelle as a function of its size," *Chem. Phys. Lett.*, vol. 425, no. 1, pp. 58–61, 2006.

[29] F. Yuan, S. Wang, and R. G. Larson, "Potentials of mean force and escape times of surfactants from micelles and hydrophobic surfaces using molecular dynamics simulations," *Langmuir*, 2015.

[30] S. J. Marrink, H. J. Risselada, S. Yefimov, D. P. Tieleman, and A. H. de Vries, "The martini force field: coarse grained model for biomolecular simulations," *J. Phys. Chem. B*, vol. 111, no. 27, pp. 7812–7824, 2007.

[31] L. Monticelli, S. K. Kandasamy, X. Periole, R. G. Larson, D. P. Tieleman, and S.-J. Marrink, "The martini coarse-grained force field: extension to proteins," *J. Chem. Theory Comput.*, vol. 4, no. 5, pp. 819–834, 2008.

[32] P. Brocos, P. Mendoza-Espinosa, R. Castillo, J. Mas-Oliva, and Á. Pineiro, "Multiscale molecular dynamics simulations of micelles: coarse-grain for self-assembly and atomic resolution for finer details," *Soft Matter*, vol. 8, no. 34, pp. 9005–9014, 2012.

[33] S. Pronk and E. Lindahl, "Gromacs 4.5: a high-throughput and highly parallel open source molecular simulation toolkit," *Bioinformatics*, vol. 29, no. 7, pp. 845–854, 2013.

[34] H. Lee, R. M. Venable, A. D. MacKerell Jr, and R. W. Pastor, "Molecular dynamics studies of polyethylene oxide and polyethylene glycol: hydrodynamic radius and shape anisotropy," *Biophys. J.*, vol. 95, no. 4, pp. 1590–1599, 2008.

[35] S. J. Marrink, A. H. de Vries, and A. E. Mark, "Coarse grained model for semi-quantitative lipid simulations," *J. Phys. Chem. B*, vol. 108, no. 2, pp. 750–760, 2004.

[36] D. H. de Jong, G. Singh, W. D. Bennett, C. Arnarez, T. A. Wassenaar, L. V. Schafer, X. Periole, D. P. Tieleman, and S. J. Marrink, "Improved parameters for the martini coarse-grained protein force field," *J. Chem. Theory Comput.*, vol. 9, no. 1, pp. 687–697, 2012.

[37] H. Lee, A. H. de Vries, S.-J. Marrink, and R. W. Pastor, "A coarse-grained model for polyethylene oxide and polyethylene glycol: conformation and hydrodynamics," *J. Phys. Chem. B*, vol. 113, no. 40, pp. 13186–13194, 2009.

[38] H. Lee and R. W. Pastor, "Coarse-grained model for pegylated lipids: Effect of pegylation on the size and shape of self-assembled structures," *J. Phys. Chem. B*, vol. 115, no. 24, pp. 7830–7837, 2011.

[39] M. Velinova, D. Sengupta, A. V. Tadjer, and S.-J. Marrink, "Sphere-to-rod transitions of nonionic surfactant micelles in aqueous solution modeled by molecular dynamics simulations," *Langmuir*, vol. 27, no. 23, pp. 14071–14077, 2011.

[40] D. Liao, S. Dai, and K. C. Tam, "Rheological properties of hydrophobic ethoxylated urethane (heur) in the presence of methylated β-cyclodextrin," *Polymer*, vol. 45, no. 25, pp. 8339–8348, 2004.

[41] D. Liao, S. Dai, and K. C. Tam, "Rheological properties of a telechelic associative polymer in the presence of α-and methylated β-cyclodextrins," *J. Phys. Chem. B*, vol. 111, no. 2, pp. 371–378, 2007.

[42] F. Palazzesi, M. Calvaresi, and F. Zerbetto, "A molecular dynamics investigation of structure and dynamics of sds and sdbs micelles," *Soft Matter*, vol. 7, no. 19, pp. 9148–9156, 2011.

[43] A. V. Sangwai and R. Sureshkumar, "Coarse-grained molecular dynamics simulations of the sphere to rod transition in surfactant micelles," *Langmuir*, vol. 27, no. 11, pp. 6628–6638, 2011.

[44] X. Tang, K. J. Huston, and R. G. Larson, "Molecular dynamics simulations of structure–property relationships of tween 80 surfactants in water and at interfaces," *J. Phys. Chem. B*, vol. 118, no. 45, pp. 12907–12918, 2014.

[45] X. Tang, P. H. Koenig, and R. G. Larson, "Molecular dynamics simulations of sodium dodecyl sulfate micelles in water the effect of the force field," *J. Phys. Chem. B*, vol. 118, no. 14, pp. 3864–3880, 2014.

[46] X. Jia, J. Chen, B. Wang, W. Liu, and J. Hao, "Molecular dynamics simulation of shape and structure evolution of preassembled cylindrical cetyltrimethylammonium bromide micelles induced by octanol," *Colloids Surf., A*, 2014.

[47] E. B. Saff and A. B. Kuijlaars, "Distributing many points on a sphere," *Math. Intell.*, vol. 19, no. 1, pp. 5–11, 1997.

[48] G. Bussi, D. Donadio, and M. Parrinello, "Canonical sampling through velocity rescaling," *J. Chem. Phys.*, vol. 126, no. 1, p. 014101, 2007.

[49] M. Parrinello and A. Rahman, "Polymorphic transitions in single crystals: A new molecular dynamics method," *J. Appl. Phys.*, vol. 52, p. 7182, 1981.

[50] J. A. Lemkul and D. R. Bevan, "Assessing the stability of alzheimer's amyloid protofibrils using molecular dynamics," *J. Phys. Chem. B*, vol. 114, no. 4, pp. 1652–1660, 2010.

[51] N. Funasaki and S. Hada, "Molar volumes of mixed micelles as a measure of nonideality of mixing of micelles," *J. Phys. Chem.*, vol. 86, no. 13, pp. 2504–2508, 1982.

[52] J. H. Clint, "Micellization of mixed nonionic surface active agents," *J. Chem. Soc. Faraday Trans.*, vol. 71, pp. 1327–1334, 1975.

[53] N. Funasaki and S. Hada, "Surface tension of aqueous solutions of surfactant mixtures. the composition of mixed micelles," *J. Phys. Chem.*, vol. 83, no. 19, pp. 2471–2475, 1979.

[54] S. Paria, "The mixing behavior of n-alkylpyridinium bromide–np-9 mixed surfactant systems," *Colloids Surf., A*, vol. 281, no. 1, pp. 113–118, 2006.

[55] J. N. Israelachvili, *Intermolecular and surface forces: revised third edition*. Academic press, 2011.

[56] G. M. Torrie and J. P. Valleau, "Nonphysical sampling distributions in monte carlo free-energy estimation: Umbrella sampling," *J. Comput. Phys.*, vol. 23, no. 2, pp. 187–199, 1977.

[57] S. Kumar, J. M. Rosenberg, D. Bouzida, R. H. Swendsen, and P. A. Kollman, "The weighted histogram analysis method for free-energy calculations on biomolecules. i. the method," *J. Comput. Chem.*, vol. 13, no. 8, pp. 1011–1021, 1992.

[58] J. S. Hub, B. L. De Groot, and D. Van Der Spoel, "g_wham:a free weighted histogram analysis implementation including robust error and autocorrelation estimates," *J. Chem. Theory Comput.*, vol. 6, no. 12, pp. 3713–3720, 2010.

[59] W. Humphrey, A. Dalke, and K. Schulten, "VMD – Visual Molecular Dynamics," *J. Mol. Graphics.*, vol. 14, pp. 33–38, 1996.

[60] J. Eargle, D. Wright, and Z. Luthey-Schulten, "Multiple Alignment of protein structures and sequences for VMD," *Bioinformatics*, vol. 22, pp. 504–506, Feb 2006.

[61] S. V. Burov, A. A. Vanin, and E. N. Brodskaya, "Principal role of the stepwise aggregation mechanism in ionic surfactant solutions near the critical micelle

concentration. molecular dynamics study," *J. Phys. Chem. B*, vol. 113, no. 31, pp. 10715–10720, 2009.

[62] P. Becher, "Nonionic surface-active compounds iv. micelle formation by polyoxyethylene alkanols and alkyl phenols in aqueous solution," *J. Colloid Interface Sci.*, vol. 16, no. 1, pp. 49–56, 1961.

[63] D. El Eini, B. Barry, and C. Rhodes, "Micellar size, shape, and hydration of long-chain polyoxyethylene nonionic surfactants," *J. Colloid Interface Sci.*, vol. 54, no. 3, pp. 348–351, 1976.

[64] D. J. Beltran-Villegas, R. M. Sehgal, D. Maroudas, D. M. Ford, and M. A. Bevan, "A smoluchowski model of crystallization dynamics of small colloidal clusters," *J. Chem. Phys.*, vol. 135, no. 15, p. 154506, 2011.

[65] W. S. Price and O. Söderman, "Self-diffusion coefficients of some hydrocarbons in water: Measurements and scaling relations," *J. Phys. Chem. A*, vol. 104, no. 24, pp. 5892–5894, 2000.

[66] T. Annable, R. Buscall, R. Ettelaie, and D. Whittlestone, "The rheology of solutions of associating polymers: Comparison of experimental behavior with transient network theory," *J. Rheol.*, vol. 37, no. 4, pp. 695–726, 1993.

[67] F. E. Herrera, A. S. Garay, and D. E. Rodrigues, "Structural properties of chaps micelles, studied by molecular dynamics simulations," *J. Phys. Chem. B*, vol. 118, no. 14, pp. 3912–3921, 2014.

[68] D. Tieleman, D. Van der Spoel, and H. Berendsen, "Molecular dynamics simulations of dodecylphosphocholine micelles at three different aggregate sizes: micellar structure and chain relaxation," *J. Phys. Chem. B*, vol. 104, no. 27, pp. 6380–6388, 2000.

[69] Z. Li, F. Yuan, K. A. Fichthorn, S. T. Milner, and R. G. Larson, "Molecular view of polymer/water interfaces in latex paint," *Macromolecules*, vol. 47, no. 18, pp. 6441–6452, 2014.

[70] Y. Sasanuma and K. Sugita, "The attractive gauche effect of ethylene oxides," *Polym. J.*, vol. 38, no. 9, pp. 983–988, 2006.

[71] Y. Sasanuma, H. Ohta, I. Touma, H. Matoba, Y. Hayashi, and A. Kaito, "Conformational characteristics of poly (ethylene sulfide) and poly (ethylene oxide): Solvent dependence of attractive and repulsive gauche effects," *Macromolecules*, vol. 35, no. 9, pp. 3748–3761, 2002.

[72] J. J. Shephard, P. J. Bremer, and A. J. McQuillan, "Structure and conformation in mixtures of methyl-terminated poly (ethylene oxide) and water. principal component analysis and band fitting of infrared absorptions," *J. Phys. Chem. B*, vol. 113, no. 43, pp. 14229–14238, 2009.

[73] S. Hezaveh, S. Samanta, G. Milano, and D. Roccatano, "Molecular dynamics simulation study of solvent effects on conformation and dynamics of polyethylene oxide and polypropylene oxide chains in water and in common organic solvents," *J. Chem. Phys.*, vol. 136, no. 12, p. 124901, 2012.

[74] H. Kuramochi, Y. Andoh, N. Yoshii, and S. Okazaki, "w," *J. Phys. Chem. B*, vol. 113, no. 46, pp. 15181–15188, 2009.

[75] V. A. Makarov, B. K. Andrews, P. E. Smith, and B. M. Pettitt, "Residence times of water molecules in the hydration sites of myoglobin," *Biophys. J.*, vol. 79, no. 6, pp. 2966–2974, 2000.

[76] K. Tasaki, "Poly (oxyethylene)-water interactions: a molecular dynamics study," *J. Am. Chem. Soc.*, vol. 118, no. 35, pp. 8459–8469, 1996.

[77] O. Borodin, D. Bedrov, and G. D. Smith, "Concentration dependence of water dynamics in poly (ethylene oxide)/water solutions from molecular dynamics simulations," *J. Phys. Chem. B*, vol. 106, no. 20, pp. 5194–5199, 2002.

CHAPTER V

Conclusions

5.1 Summary

In this doctoral work we have applied multi-scale MD simulations to study the waterborne coatings consisting of latex binders, surfactants and HEUR rheology modifiers.

In Chapter II, We utilize the CHARMM atomistic force field to simulate the interface of the latex binder and water. The model latex slab is composed of atactic random copolymers of PMMA and PBA of mole ratio of 1:1. We validated the CHARMM force field parameters by comparing the simulated bulk polymer properties of PMMA and PBA with experiments. The atomistic simulates successfully predicted the PMMA static structure and temperature dependence of surface energy of PBA/vacuum systems. Using these parameters, we built a slab of copolymer of PMMA and PBA, and characterized it by density profile and hydrogen bonds formation. The interactions of the copolymer slab and a commonly used surfactant SDS is characterized using PMFs, the free energy penalty of transferring an SDS molecule from its equilibrated position on the latex surface is found to be about 17kT, indicating a very strong bonding between the latex surface and the SDS surfactant. From the PMF of transferring an SDS to the aqueous solution, we obtained the relationship between the bulk SDS concentration and surface coverage of SDS on latex surface at

low bulk concentrations ($K = \frac{\Gamma}{c_0}$). The maximum coverage of SDS on latex surface is found to be 1.87 $surf./nm^{-2}$. The adsorption isotherm of SDS on latex surface in water is therefore constructed using K in the low concentration region and the maximum coverage in the high concentration region. The dynamics of the interfacial water molecules are found to be affected by the coverage of SDS absorbed on latex surface. The adsorbed SDS molecules slow down the rotational dynamics of interfacial water significantly. The orientational relaxation time (τ_r) is found to increase monotonically as the coverage of SDS increases.

The rheology and the structure of the latex paint depend largely on the relaxation times of hydrophobes escaping from the micelle and from the hydrophobic latex surfaces. In Chapter III, we developed a method to evaluate the mean first-passage times (MFPT) of these escaping processes from PMF and diffusion coefficients calculations. We compare the MFPTs of a hydrophobe escaping from its micelle and from the latex surface for an ionic surfactant (SDS) and a nonionic surfactant (C12E5). For both surfactants, the escaping times from the latex surface are longer than from the micelles, indicating that, at low concentrations of surfactants, the majority of the surfactants resides on the latex surfaces rather than in their aggregate forms, consisting with previous experimental predictions. In this Chapter, we also evaluated two coarse-grained (CG) force fields, MARTINI and SDK, and we find that the two force fields are both accurate in simulating the nonionic surfactant (C12E5), and for ionic surfactant (SDS), the MARTINI force fields doesn't result in accurate PMF because it ignores the long-range electrostatic interactions while the SDK force fields successfully reproduces the PMF curve.

In Chapter IV, we developed a chemical species model that accurately predict the micelle size distribution of HEUR flower-like micelles. In this model, micelle of each size is treated as a different species, the free energy changes of transferring a hydrophobe from a micelle of various sizes are used to obtain the size distribution

and critical micelle concentration. The free energies changes are calculated using the MARTINI force field to achieve high simulation efficiency, since we have demonstrated its accuracy in simulating nonionic surfactants. The most probable hydrophobe aggregation number of C16E45C16 HEUR micelle is found to be about 85, consistent with previous experimental predictions. While the coarse-grained simulations provide thermodynamic properties of the micelles, the atomic resolution information such as the hydrogen bonds formation and hydration water decay times could only be obtained via atomistic simulations. We conduct atomistic simulations on HEUR micelles of various sizes and find that the PEO groups form hydrogen bonds with water, and the PEO groups immediately adjacent to the hydrophobes form fewest hydrogen bonds compared to other PEO groups, the average number of hydrogen bonds per PEO doesn't seem to be affected by the HEUR micelle size. However, the hydration water life time is found to be affected by the aggregation number of the micelles. Bigger HEUR micelles result in longer residence times of hydration waters. The life time of hydration water is also found to be location dependent; the hydration water molecules near the PEO groups furthest from the hydrophobes have the shortest decay time, while those in proximity of the PEO groups adjacent to the hydrophobes decay most slowly.

5.2 Outlook

There exist many exciting challenges and opportunities for extending the work presented here. Applying the techniques presented here, one could solve real-life engineering problems of waterborne coatings and many similar systems. The future work have also been discussed as listed below:

1. The atomistic model for the latex/water interface could be applied to study the commercial formulations of waterborne coatings including the latex particles,

rheology modifiers, surfactants and other additives. For example, it is of interest to evaluate the effect of SDS coverage on the adsorption of HEUR adsorption on the latex surface. The free energy profile of transferring a hydrophobe of a HEUR molecule adsorbed on the latex surface will provide insight on the bridge/loop ratio of HEUR molecule in waterborne coating, which is essential for the reology of the waterborne coatings.

2. With the knowledge of HEUR bridge/loop ratio as a function of SDS coverage and HEUR concentration, we can calculate the free energy profile of separating two latex particles at various conditions. While the length scale of this system can be beyond the ability of atomistic simulations, corse-grained force field parameters should be developed for the PMMA/PBA copolymers to reproduce the interfacial properties of copolymer/water interface.

3. Then Brownian dynamics simulations can be conducted on the particles alone with the polymers being included only implicitly, through the colloidal-scale PMF. Since the degrees of freedom are now reduced to just the centers of the latex particles, a system containing a large number of particles can be simulated. The phase behavior of this system can thereby be determined. In addition, flow can be imposed on the suspension through standard methods. The shear viscosity as a function of shear rate can be calculated, and compared to experimental results. Thus, the origin of rheological effects, such as yield stress, shear thinning, shear thickening, and hysteretic effects, can be traced to the molecular interactions at the atomistic scale, through the multi-scale simulation approach.

APPENDIX

APPENDIX A

CGenFF parameters for polymers

1. atom types

All the parameters here listed were generated by SwissParam[1]. All carbonyl carbons are assigned the atom type C=O, all the carbonyl oxygens are assigned the atom type O=C, and oxygen atoms connected to C=O are assigned atom type OR. All the other carbons are assigned atom type CR, and all the hydrogens are assigned atom type HCMM.

2. bond parameters

$V_b(r_{ij}) = \frac{1}{2}k^b_{ij}(r_{ij} - b_{ij})^2$

i	j	b_{ij} (nm)	k^b_{ij} $(kJmol^{-1}nm^{-2})$
CR	CR	0.15080	256422.30
CR	C=O	0.14920	252327.80
C=O	O=C	0.12220	779866.60
C=O	OR	0.13550	349343.90
OR	CR	0.14180	303937.50
CR	HCMM	0.10930	287014.90
OR	HOCO	0.09810	445818.60

3. angle parameters

$V_a(\theta_{ijk}) = \frac{1}{2}k^\theta_{ijk}(\theta_{ijk} - \theta^0_{ijk})^2$

i	j	k	$\theta^0_{ijk}(deg)$	$k^\theta_{ijk}(kJmol^{-1}rad^{-2})$
CR	CR	HCMM	110.54900	383.00000
HCMM	CR	HCMM	108.83600	310.74000
CR	CR	CR	109.60800	512.48000
CR	CR	C=O	107.51700	467.91000
CR	C=O	O=C	124.41000	564.87000
C=O	OR	HOCO	111.94800	351.09000
O=C	C=O	OR	124.42500	695.55000
OR	CR	HCMM	108.57700	470.32000
C=O	OR	CR	108.05500	555.84000
HCMM	CR	C=O	108.38500	391.44000
CR	C=O	OR	109.71600	628.1000
OR	CR	CR	108.13300	597.39000

4. proper dihedral parameters

$v_d(\phi_{ijkl}) = k_\phi(1 + cos(n\phi - \phi_s)))$

i	j	k	l	$\phi_s(deg)$	$k_\phi(kJmol^{-1})$	multiplicity
CR	CR	CR	CR	0.0000	0.2134	1
CR	CR	CR	CR	180.0000	1.4267	2
CR	CR	CR	CR	0.0000	0.6945	3
CR	CR	CR	HCMM	0.0000	1.3389	1
CR	CR	CR	HCMM	180.0000	-1.3180	2
CR	CR	CR	HCMM	0.0000	0.5523	3
CR	CR	C=O	O=C	0.0000	1.7238	1
CR	CR	C=O	O=C	180.0000	0.2929	2
CR	CR	C=O	O=C	0.0000	0.6820	3

CR	CR	C=O	OR	0.0000	-0.2469	1
CR	CR	C=O	OR	180.0000	-0.6987	2
CR	CR	C=O	OR	0.0000	0.4226	3
CR	CR	CR	C=O	0.0000	0.1381	1
CR	CR	CR	C=O	180.0000	-0.3264	2
CR	CR	CR	C=O	0.0000	0.2971	3
CR	C=O	OR	HOCO	0.0000	-2.4393	1
CR	C=O	OR	HOCO	180.0000	10.6232	2
CR	C=O	OR	HOCO	0.0000	-1.1422	3
C=O	CR	CR	HCMM	0.0000	-0.5356	1
C=O	CR	CR	HCMM	180.0000	0.1213	2
CR	C=O	OR	CR	0.0000	-2.6024	1
CR	C=O	OR	CR	180.0000	11.4683	2
CR	C=O	OR	CR	0.0000	0.7615	3
O=C	C=O	OR	HOCO	0.0000	3.4769	1
O=C	C=O	OR	HOCO	180.0000	12.8700	2
O=C	C=O	OR	HOCO	0.0000	-0.1213	3
HCMM	CR	CR	HCMM	0.0000	0.5941	1
HCMM	CR	CR	HCMM	180.0000	-2.8995	2
HCMM	CR	CR	HCMM	0.0000	0.6569	3
O=C	C=O	CR	HCMM	0.0000	1.3807	1
O=C	C=O	CR	HCMM	180.0000	-2.9455	2
O=C	C=O	CR	HCMM	0.0000	0.6443	3
OR	C=O	CR	HCMM	180.0000	-1.3054	2
OR	C=O	CR	HCMM	0.0000	0.6904	3
O=C	C=O	OR	CR	0.0000	1.4267	1

O=C	C=O	OR	CR	180.0000	15.0289	2
O=C	C=O	OR	CR	0.0000	-1.9581	3
C=O	OR	CR	HCMM	0.0000	1.1966	1
C=O	OR	CR	HCMM	0.0000	-0.6360	3
OR	CR	CR	HCMM	0.0000	-1.3682	1
OR	CR	CR	HCMM	180.0000	2.2426	2
OR	CR	CR	HCMM	0.0000	0.5858	3
C=O	OR	CR	CR	0.0000	-1.1464	1
C=O	OR	CR	CR	0.0000	0.6694	3
OR	CR	CR	CR	0.0000	-1.4393	1
OR	CR	CR	CR	180.0000	3.6736	2
OR	CR	CR	CR	0.0000	0.9958	3

5. improper dihedral parameters

$V_{id}(\xi_{ijkl}) = \frac{1}{2}k_\xi(\xi_{ijkl} - \xi_0)^2$

i	j	k	l	$\xi_0(deg)$	$k_\xi(kJmol^{-1}rad^{-2})$
C=O	X	X	O=C	0.00	84.9101

6. non-bonded potential parameters

$V_{LJ}(r_{ij}) = 4\epsilon_{ij}((\frac{\sigma_{ij}}{r_{ij}})^{12} - (\frac{\sigma_{ij}}{r_{ij}})^6)$

atom	$\sigma(nm)$	$\epsilon(kJmol^{-1})$
CR	0.387541	0.230120
C=O	0.356359	0.460240
O=C	0.302905	0.502080
OR	0.315378	0.636386
HCMM	0.235197	0.092048
HOCO	0.040001	0.192464

7. partial charges

All carbonyl carbons (C=O) are assigned a charge of 0.659, all carbonyl oxygens (O=C) are assigned a charge of -0.57, all oxygens connected with the carbonyl carbons (OR) are assigned a charge of -0.43, all carbons connected with C=O are assigned a charge of 0.061, and all the carbons connected with OR are assigned a charge of 0.28. All the other atoms are neutral. All the partial charges were generated by SwissParam.

Bibliography

[1] V. Zoete, M. A. Cuendet, A. Grosdidier, and O. Michielin, "Swissparam: a fast force field generation tool for small organic molecules," *Journal of computational chemistry*, vol. 32, no. 11, pp. 2359–2368, 2011.